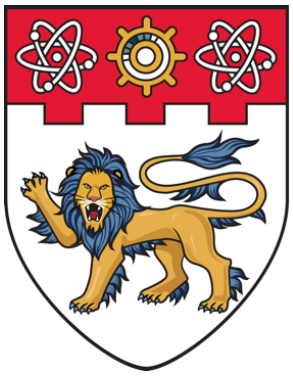

NANYANG TECHNOLOGICAL UNIVERSITY
SINGAPORE

Probing Exciton Properties and Dynamics in Lead Halide Perovskite Semiconductors by Optical Spectroscopy

Do Thi Thu Ha

SCHOOL OF PHYSICAL AND MATHEMATICAL SCIENCES

2019

Probing Exciton Properties and Dynamics in Lead Halide Perovskite Semiconductors by Optical Spectroscopy

Do Thi Thu Ha

SCHOOL OF PHYSICAL AND MATHEMATICAL SCIENCES

A thesis submitted to the Nanyang Technological University in partial fulfilment of the requirement for the degree of Doctor of Philosophy

2019

Statement of Originality

I hereby certify that the work embodied in this thesis is the result of original research done by me except where otherwise stated in this thesis. The thesis work has not been submitted for a degree or professional qualification to any other university or institution. I declare that this thesis is written by myself and is free of plagiarism and of sufficient grammatical clarity to be examined. I confirm that the investigations were conducted in accord with the ethics policies and integrity standards of Nanyang Technological University and that the research data are presented honestly and without prejudice.

29/07/2019

. . . . . .

Date

. . . . . .

Do Thi Thu Ha

Supervisor Declaration Statement

I have reviewed the content and presentation style of this thesis and declare it of sufficient grammatical clarity to be examined. To the best of my knowledge, the thesis is free of plagiarism and the research and writing are those of the candidate's except as acknowledged in the Author Attribution Statement. I confirm that the investigations were conducted in accord with the ethics policies and integrity standards of Nanyang Technological University and that the research data are presented honestly and without prejudice.

29/07/2019

. . . . . .

Date

. . . . . .

Xiong Qihua

Authorship Attribution Statement

This thesis contains material from 1 paper published in the following peer-reviewed journal in which I am listed as an author.

Chapter 4 is published as T. Thu Ha Do, A. Granados del Águila, Chao Cui, Jun Xing, Zhijun Ning, Qihua Xiong. Optical study on intrinsic exciton states in high-quality $CH_3NH_3PbBr_3$ single crystal. *Physical Review B* **96**, 075308 (2017). DOI: 10.1103/PhysRevB.96.075308.

The contributions of the co-authors are as follows:

- Prof. Qihua Xiong and Prof. Zhijun Ning started the jointed project.
- Chao Cui and Dr. Jun Xing prepared the samples.
- I and Dr. Andrés Granados del Águila co-designed the study and performed all the optical measurements at the School of Physical and Mathematical Sciences.
- I and Dr. Andrés Granados del Águila analyzed the data.
- I conducted X-ray Diffraction measurement using The Characterization Facilities at the School of Physical and Mathematical Sciences.

29/07/2019

. . . . . .

Date

. . . . . .

Do Thi Thu Ha

Abstract

Lead halide perovskite semiconductors have emerged as potential building blocks for photovoltaic and optoelectronic applications. The rapid development of the low-cost synthesis methodologies and the continuous improvement of perovskite-based device efficiency have stimulated intensive research to unravel the behaviours of the photo-generated species, such as electrons, holes, coupled electron-hole pairs (excitons) and their interactions. The fundamental understanding of the electronic band structures and the interparticle coupling is still at its early stage. Several controversies among the experimental observations need to be resolved by both experimental and theoretical means.

In this thesis, by utilizing steady-state and time-resolved optical spectroscopy, we investigate the exciton structures, linear and nonlinear optical properties and the effects of quantum-confinement on the optical responses of perovskite materials. Our systematic studies reveal that lead halide perovskites have complicated band structures with multiple states near the bandgap region, which are separated by only tens of milli-electron volts. As a result, multiple optical transitions occur to generate electron-hole pairs with different binding energies and properties. Under strong quantum-confinement regime, the spin-degeneracy of the exciton bands can be lifted due to the enhanced Coulomb interaction between electrons and holes that consequently produces exciton fine-structure. Particularly, in perovskite quantum-wells, we resolve the anisotropic excitons split by the anisotropic electron-hole exchange interaction, which, on the other hand, does not affect the spin-polarization of the indirect excitons. The interplay of different spin-interacting processes gives rise to the coexistence of anisotropic and isotropic excitons in two-dimensional perovskites. Moreover, the exciton dynamics in low-dimensional structures is found to be faster due to the stronger interparticle interactions.

The coupling between electrons and holes or electrons and phonons is also enhanced when further reducing the crystal dimensions into nanocrystal form leading to interesting phenomena. The electron-phonon and phonon-phonon interactions are found to be strong that are responsible for the phonon-assisted exciton transitions in perovskite nanocrystals. As a result, thermal energy can be efficiently extracted to produce light energy. Our results

demonstrate that perovskite nanocrystals are ideal platforms for the energy conversion purposes.

Our findings presented in this thesis provide deep insights into the exciton band structures and exciton fine-structure of perovskite materials. More questions are still to be solved in the future work to reconcile the discrepancy between experimental observations and theory. A unified understanding of the fundamental properties on this emergent class of semiconductors will pave the way towards exciton manipulation for novel device applications.

Acknowledgement

This thesis will close my four-year journey as a Ph.D. student, which has been filled with lessons and growth. I treasure all the bad and good experiences that have created a stronger me today. Along this journey, I owe many people, who have provided their invaluable help for my research and who have accompanied me throughout this challenging time, a great debt of gratitude.

First, I would like to deeply appreciate my supervisor – Professor Xiong Qihua, who constantly inspired my confidence to take the Ph.D. challenge four years ago. Under his supervision, I have learned to work independently, responsibly and critically. Since my second year, he has given me freedom to explore the physics that I was interested in. It was difficult at the beginning, but his guidance brought me to the right track. His perseverance has taught me how to view failures at a positive angle and to keep fighting hard to finally achieve the set goals. In addition, he has provided me countless opportunities to collaborate with scientists with different backgrounds, from whom I have gained a lot of knowledge. All what I have earned in Prof. Xiong's group will be the luxury luggage for my future journeys.

The second very important person, who I would like to express my appreciation to, is Dr. Andrés Granados del Águila, for being a great mentor and the best colleague of mine. He was the one who has spent days and nights in the lab doing experiments with me and patiently taught me every single detail of the optical setups. During all my projects, he raised a thousand of scientific questions for me to address before the projects could be considered as 'finished'. His infinite curiousity, imagination and strong passion have strongly motivated me to explore new things. Besides research matters, Andrés, thank you for being a great friend, for all the joys, jokes, stories and experiences that we shared with each other, for bringing many good friends to my life, and for your timely and generous help whenever I need.

I would like to thank my collaborators, Chao Cui and especially Xing Jun for their high-quality samples that play an important role on all my optical studies. Thanks to Liu Sheng and Bao Di for being good colleagues and friends. Many thanks to Dr. Ha Son Tung for being a close senior, who introduced to me different research perspectives

and gave me advices. Furthermore, I also want to thank all members in Xiong group for their kind help, training and suggestions for my projects.

Next, I want to send a big thank to all of my friends. No matter where they are living now, it is my great honour to have them around. Special thanks to Huong Nguyen for being my best friend since we were just little kids, for always staying by my side, listening, understanding and sympathizing with my sorrows and joys. Thanks all my close and good friends for continuously filling my life with a bundle of unforgettable memories. Even though I cannot list all your names here, our friendship means so much to me. One day, we will meet again and have fun together.

Last but not least, this thesis would not be started nor completed without the unconditional support from my grandparents, my parents, my brother and my sister-in-law. Their infinite love and care have been always encouraging me to fight hard with the most difficult time. I hope that the completion of my Ph.D. will make them happy as much as how their love does to me. Finally, thank you, Nhut, for having been experiencing and growing up with me for the past years. Despite how tough the challenges were, we have eventually overcome them all and become tougher. Today, I would like to express my deepest love and gratitude to my beloved family. For the precious happiness that I have ever received, this thesis is dedicated to them.

Table of Contents

List of Figures

List of Tables

Chapter 1

General Introduction

Light-matter interaction has been intensively studied for decades to understand the crystal structures and the inherent properties of solid-state materials. The most fundamental processes, such as light absorption and light emission, which determine the appearance of an object to human eyes, strongly depend on the chemical compositions as well as the crystal sizes. Several optical spectroscopy techniques have been developed to investigate not only the final outcomes but also the transient states of the materials after the photo-excitation. The understanding of how light and matter interact is fundamentally and practically important for the development of novel photonic devices.

An ideal solid-state crystal is built up from atoms, which are arranged in a periodic lattice to form a macroscopic-sized crystalline crystal [1]. Continuous efforts have resulted in the discovery of a wide variety of crystal lattices for many kinds of semiconductors, whose compositions cover a large portion of the periodic table. Such diversity offers broad choices for materials with desired properties. Furthermore, the rapid development of fabrication techniques using bottom-up and top-down approaches has opened up a fascinating nanoscale world, where quantum-wells, quantum-wires and quantum-dots exhibit completely different optical and electrical properties from the bulk due to quantum-confinement effects. Tailoring the sizes and shapes of these nanostructures enables the exploration for new physical phenomena and their applications in, for example, photovoltaic [2], light-emitting devices [3] and biomedical tagging [4].

This thesis will present a systematic study on an emergent class of materials: lead halide perovskite semiconductors, in which lead and halogen atoms are arranged in a perovskite lattice. The past decade has witnessed intensive research on these materials due to the excellent optical and electrical properties, which inherit from their strong light absorption [5], strong light emission [6] and long carrier diffusion length [7]. Furthermore, their bandgap can be finely tuned with high precision to cover the entire visible regions of the electromagnetic spectrum. To date, high-quality samples can be

synthesized by chemical methods, making perovskite family a promising candidate for low-cost photovoltaics and light-emitting devices. In addition, not only bulk crystals but also low-dimensional perovskite nanostructures such as quantum-wells, nanowires and nanocrystals, have been successfully synthesized with high quality, high throughput and good reproducibility [8] that allow for the fundamental study on the intrinsic optical properties of these materials under different quantum-confinement regime.

Although the fabrication as well as the excellent performance of perovskite-based devices have been tremendously reported, there remains lack of a consistent understanding on the electronic band structure, which is the root of all the light-induced phenomena. Specifically, the interaction between the photo-generated carriers (electrons, holes), between different coupled electron-hole pairs (excitons) and between the particles/quasi-particles and the lattice vibration (phonons), remains controversial. Therefore, the optical responses of perovskite materials are not well understood. Confining the carrier motions in a limited space of low-dimensional nanostructures further complicates the exciton pictures. In strong quantum-confinement regime, the interparticle interactions can be strengthened by several to hundreds times. A primary consequence is the widening of the bandgap found in low-dimensional structures as decreasing the crystal size. Furthermore, the enhanced spin-exchange interaction between electrons and holes can lift the degeneracy of a degenerate band and cause an energy splitting between the exciton sub-bands. The exciton fine-structure in perovskite nanostructures is currently under debate. Contradicting scenarios have been rationalized for the band degeneracy and dark-bright nature of the optical transitions in low-dimensional perovskite systems. High-quality nanostructures with reduced traps and scattering centers, which produce optical spectra with narrow linewidths, are critically required.

In addition to the prominent linear optical properties, lead halide perovskites are also known by their remarkable nonlinear responses. Large multiple-photon absorption cross-section [9] and strong phonon-assisted optical transitions [10] have been reported in perovskite nanostructures that results in surprisingly strong fluorescence upconversion. In the latter case, low-energy photo-excitations are able to induce real electronic transitions by the additional absorption of internal energy in the form of lattice vibration. If the removal of the internal energy is more efficient than the heating effects induced by the laser illumination, semiconductor lattices will be cooled down as demonstrated in Ref. [10] and Ref. [11]. These observations have motivated us to investigate how phonon energies could be exploited in the upconversion photoluminescence process that

may stimulate the new designs of nanomaterials towards the efficient use of the lattice energy for energy conversion applications.

In this thesis, we aim to address three main fundamental questions:

1. How are the electronic band structures and how do the photo-excited carriers interact in lead halide perovskites? How do these properties depend on chemical compositions?

2. How do the quantum- and dielectric-confinement affect the exciton spectra and exciton dynamics in low-dimensional perovskite nanostructures? How do different spin-interacting processes alter the exciton properties?

3. How does the lattice vibrational energy assist the exciton transition under below-bandgap excitation in perovskite nanocrystals?

The organization of this thesis is as the following. **Chapter 2** provides the background on the linear and nonlinear optical processes in semiconductors and how these properties vary with the crystal dimensionality. In particular, interband transitions, formation of excitons, quantum-confinement and its immediate effects on the band structures and optical properties of semiconductors will be discussed. At the end of this chapter, an introduction on lead halide perovskite structures, together with the synthesis and the current status of the fundamental understanding on intrinsic properties of these semiconductors, will be given.

Chapter 3 presents different spectroscopic techniques that have been used throughout the thesis, including steady-state (absorption, reflection, photoluminescence) and time-resolved (photoluminescence, absorption) techniques. The working principle of each technique, instrumentation and experimental setup will be described along with relevant details on the data acquisition and analysis.

Chapter 4 focuses on the exciton properties in three-dimensional perovskite bulk crystals composed of different chemical constituents. Both hybrid organic-inorganic and all-inorganic perovskites are systematically studied that reveal multiple exciton bands in all of the examined compounds. The potential origins of the multibands in the perovskite family will be discussed. The relaxation between the exciton bands and the photoluminescence lifetime will be explained.

The thesis continues with **Chapter 5** presenting the optical responses of perovskite quantum-well systems. In consistent with the bulk form, multiple optical transitions with distinct properties are resolved. An systematic study on the polarization of the

anisotropic and isotropic exciton structures will be presented, followed by the discussion on different spin-interacting processes, which are responsible for the peculiar exciton spectra. The non-trivial exciton dynamics in two-dimensional perovskite systems, such as the buildup and decay of the exciton populations will also be discussed.

Chapter 6 describes the linear and nonlinear optical responses of zero-dimensional perovskite nanocrystals under different excitation conditions. Specifically, the chapter will extensively discuss the important role of the strong electron-phonon and phonon-phonon interactions on the enhanced probability of the phonon-assisted exciton transitions using low-energy photo-excitation.

All the key findings will be summarized in **Chapter 7**. An outlook for the future of perovskite research will also be briefly presented. Few research questions regarding the fundamental understanding of lead halide perovskites materials, are to be answered that will make an essential contribution to the design and fabrication of novel high-performance perovskite-based devices.

References

1. Kittel, C., McEuen, P. & McEuen, P. *Introduction to solid state physics* (Wiley New York, 1976).

2. Kojima, A., Teshima, K., Shirai, Y. & Miyasaka, T. Organometal halide perovskites as visible-light sensitizers for photovoltaic cells. *J. Am. Chem. Soc.* **131,** 6050–6051 (2009).

3. Dai, X., Zhang, Z., Jin, Y., Niu, Y., Cao, H., Liang, X., Chen, L., Wang, J. & Peng, X. Solution-processed, high-performance light-emitting diodes based on quantum dots. *Nature* **515,** 96 (2014).

4. Bruchez, M., Moronne, M., Gin, P., Weiss, S. & Alivisatos, A. P. Semiconductor nanocrystals as fluorescent biological labels. *Science* **281,** 2013–2016 (1998).

5. Yang, Y., Yang, M., Moore, D. T., Yan, Y., Miller, E. M., Zhu, K. & Beard, M. C. Top and bottom surfaces limit carrier lifetime in lead iodide perovskite films. *Nat. Energy* **2,** 16207 (2017).

6. Zhu, H., Fu, Y., Meng, F., Wu, X., Gong, Z., Ding, Q., Gustafsson, M. V., Trinh, M. T., Jin, S. & Zhu, X. Lead halide perovskite nanowire lasers with low lasing thresholds and high quality factors. *Nat. Mater.* **14,** 636–642 (2015).

7. Dong, Q., Fang, Y., Shao, Y., Mulligan, P., Qiu, J., Cao, L. & Huang, J. Electron-hole diffusion lengths >175 μm in solution-grown $CH_3NH_3PbI_3$ single crystals. *Science* **347,** 967–970 (2015).

8. Ha, S. T., Su, R., Xing, J., Zhang, Q. & Xiong, Q. Metal halide perovskite nanomaterials: synthesis and applications. *Chem. Sci.* **8,** 2522–2536 (2017).

9. Chen, W., Bhaumik, S., Veldhuis, S. A., Xing, G., Xu, Q., Grätzel, M., Mhaisalkar, S., Mathews, N. & Sum, T. C. Giant five-photon absorption from multidimensional core-shell halide perovskite colloidal nanocrystals. *Nat. Commun.* **8,** 15198 (2017).

10. Ha, S. T., Shen, C., Zhang, J. & Xiong, Q. Laser cooling of organic–inorganic lead halide perovskites. *Nat. Photonics* **10,** 115 (2016).

11. Zhang, J., Li, D., Chen, R. & Xiong, Q. Laser cooling of a semiconductor by 40 kelvin. *Nature* **493,** 504 (2013).

Chapter 2

Excitons in Semiconductors

Intrinsic properties of a material rely on its electrons, whose microscopic behaviours are determined by the electronic band structure. Semiconductors and insulators are distinguished from metals by the existence of the finite energy gaps or forbidden energy regions between the valence and conduction bands. The typical bandgap of semiconductors lies within >0 to 3 eV [1]. In semiconductor bulk crystals, carriers move freely in three dimensions. Confining the carrier motions in low-dimensional structures, such as quantum-wells, quantum-wires and quantum-dots, entirely alters the energy spectra due to the energy quantization along the confining directions.

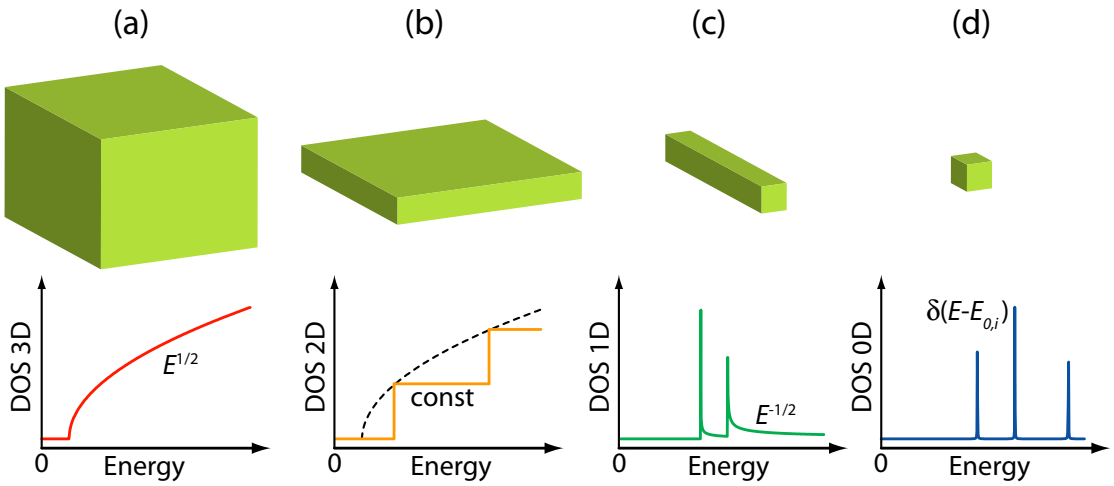

Figure 2.1: Density of states of quantum-confined semiconductor systems. (a) three-dimensional (3D) bulk crystal with DOS $\propto E^{1/2}$, (b) two-dimensional (2D) quantum-well with energy-independent DOS, (c) one-dimensional (1D) quantum-wire with DOS $\propto E^{-1/2}$ and (d) zero-dimensional (0D) quantum-dot with discrete DOS $\propto \delta(E - E_{0,i})$.

Figure 2.1 sketches the density of states (DOS), which somewhat reflects the absorption profile of semiconductors in different quantum-confined structures such as three-dimensional (3D) bulk (panel(a)), two-dimensional (2D) quantum-well (panel(b)), one-dimensional (1D) quantum-wire (panel (c)) and zero-dimensional (0D) quantum-dots (panel (d)). The semiconductor bandgap increases as reducing the dimensionality.

This chapter will describe the effects of quantum-confinement on the behaviours of photo-generated carriers and their interactions. The quantum-wire structure will not be discussed.

2.1 Semiconductors Bulk Crystals

2.1.1 Electronic Band Structure

The motion of a single nonrelativistic particle having a mass m is described by its position ($\boldsymbol{r}$) and momentum ($\boldsymbol{p}$). In quantum mechanics, the behaviours of the particle at any arbitrary time t are all compacted in a wavefunction $\Psi(\boldsymbol{r}, t)$, which is the solution of the time-dependent Schrödinger equation:

$$i\hbar\frac{\partial}{\partial t}\Psi(\boldsymbol{r}, t) = \hat{\mathcal{H}}\Psi(\boldsymbol{r}, t), \tag{2.1}$$

where $\hbar$ is the reduced Planck constant. The Hamiltonian operator $\hat{\mathcal{H}}$ is constructed from the kinetic energy $\boldsymbol{p}^2/2m$ and the potential energy $\hat{\mathcal{V}}$. Since the operators $\boldsymbol{p}^2/2m$ and $\hat{\mathcal{V}}$ only act on the spatial part of the wavefunction, $\Psi(\boldsymbol{r}, t)$ can be separated into spatial $\psi(\boldsymbol{r})$ and temporal $T(t)$ components, which can be solved independently and $\Psi(\boldsymbol{r}, t) = \psi(\boldsymbol{r})T(t)$. The total energy of the particles is deduced from the eigenvalue of $\hat{\mathcal{H}}$.

In the periodic potential of a bulk crystal, the spatial part of the electron wavefunction has the form of:

$$\psi_{\boldsymbol{k}}(\boldsymbol{r}) = u_{\boldsymbol{k}}(\boldsymbol{r})e^{i\boldsymbol{k}.\boldsymbol{r}}, \tag{2.2}$$

where $u_{\boldsymbol{k}}(\boldsymbol{r})$ is a periodic function with the same periodicity as the crystal potential and $e^{i\boldsymbol{k}.\boldsymbol{r}}$ is the crystal plane-wave with wavevector $\boldsymbol{k}$ [2]. The resultant electron energy as a function of $\boldsymbol{k}$, *i.e.,* $E(\boldsymbol{k})$, establishes the electronic band structure, which determines the optical properties of the semiconductor. Due to the periodicity of the crystal lattice, the Bloch wavefunction in Eq. (2.2) described by a wavevector $\boldsymbol{k}$ is equivalent to that described by a wavevector $\boldsymbol{k} + \boldsymbol{G}$, where $\boldsymbol{G}$ is the reciprocal lattice vector. Hence, the band structures of semiconductors are normally discussed within the first Brillouin zone, where the all the Bloch wavefunctions can be characterized by a unique $\boldsymbol{k}$.

Furthermore, the carriers moving in the lattice experience different 'masses' from their free masses in the vacuum [2, 3]. Therefore, the effective mass m^*, which takes into

account the interaction between the carriers and the crystal potential, is normally used. In the simplified forms, the valence and conduction band dispersion near the extrema can be approximated by parabolic functions:

$$E_v(\boldsymbol{k}) = -\frac{\hbar^2 \boldsymbol{k}^2}{2m_h^*}, \tag{2.3}$$

$$E_c(\boldsymbol{k}) = E_g + \frac{\hbar^2 \boldsymbol{k}^2}{2m_e^*}, \tag{2.4}$$

where m_h^* and m_e^* denote the effective masses of the hole and electron in valence and conduction bands, respectively. From Eqs. (2.3) and (2.4), $m_{e/h}^*$ can be deduced from the curvature of the corresponding band dispersion at its extremum.

2.1.2 Interband Transitions

Semiconductors in ground state have the valence bands completely filled by electrons and the conduction bands completely unoccupied. Illuminating a semiconductor with light of appropriate energy, which is larger than the bandgap energy ($\hbar\omega \geq E_g$), can excite the valence electrons to conduction band, leaving holes in the valence band. The photo-excited electrons and holes relax to the bandedges, where they can radiatively recombine producing photons or non-radiatively recombine releasing energy in the form of heat. The transitions between the conduction and valence bands are called interband transitions. Due to the continuous bands, the light absorption can occur over a continuous range of photon frequency as long as the condition $\hbar\omega \geq E_g$ is satisfied. This is in contrary to the absorption spectra of atoms or molecular systems, which only absorb particular photon energies matching the energy difference between discrete states.

The absorption rate of a photon with wavevector $\boldsymbol{q}$ and energy $\hbar\omega$ can be evaluated by the Fermi golden rule [4]:

$$W_{\mathrm{v-c}}^{\mathrm{3D}}(\hbar\omega) = \frac{2\pi}{\hbar}\left|M_{\mathrm{v-c}}^{\mathrm{3D}}\right|^2 g(\hbar\omega), \tag{2.5}$$

where $M_{\mathrm{v-c}}^{\mathrm{3D}}$ is the matrix element describing the transition of the electrons from initial state $|v\rangle$ to final state $|c\rangle$ induced by light, and $g(\hbar\omega)$ is the joint density of states describing the distribution of the states lying in the continuum, which are associated to the interband transitions. Each factor will be independently considered.

Using Dirac notation, where $|v\rangle$ and $|c\rangle$ are represented by the carrier wavefunctions

ψ_v and ψ_c, respectively, the matrix element is expressed as:

$$M_{\mathrm{v-c}}^{\mathrm{3D}} = \langle v|\hat{\mathcal{V}}|c\rangle\,, \tag{2.6}$$

where $\hat{\mathcal{V}} = -e\boldsymbol{r}.\boldsymbol{\xi}$ (2.7) is the perturbation operator created by the electric field $\boldsymbol{\xi} = \boldsymbol{\xi_0}e^{i\boldsymbol{q}.\boldsymbol{r}}$. On the other hand, the electron in valence and conduction bands can be described by the Bloch wavefunctions in the same manner as shown in Eq. (2.2):

$$|v\rangle \equiv \psi_v(\boldsymbol{r}) = \frac{1}{\sqrt{\Omega}}e^{i\boldsymbol{k_v}.\boldsymbol{r}}u_v(\boldsymbol{r}), \tag{2.8}$$

$$|c\rangle \equiv \psi_c(\boldsymbol{r}) = \frac{1}{\sqrt{\Omega}}e^{i\boldsymbol{k_c}.\boldsymbol{r}}u_c(\boldsymbol{r}), \tag{2.9}$$

where $1/\sqrt{\Omega}$ is the normalization factor. Substituting Eq. (2.7)-(2.9) into Eq. (2.6) and using the momentum conservation $\hbar\boldsymbol{k_c} = \hbar\boldsymbol{k_v} + \hbar\boldsymbol{q}$, we obtain the form of the transition matrix element as:

$$\begin{aligned} M_{\mathrm{v-c}}^{\mathrm{3D}} &= \frac{1}{\Omega}\int_{\mathrm{unitcell}} u_c^*(\boldsymbol{r})e^{-i\boldsymbol{k_c}.\boldsymbol{r}}[\boldsymbol{r}.\boldsymbol{\xi_0}e^{i\boldsymbol{q}.\boldsymbol{r}}u_v(\boldsymbol{r})]e^{i\boldsymbol{k_v}.\boldsymbol{r}}d^3\boldsymbol{r} \\ &\propto \frac{1}{\Omega}\int_{\mathrm{unitcell}} u_c^*(\boldsymbol{r})\boldsymbol{r}u_c^*(\boldsymbol{r})d^3\boldsymbol{r} \equiv \frac{1}{\Omega}\langle c|\boldsymbol{r}|v\rangle\,. \end{aligned} \tag{2.10}$$

The joint density of state $g(\hbar\omega)$ is defined as:

$$g(\hbar\omega) = \frac{2\Omega}{(2\pi)^3}\int \delta[\hbar\omega + E_v(\boldsymbol{k_v}) - E_c(\boldsymbol{k_c})]d^3\boldsymbol{k}, \tag{2.11}$$

where $2\Omega/(2\pi)^3$ describes the number of states in a three-dimensional volume Ω. It changes to $2S/(2\pi)^2$ for two-dimensional area S, $2L/\pi$ for one-dimensional length L, and simply 2 for zero-dimensional case.

For direct-bandgap semiconductors, the valence band maximum (VBM) and the conduction band minimum (CBM) occur at the same $\boldsymbol{k}$-point in the Brillouin zone, denoted as $\boldsymbol{k_0}$ for generality. The band dispersions described in Eq. (2.12) and Eq. (2.13) are modified as:

$$E_v(\boldsymbol{k}) = E_{v,\max} - \frac{\hbar^2}{2m_h^*}(\boldsymbol{k}-\boldsymbol{k_0})^2, \tag{2.12}$$

$$E_c(\boldsymbol{k}) = E_{c,\min} + \frac{\hbar^2}{2m_e^*}(\boldsymbol{k}-\boldsymbol{k_0})^2, \tag{2.13}$$

where $E_{v,\max}$ and $E_{c,\min}$ are the energies at the VBM and CBM, respectively. The fun-

damental bandgap is defined as $E_g = E_{c,\min} - E_{v,\max}$. Substituting the band dispersion into Eq. (2.11), we have:

$$\begin{aligned} g(\hbar\omega) &= \frac{2\Omega}{(2\pi)^3}\int \delta\Big[\hbar\omega - E_g - \frac{\hbar^2}{2\mu}(\boldsymbol{k}-\boldsymbol{k_0})^2\Big]d^3\boldsymbol{k} \\ &= \frac{\Omega}{4\pi^2}\Big(\frac{2\mu}{\hbar^2}\Big)^{3/2}(\hbar\omega - E_g)^{1/2}H(\hbar\omega - E_g), \end{aligned} \tag{2.14}$$

where $\mu = (1/m_e^* + 1/m_h^*)^{-1}$ is the reduced mass of the electron-hole pair and $H(\hbar\omega - E_g)$ is the Heaviside step function. Plugging Eq. ((2.10)) and Eq. (2.14) into Eq. (2.5), we obtain the absorption rate from the valence ($|v\rangle$) or the conduction band ($|c\rangle$) as

$$W_{\mathrm{v-c}}^{\mathrm{3D}}(\omega) = \frac{1}{4\pi^2}\langle c|\boldsymbol{r}|v\rangle\left(\frac{2\mu}{\hbar^2}\right)^{3/2}(\hbar\omega - E_g)^{1/2}H(\hbar\omega - E_g) \tag{2.15}$$

The evaluation of the transition rate requires the understanding of the Bloch functions of the relevant valence ($u_v(\boldsymbol{r})$) and conduction bands ($u_c(\boldsymbol{r})$), which can be calculated from the corresponding atomic orbitals. Since different materials have different band structures, Eq. (2.15) needs to be individually considered.

Once $W_{\mathrm{v-c}}^{\mathrm{3D}}(\omega)$ is known, the absorption coefficient can be calculated as:

$$\alpha(\omega) = \frac{ne^2}{\varepsilon_0\omega c m_0^2}W_{\mathrm{v-c}}^{\mathrm{3D}}(\omega), \tag{2.16}$$

where n is the refractive index of the medium, ε_0 is the permittivity of the vacuum, c is the speed of light and m_0 is the free electron mass. However, the derivation is still much simpler than the experimental results. Coulomb interaction between electrons and holes need to be included to resolve the discrepancy.

On the other hand, in indirect-bandgap semiconductors, the conduction and valence band extrema do not occur at the same $\boldsymbol{k}$-point. Hence, the optical transition at the band-edges cannot take place with a photon only due to the momentum mismatch. Phonons, which are quanta of the lattice vibration energy, are needed to assist the interband transition to satisfy the energy and momentum conservation rules:

$$E_c = E_v + \hbar\omega \pm \hbar\omega_{\mathrm{ph}}, \tag{2.17}$$

$$\hbar\boldsymbol{k_c} = \hbar\boldsymbol{k_v} \pm \hbar\boldsymbol{k_{ph}}, \tag{2.18}$$

where $\hbar\omega_{\mathrm{ph}}$ and $\hbar\boldsymbol{k_{ph}}$ are energy and momentum of the involved phonons, respectively. The plus and minus signs indicate the absorption and emission of a phonon, respectively.

These second-order processes lower the interband transition probability, therefore, alter the absorption coefficients in indirect-bandgap semiconductors *i.e.*, $\alpha^{\text{indir}}(\omega) \propto (\hbar\omega - E_g \mp \hbar\omega_{\text{ph}})^2$ [4].

2.1.3 Excitons: Elementary Excitations

The photo-generated electrons and holes with opposite charges couple with each other through Coulomb electrostatic interaction. The attractive force keeps the carriers orbiting around each other in a stable trajectory. Each coupled electron-hole pair forms a neutral bound state called 'exciton', which can be regarded to as a quasiparticle. Excitons can be classified into two types: Wannier-Mott free excitons, which are normally found in semiconductors, and Frenkel tightly bound excitons, which exist in many insulators or molecular crystals.

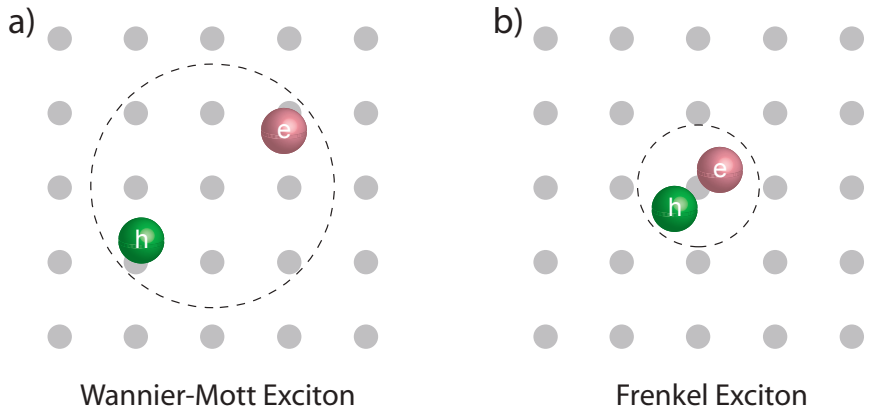

Figure 2.2: Classification of excitons. (a) Wannier-Mott free exciton, whose wavefunction expands over many atoms in the crystal lattice, and (b) Frenkel tightly bound exciton, which is bound to a particular atom or molecule.

A Wannier-Mott exciton is composed of a weakly bound electron-hole pair. The exciton has large radius and its wavefunction covers many lattice points (see Fig. 2.2(a)). Due to the delocalization, the exciton center-of-mass is free to move throughout the crystals. In contrast, Frenkel excitons are localized states that tightly bound to a specific atom site (see Fig. 2.2(b)). Their radii are comparable to one unit cell size. In this thesis, we will only study the Wannier-Mott free excitons in semiconductors, while the Frenkel excitons will not be discussed further.

In general, the dielectric function of a semiconductor is frequency-dependent that is especially modified at the exciton resonance energies. Far from the resonance, the material can be considered as a uniform dielectric environment with an effective dielectric

constant ε_r^*. In many cases, the free exciton can be well described by the hydrogen model [3], in which, the exciton binding energy and Bohr radius can be expressed as

$$E_b(n) = -\frac{\mu}{m_0}\frac{1}{\varepsilon_r^{*2}}\frac{R_H}{n^2} = -\frac{E_{b,X}}{n^2}, \tag{2.19}$$

$$a_B(n) = \frac{m_0}{\mu}\varepsilon_r^* n^2 a_H = n^2 a_X, \tag{2.20}$$

where $\mu = (1/m_e^* + 1/m_h^*)^{-1}$ is the exciton reduced mass, R_H = 13.6 eV and $a_H = 5.29\times10^{-11}$ m is the Rydberg energy and Bohr radius of the hydrogen atom, respectively, $E_{b,X}$ and a_X are the exciton Rydberg energy (binding energy) and exciton Bohr radius, respectively. Since the Coulomb attractive force lowers the total energy of the electron-hole pair by an amount of E_b/n^2, the total energy of an exciton X is given as

$$E_X^{\mathrm{3D}}(n) = E_g - \frac{E_{b,X}}{n^2} + \frac{\hbar^2 \boldsymbol{k}_{\boldsymbol{X}}^2}{2(m_e^* + m_h^*)}, \tag{2.21}$$

where $\boldsymbol{k}_{\boldsymbol{X}}$ is the translational wavevector of the exciton. Equations (2.19) and (2.20) reveal that the lowest-energy exciton (n = 1) is the most tightly bound pair with the smallest radius, while the excited states ($n > 1$) have lower binding energies and larger radii. Exciton binding energy and radius are the most fundamental and crucial parameters for understanding and manipulating the optical and electrical properties of semiconductors.

The correlation between the electron and hole can be destroyed by scattering events with phonons, whose population scales up with temperature. The maximum thermal energy at temperature T is $\sim k_B T$, where k_B is Boltzmann constant. An exciton only exists if $E_b > k_B T$. Otherwise, it is dissociated into free carriers and the exciton picture is no longer valid. The exciton binding energy and Bohr radius vary with different materials. Typically, E_b increases and a_B decreases with increasing E_g as observed in many group II-V and III-V semiconductors (see Table 4.1 in Ref. [4]). In the wide-gap materials, such as insulators with $E_g > 5$ eV, the exciton radius is comparable to the unit-cell size, and the binding energy is in the range of hundreds meV that makes the excitons very stable at high temperature. In this limit, hydrogenic series of Wannier-Mott excitons cannot be applied. In the other limit, the exciton binding energy falls below 1 meV in the narrow-gap materials with $E_g < 0.5$ eV. Hence, excitonic effects are not practically resolved on these materials at temperature above 11 K. The best materials should have the bandgap of 1-3 eV, and exciton binding energy of 2-25 meV that allows for the study of excitonic effects from cryogenic temperature ($k_B T \sim 0.3$ meV) till up to

room temperature ($k_BT \sim 25$ meV).

Although the concepts of free carriers and excitons are rather simple, there are still confusions of the single-particle and quasi-particle pictures, while plotting the band diagram. Figure 2.3 distinguishes two energy schemes for free-carrier (panel (a)) and exciton (panel (b)) representations. The valence and conduction bands in the free-carrier picture corresponds to a single exciton band in the exciton representation. The exciton energy is lowered by E_b and the exciton wavevector is recalculated accordingly as $\boldsymbol{k_X} = \boldsymbol{k_e} - \boldsymbol{k_h}$.

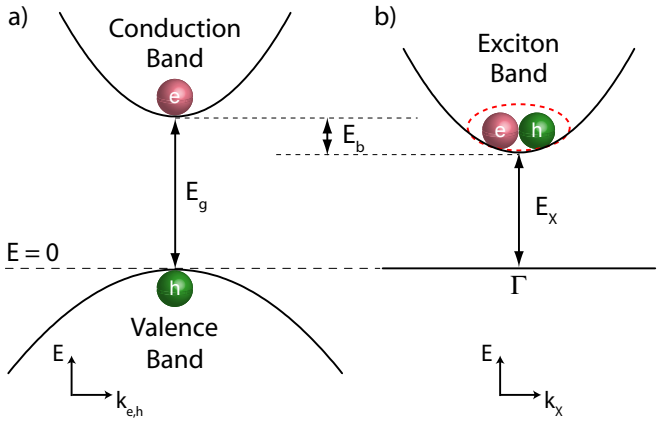

Figure 2.3: Simplified band structure plotted in (a) free-carrier and (b) exciton representations. The exciton energy $E_X = E_g - E_b$ and wavevector $\boldsymbol{k_X} = \boldsymbol{k_e} - \boldsymbol{k_h}$ are recalculated from the free-carrier picture.

2.2 Semiconductor Quantum-Wells

2.2.1 One-Dimensional Quantum-Confinement Effects

The application of quantum confinement on three-dimensional crystals modifies the electronic band structures and consequently, alters the optical responses of the materials. The size-effect is negligible if the crystal is large, but becomes significant when the crystal dimensions are comparable to the exciton Bohr radius a_X. The quantum-confinement effects play important role on this regime and the optical properties depend strongly on the crystal size.

We start with the one-dimensional confinement case, where the thickness of the bulk crystal is truncated to few unit cells (see Fig. 2.1(b)). In practice, the whole system resembles heterostructure crystals, consisting of various layers of different materials: the top vacuum layer, the semiconductor quantum-well layer and the bottom substrate.

The different electronic properties of different layers result in the realignment of the bands in such a way that the whole system bears the same Fermi level. Consequently, the band alignment leads to potential differences at the interfaces of the heterostructures that restrict the motion of carriers across the interfaces. The quantum-well structures can be fabricated by the specialized epitaxial growth techniques such as molecular beam epitaxy (MBE) [5] and metal-organic chemical vapour deposition (MOCVD) [6] or naturally exist in layered materials [7, 8]. In all cases, the thickness of the well and the barrier layers can be controlled down to atomic precision that favors for the systematic studies of the quantum-confinement effects on the carrier and exciton behaviours.

In semiconductor quantum-wells, the carriers are free to move in a two-dimensional xy-plane and restricted to move in the confining z-direction. The wavefunctions and the energies of the confined electrons and holes can be derived from Schrödinger equation using effective mass approximation. The spatial parts of the wavefunctions can be found by separation variables methods, which allow to factorize as $\Psi(x, y, z) = \psi(x, y)\phi(z)$. The electronic states in the system are described by a wavevector $\boldsymbol{k_{xy}}$ for the free motion and by a quantum number n for the quantization energy due to the confinement. The total energy is then calculated by summing up the energy in all directions: $E_{\mathrm{tot}}(\boldsymbol{k_{xy}}, n) = E_{xy}(\boldsymbol{k_{xy}}) + E_z(n)$.

In the simplest case of infinite confining potential, where the carriers are confined in the well thickness L_w and cannot tunnel through the barrier, the Schrödinger equation in the well medium is:

$$-\frac{\hbar^2}{2m^*}\frac{d^2\phi(z)}{dz^2} = E_z\phi(z). \tag{2.22}$$

In order to satisfy the boundary condition as $\phi(z = 0)$ = $\phi(z = L_w)$= 0, the solutions have the form of standing waves with nodes at the well-barrier interfaces as:

$$\phi_n(z) = \sqrt{\frac{2}{L_w}}\sin\Big(k_n z + \frac{n\pi}{2}\Big), \tag{2.23}$$

where the integer n is the quantum number and $k_n = n\pi/d$ is the quantized wavevector. The energy of the n^{th} level along z-direction is:

$$E_n(z) = \frac{\hbar^2 k_n^2}{2m^*} = \frac{\hbar^2}{2m^*}\left(\frac{n\pi}{d}\right)^2. \tag{2.24}$$

On the other hand, the free motion of carriers in the unconfined xy-plane is still well described with Bloch wavefunctions (see Eq. (2.2)). Therefore, the general Bloch

wavefunction for holes and electrons in quantum-wells can be expressed as:

$$|v\rangle \equiv \psi_v = \frac{1}{\sqrt{S}} u_v(x,y)\phi_{h,n}(z)e^{i\boldsymbol{k_{xy}}\cdot\boldsymbol{r_{xy}}}, \tag{2.25}$$

$$|c\rangle \equiv \psi_c = \frac{1}{\sqrt{S}} u_c(x,y)\phi_{e,n'}(z)e^{i\boldsymbol{k'_{xy}}\cdot\boldsymbol{r_{xy}}}, \tag{2.26}$$

where $1/\sqrt{S}$ is the normalization area factor, $\phi_{h,n}$ and $\phi_{e,n'}$ denote the quantized n-hole state and n'-electron state, respectively. For a direct optical transition, $\boldsymbol{k_{xy}} \approx \boldsymbol{k'_{xy}}$ since the momentum of the photon is negligible.

In two-dimensional system, the joint density of state is energy-independent [4]:

$$g(\hbar\omega) = \frac{S\mu}{\pi\hbar^2} H(\hbar\omega - E_g). \tag{2.27}$$

In analogous to the 3D case (see Eq. (2.16)), the Fermi golden rule suggests that the absorption rates in quantum-well is proportional to the density of states $g(\hbar\omega)$ and the transition matrix element ($M^{\mathrm{2D}}_{\mathrm{v-c}} \propto S^{-1}\langle c|\boldsymbol{r}|v\rangle$) as following:

$$\begin{aligned} W^{\mathrm{2D}}_{\mathrm{v-c}}(\omega) &= \frac{2\pi}{\hbar}\left|M^{\mathrm{2D}}_{\mathrm{v-c}}\right|^2 g(\hbar\omega) \\ &= \frac{2\mu}{\hbar^3}|\langle c|\boldsymbol{r}|v\rangle|^2 H(\hbar\omega - E_g). \end{aligned} \tag{2.28}$$

Besides the quantization of the carrier energies in one direction, the quantum confinement also causes an enhancement on the exciton binding energy, since the electron and hole are forced closer and the Coulomb interaction between them consequently becomes stronger. Furthermore, the overlap between the electron and hole wavefunctions increases significantly, leading to the larger transition probability or oscillator strength in 2D as compared to 3D systems. The total energy of excitons in two-dimensional systems, at the limit of widthless quantum-well and infinite barrier potential, is modified as [9]:

$$E^{\mathrm{2D}}_X(n) = E_g + E_{\mathrm{conf}} - \frac{E_{b,X}}{(n-1/2)^2} + \frac{\hbar^2\boldsymbol{k}^2_{\boldsymbol{X}}}{2(m^*_e + m^*_h)}, \tag{2.29}$$

where E_g is the bandgap energy of the bulk, E_{conf} is the confinement energy. Comparing Eq. (2.29) with Eq. (2.21), within the limit of hydrogen model, the binding energy of the lowest-energy exciton (n = 1) increases by four times ($4E_{b,X}$) in 2D systems from the corresponding value in the 3D structure ($E_{b,X}$). If the barrier potential is finite, the binding energy slightly drops to $\sim$2-3$E_{b,X}$ depending on the specific material

parameters. In practice, the quantum-wells have finite widths of L_w, which modifies the exciton binding energy as [9]:

$$E_b^{\mathrm{2D}}(1s) = \frac{E_{b,X}^{\mathrm{3D}}}{(1+\frac{d_{\mathrm{eff}}^*-3}{2})^2}, \tag{2.30}$$

where $d_{\mathrm{eff}} = 3 - \exp(-L_w/2a_B)$ is the effective 'dimensionality'.

The hydrogen model works well to describe the excitonic behaviours in conventional III-V quantum-well systems such as GaAs and GaN [9]. However, it fails to explain the behaviours of excitons in the naturally existing 2D systems such as lead halide perovskite quantum-wells and transition metal dichalcogenide semiconductors, where the binding energies are boosted by orders of magnitude from that in the 3D counterparts [7, 10–14]. In such unconventional 2D systems, the exciton effects need to be explicated by taking into account both quantum- and dielectric-confinement effects. The largely enhanced binding energy make these atomically thin semiconductors extraordinary with nontrivial exciton behaviours.

2.2.2 Optical Selection Rules

The selection rules of the optical transitions in quantum-wells are defined by the transition matrix $M_{\mathrm{v-c}}^{\mathrm{2D}} \propto \langle c|\boldsymbol{r}|v\rangle$, where $\boldsymbol{r}$ is the polarization of the light field. In 3D bulk isotropic crystals, $\langle c|x|v\rangle$, $\langle c|y|v\rangle$ and $\langle c|z|v\rangle$ are equivalent. The selection rule on 3D case depends on the Bloch function, which is determined by the symmetry of bands involved. On the other hand, in 2D systems, the symmetry along z-direction is broken. The components x and y are equivalent, but totally different from z, *i.e.,* $\langle c|x|v\rangle = \langle c|y|v\rangle \neq \langle c|z|v\rangle$. Under normal incident excitation, the excitation polarization is in the xy-plane. Without the loss of generality, we will discuss the case where the electric field is polarized along x direction.

The transition matrix element is rewritten as:

$$\begin{aligned} M_{\mathrm{v-c}}^{\mathrm{2D}} &= M_u M_\phi \\ &= \left(\int_{-\infty}^{\infty}\int_{-\infty}^{\infty} u_c^*(x,y)xu_v(x,y)dydx\right)\left(\int_{-\infty}^{\infty}\phi_{e,n'}^*(z)\phi_{h,n}(z)dz\right), \end{aligned} \tag{2.31}$$

The first integral depends on the transition symmetry, which in many cases is electric-dipole allowed, *i.e.,* $M_u > 0$. Whereas, the second integral ($M_\phi \equiv M_{n,n'}$) describes the quantum-effects on the optical transition matrix. In the simplest case of infinite barrier

potential, we have:

$$M_\phi = \frac{2}{L_w}\int_{-L_w/2}^{+L_w/2} \sin\left(k_n z + \frac{n\pi}{2}\right)\sin\left(k'_n z + \frac{n'\pi}{2}\right)dz. \tag{2.32}$$

The selection rule can be determined by $\Delta n = n' - n$. Equation (2.32) equals to 0 if $n \neq n'$ and equals to 1 if and only if $n = n'$. Therefore, the optical selection rule for an ideal quantum-well is:

$$\Delta n = 0, \tag{2.33}$$

meaning that an optical transition is only allowed when the electron and the hole share the same quantum numbers.

In practice, the potential barrier is usually near-infinite or finite. Therefore, the wavefunctions and energies of the states will be different from Eq. (2.32). The derivation is widely discussed elsewhere [4]. Although there is no analytical solutions for the Schrödinger equations in such cases, the potential is still symmetric about z = 0 similarly to the infinite potential case. Therefore, the eigenstate also has a well-defined parity. However, the electron and hole states of different quantum numbers are not always orthogonal due to the different tunneling constants through the barriers. Therefore, the transitions between $n \neq n'$ can be still allowed but with low probability. Only when Δn is odd, the transitions are forbidden due to the opposite parities [4].

2.2.3 Electron-Hole Exchange Interactions

The quantum-confinement in two-dimensional systems confines the carriers along one direction that strengthens the interaction between electrons and holes. Their wavefunctions are largely overlapped, leading to the great enhancement of oscillator strength and exciton binding energy. In addition, the electron-hole exchange interaction is also enhanced that strongly couples the spins of the spatially confined electron and hole. Taking into account the positions and spins of particles, we have the full forms of their time-independent wavefunctions as $\Psi(\boldsymbol{r}, \boldsymbol{\sigma}) = \psi(\boldsymbol{r}).S(\boldsymbol{\sigma})$, including the spatial $\psi(\boldsymbol{r})$ and spin $S(\boldsymbol{\sigma})$ components. In almost all semiconductor systems, there always exist degenerate states, where multiple substates have the same energy but different spin configurations. The electron-hole exchange interaction will lift the spin-degeneracy of such exciton manifold states, resulting in exciton fine-structure.

The e-h exchange interaction can be calculated by Wannier-function formalism [15]

or k-space method [16]. Both methods give the same results. In the Wannier-function formalism approach, the Bloch functions are expanded into Wannier functions. The exchange matrix element is then obtained by summing up over the lattice sites τ. The term with τ = 0 is called short-range part, whereas the long-range term is associated with $\tau \neq 0$. On the other hand, the k-space method is developed by expanding the products of the periodic Bloch function in plane waves using reciprocal lattice vectors $\boldsymbol{G}$ and Fourier transform. The e-h exchange matrix element is [17]:

$$J(\boldsymbol{k},\boldsymbol{k'}) = \frac{1}{\Omega}\sum_{G} D_{cvk_ck_v}(\boldsymbol{G}) D_{vck'_vk'_c}(-\boldsymbol{G}) \frac{4\pi e^2}{|\boldsymbol{G}+\boldsymbol{k_X}|^2} \equiv \frac{1}{N}(J^{\mathrm{anal}} + J^{\mathrm{non-anal}}), \tag{2.34}$$

where Ω is the volume of a unit cell and

$$D_{cvk_ck_v}(\boldsymbol{G}) = \int u^*_{\boldsymbol{ck_c}}(\boldsymbol{r}) u_{v\boldsymbol{k_v}}(\boldsymbol{r}) e^{-i\boldsymbol{G}.\boldsymbol{r}} d\boldsymbol{r} \tag{2.35}$$

The contribution of all the $\boldsymbol{G} \neq 0$ terms gives rise to the analytical part J^{anal}, which has a well-defined limit as $\boldsymbol{k_X} \to 0$. Whereas, the term with G = 0, having different limits as $\boldsymbol{k_X} \to 0$ for different directions of $\boldsymbol{k_X}$, is non-analytical part $J^{\mathrm{non-anal}}$. Expanding the envelop function around the band extrema $\boldsymbol{k}$ = 0 in the $\boldsymbol{k.p}$ theory, results in:

$$J^{\mathrm{non-anal}}(\boldsymbol{k_X}) = \frac{4\pi e^2}{\Omega \boldsymbol{k_X^2}} \langle u_c|\boldsymbol{k_X}.\boldsymbol{r}|u_v\rangle \ \langle u_v|\boldsymbol{k_X}.\boldsymbol{r}|u_c\rangle \tag{2.36}$$

For $\boldsymbol{k_X} \parallel \boldsymbol{r}$, $J^{\mathrm{non-anal}}$ tends to $4\pi e^2 |\langle u_c|\boldsymbol{r}|u_v\rangle|^2/\Omega$ (longitudinal mode), while $J^{\mathrm{non-anal}}$ becomes 0 or vanishingly small value when $\boldsymbol{k_X} \perp \boldsymbol{r}$ (transverse mode). The energy splitting between the longitudinal and transverse excitons is achieved as:

$$\Delta E_{LT} = g\frac{4\pi |\langle u_c|e\boldsymbol{r}|u_v\rangle|^2}{\varepsilon_\infty} |\psi(0)|^2 \propto \frac{f}{\Omega}, \tag{2.37}$$

where g is the spin-orbit factor which depends on the symmetry of the band, ε_∞ is the dielectric constant at high frequency and $\psi(0)$ is the envelope function describing the relative electron-hole motion in the x-y plane. For 2D excitons, $|\psi(0)|^2 = 2/\pi a_X^2$ [15]. f/Ω is the oscillator strength per unit volume. In the single-well system, f/Ω is negligible leading to the absence of L-T splitting. This problem can be solved by considering multiple-well systems, where f/Ω is finite resulting in a nonvanishing ΔE_{LT}.

2.2.4 Exciton Fine-Structure

Figure 2.4 illustrates the effects of Coulomb e-h exchange interaction on a degenerate exciton band $|X\rangle$. As discussed in Eq. (2.34), the e-h exchange interaction can be divided into analytical (short-range) and non-analytical (long-range) parts. While the analytical component separates the optically-allowed (bright) and optically-forbidden (dark) exciton states, the non-analytical part splits the degenerate bright exciton states into longitudinal $|L\rangle$ and transverse $|T\rangle$ modes, whose polarizations are mutually orthogonal in the quantum-well plane. In the case of light-hole excitons in conventional III-V quantum-wells, there also exists an out-of-plane (Z) mode, which is perpendicular to the in-plane excitons L and T. In backscattering μ-PL experiments, the emission from Z-mode cannot be detected.

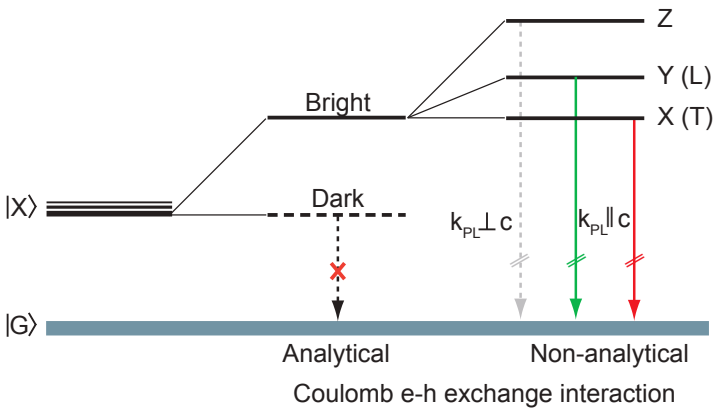

Figure 2.4: Fine-structure splitting of a degenerate exciton state in quantum-wells due to electron-hole exchange interactions. The analytical part causes a splitting between bright and dark states, while the non-analytical component further separates the bright state into longitudinal (L) and transverse (T) modes. In the case of the light-hole exciton, there may exist additional out-of-plane mode (Z). For simplification, the dispersions of the exciton bands are neglected in this scheme.

The increase of e-h wavefunction overlap results in the enhanced oscillator strength and e-h exchange interaction. As a result, the fine-structure splitting becomes more prominent in quantum-confined systems. In typical wurtzite semiconductor quantum-wells, the short-range exchange energy is 0.69 meV in GaN [18], 0.02 meV in GaAs [19] and up to 4.7 meV in ZnO [20]. On the other hand, the long-range exchange interaction can cause an L-T splitting of 0.3 meV in GaAs quantum-wells [15]. These energy splittings are usually smeared out by the inhomogeneous broadening of the sample, which is typically larger than 1 meV. Therefore, spectrally resolving the exciton fine-structure in those quantum-well systems by spectroscopic techniques is challenging.

2.3 Semiconductor Nanocrystals

2.3.1 Three-Dimensional Quantum-Confinement Effects

In three-dimensional bulk crystals and two-dimensional systems, the electrons and holes can be described by Bloch wavefunctions, which can propagate freely in three dimensions and two dimensions, respectively. How about the particles in nanocrystals with all three dimensions confined? The energy levels are quantized and the absorption spectra compose of discrete lines as illustrated in Fig. 2.1(d). Nanocrystals can be fabricated with a variety of compositions and morphologies from spherical quantum-dots, cylindrical quantum-rods to more complicated shapes. Therefore, the optical properties can be tailor made with the carefully designed nanostructures.

The quantum-confinement effects on the electronic structure of the NCs are revealed in the carrier wavefunctions, which are the solutions of the Schrödinger equation (2.1), where $\hat{\mathcal{V}}$ is the confinement potential defined by the size and shape of the nanoscrystal. In the simplest case of rectangular NCs with dimensions of L_x, L_y, L_z and infinite confinement potential, Eq. (2.1) becomes a particle-in-a-box problem, in which the wavevectors of the confined electrons and holes are quantized, *i.e.*, $k = n\pi/L$ with positive integers n.

As a result, the eigenvalues or energies are given by:

$$E_v(n_{h,x}, n_{h,y}, n_{h,z}) = E_{v,\max} - \frac{\pi^2\hbar^2}{2m_h^*}\left(\frac{n_{h,x}^2}{L_x^2} + \frac{n_{h,y}^2}{L_y^2} + \frac{n_{h,z}^2}{L_z^2}\right), \tag{2.38}$$

$$E_c(n_{e,x}, n_{e,y}, n_{e,z}) = E_{c,\min} + \frac{\pi^2\hbar^2}{2m_e^*}\left(\frac{n_{e,x}^2}{L_x^2} + \frac{n_{e,y}^2}{L_y^2} + \frac{n_{e,z}^2}{L_z^2}\right), \tag{2.39}$$

where n_x, n_y, n_z are integer quantum numbers for the quantized states in the direction x, y, z, respectively. Equations (2.38)-(2.39) reveals that the energies of the carriers are discrete and the energy spacing between the levels increases with decreasing NC size. The Bloch wavefunctions of holes and electrons in nanocrystals are written as:

$$|v\rangle \equiv \psi_v(\boldsymbol{r_h}) = u_v(\boldsymbol{r_h})\phi_v(\boldsymbol{r_h}, n_x, n_y, n_z), \tag{2.40}$$

$$|c\rangle \equiv \psi_c(\boldsymbol{r_e}) = u_c(\boldsymbol{r_e})\phi_c(\boldsymbol{r_e}, n_x, n_y, n_z). \tag{2.41}$$

2.3.2 Energy Spectrum of Excitons in Nanocrystals

The transition matrix element in nanocrystals is expressed as:

$$\begin{aligned} \left|M_{v-c}^{0D}\right|^2 &= \left| \langle c|\hat{\mathcal{V}}|v\rangle \right|^2 \\ &= \left| \langle u_c|\hat{\mathcal{V}}|u_v\rangle \right|^2 |\langle \phi_c|\phi_v\rangle|^2. \end{aligned} \tag{2.42}$$

In the case of infinite barrier potential induced in a cubic nanocrystal, $\phi_c(n_e)$ and $\phi_v(n_h)$ are orthogonal when $n_e \neq n_h$. In other words, the simple selection rule $\Delta n = 0$ needs to be satisfied in order for an optical transition to occur. This selection rule may vary with the NC sizes and shapes.

Since both electrons and holes are confined in a finite space of the NC, they can always couple to form excitons. Assuming that the selection rule is satisfied (*i.e,* $n_e = n_h \equiv n_X$), the exciton energy spectrum can be constructed, in a similar way to Eq. (2.29), as:

$$E_X(n_X) = E_c - E_v = E_g + E_{\text{conf}} + \frac{\hbar^2\pi^2}{2\mu_X}\left(\frac{n_{X,x}^2}{L_x^2} + \frac{n_{X,y}^2}{L_y^2} + \frac{n_{X,z}^2}{L_z^2}\right), \tag{2.43}$$

where μ_X is the reduced mass of the exciton, E_g is the bandgap energy of the bulk.

The first effect of quantum confinement is the increase of the optical bandgap in nanocrystal structure increases as compared to the bulk counterpart by confinement energies (see Eq. (2.43)). It is experimentally reflected by the blueshift of the resonances in the absorption and emission spectra. The 'shift' is tunable by changing the NC composition and/or size ($1/L^2$). In strong confinement regime, when the nanocrystal sizes are comparable or smaller than the exciton Bohr radius in the bulk crystals (*i.e.,* $L \leq a_X$), an energy splitting of the spin-degenerate states can be observed due to the enhanced e-h exchange interaction and spin-orbit coupling. The brightness of the split states and the bright-dark order rely on the symmetry of the states involved, which varies with different materials. For example, in conventional II-V semiconductor nanocrystals, the exciton ground-state is dark [21], while it is a bright state in perovskite nanocrystals [22].

2.3.3 Nonlinear Optical Processes in Nanocrystals

In previous sections, we have discussed the absorption of photon with energy above the bandgap, which is proportional to the wavefunction overlap and the density of the

states lying in the continuum bands. On the other hand, low-energy photons can also be absorbed but with much lower probability. In order to fulfill the energy conservation, multiple low-energy photons or internal energy need to be absorbed to excite valence electrons to conduction band.

(a) Multiple-Photon Absorption

In experiment, the strength of muliple-photon absorption processes are normally quantified by the multi-photon cross-section, expressed as [23]:

$$\sigma_{cv} = \frac{|\mu_{ci}\mu_{iv}|^2}{4\varepsilon_0^2\hbar^2c^2\Gamma^2}, \tag{2.44}$$

where i denotes the intermediate state between c and v, Γ is the linewidth of the final state and μ_{ci} and μ_{iv} are the transition dipole moments between the corresponding states. The absorption cross-section varies with different materials. Efficient multi-photon absorption has been achieved by employing core-shell structures in II-VI [24, 25] and perovskite core-shell nanocrystals [26].

(b) Phonon-Assisted Absorption in Nanocrystals

In a crystalline semiconductor, the atoms are arranged in a periodic lattice and vibrate around their own equilibrium positions forming a wave. The quantum of the lattice vibration is called as 'phonon'. Depending on the displacement direction of the atoms with respect to each other and to the propagation wavevector, phonons can be classified into optical and acoustic phonons, each of which can have longitudinal and transverse modes. In polar semiconductors such as GaAs and lead halide perovskites, as long as the optical phonon population is sufficient, the electron scatters more strongly with optical phonons through Fröhlich interaction rather than with acoustic modes.

The interaction between an electron at the state $|\boldsymbol{k}\rangle$ and a phonon at the state $|\boldsymbol{k}_{\mathbf{ph}}\rangle$ brings the system to a new electron $|\boldsymbol{k'}\rangle$ and phonon state $\left|\boldsymbol{k}'_{\mathbf{ph}}\right\rangle$. The scattering rate can be evaluated by Fermi golden rule as [27]:

$$S_{\mathrm{e-ph}}(\boldsymbol{k}, \boldsymbol{k}_{\mathbf{ph}}) = \frac{2\pi}{\hbar}\sum_{\boldsymbol{k}_{\mathbf{ph}}} |M_{\mathrm{e-ph}}(\boldsymbol{k}_{\mathbf{ph}})|^2\delta(E(\boldsymbol{k'}) - E(\boldsymbol{k}) \pm \hbar\omega_{\mathrm{ph}}), \tag{2.45}$$

where $\hbar\omega_{\mathrm{ph}}$ is the phonon energy and $M_{\mathrm{e-ph}}(\boldsymbol{k}_{\mathbf{ph}}) = \left\langle \boldsymbol{k'}, \boldsymbol{k}'_{\mathbf{ph}}\right|\hat{\mathcal{V}}_{\mathrm{e-ph}}\left|\boldsymbol{k}, \boldsymbol{k}_{\mathbf{ph}}\right\rangle$ is the transition matrix.

For Fröhlich interaction, the perturbation operator is written as:

$$\hat{\mathcal{V}}_{\mathrm{Fr}} = \sum_{\boldsymbol{k}_{\mathbf{ph}}} \frac{C}{|\boldsymbol{k}_{\mathbf{ph}}|}(a_{\boldsymbol{k}_{\mathbf{ph}}} e^{i\boldsymbol{k}_{\mathbf{ph}}.\boldsymbol{d}} - a^{\dagger}_{\boldsymbol{k}_{\mathbf{ph}}} e^{-i\boldsymbol{k}_{\mathbf{ph}}.\boldsymbol{d}}), \tag{2.46}$$

where C is a constant, $a_{\boldsymbol{k}_{\mathbf{ph}}}$ and $a^{\dagger}_{\boldsymbol{k}_{\mathbf{ph}}}$ are lowering and raising operators, respectively, $\boldsymbol{d}$ is the displacement of the atoms. The expression of $\hat{\mathcal{V}}_{\mathrm{Fr}}$ reveals the preferential coupling of carriers with longitudinal phonon modes when $\boldsymbol{k}_{\mathbf{ph}} \parallel \boldsymbol{d}$, but not with transverse modes, when $\boldsymbol{k}_{\mathbf{ph}} \perp \boldsymbol{d}$.

In nanocrystals, both carrier and phonon spectra are altered by spatial confinement. Hence, their interaction will be markedly affected. The confinement of the electron motion within a small region will enhance the probability of electron-phonon scattering, and the momentum conservation is relaxed. In nanocrystals, the electron-phonon scattering rate increases with decreasing size [27]. Furthermore, by engineering the interface of the nanocrystals, we can manipulate the interfacial phonon energy to match with the energy difference between the electron levels. For example, the GaAs nanocrystals have typical interface phonon energy of few meV; however, embedding the GaAs nanocrystal in AlAs can boost the interfacial phonon energy to 50 meV. In addition, the manipulation of the phonon spectrum can also promote the phonon-phonon scattering processes that in turn, may improve the electron-phonon interaction probability.

2.4 Lead Halide Peorvskite Semiconductors

Lead halide perovskite (LHP) semiconductors have shown a tremendous impact in a short period of time, in several optoelectronic applications such as efficient light-energy harvesting in low-cost solar cells [28–30], light-emitting devices [31–36], nanolasers [37–39], photodetectors [40–42] and optical refrigerators [43]. Due to their large interband dipole moment, LHPs generally exhibit strong photoluminescence (PL) whose emission wavelength is tunable from near-ultraviolet to near-infrared regions, by varying the chemical constituents or by alloying the halogen elements [37, 38, 44–48]. The excellent optical and electrical properties together with the giant tunability make perovskites a rich system for studying the fundamental physics as well as for developing novel applications. In this section, perovskite crystal structures, recent progress on the sample fabrication and electronic band structure will be introduced.

2.4.1 Perovskite Crystal Structures

'Perovskite' was initially named for the mineral calcium titanium oxide mineral ($CaTiO_3$) by the name of a Russian mineralogist Lev Perovski. Its name was then given for a family of materials sharing similar crystal structure AMX_3 and satisfying a condition: $R_A + R_M = t \times \sqrt{R_M + R_X}$, where R_A, R_M, R_X are the radii of the ions A^+, M^{2+}, X^-, respectively. The tolerance factor t is typically within 0.8 to 1.0 [49]. Back to history, the first synthesis of hybrid organic-inorganic perovskites was reported by Remy and Laves in 1933 [50] for copper-based perovskites (M = Cu). In the 1980s, copper was replaced by lead (M = Pb) and tin (M = Sn) by Weber [51, 52]. The anion X^- is a halide such as I^-, Br^-, Cl^- or their alloying form. The cation A^+, which neutralizes the charge in the structure, can be a monovalent metal such as Cs^+ or organic ions such as methylammonium ($CH_3NH_3^+$ = MA^+), formamidinium ($CH(NH_2)_2^+$) = FA^+).

Metal halide perovskites were first proved to be a new family of semiconductor materials in 1994 by Mitzi and his colleagues [8]. In 2009, lead halide perovskites have been successfully integrated into a solar cell by Kojima *et al.* with a solar energy conversion efficiency of 3.8%. Since then, perovskite semiconductors have attracted rapidly increasing attention. After ten years, the perovskite-based solar cell efficiency has been pushed to 24%, which can compete with the traditional silicon solar cells (26%) [53]. Other applications, especially in light-emitting devices, have been developed rigorously with external efficiency of above 20% [36, 54]. However, the use of toxic cations as Pb raises serious concerns to find an alternative cations for M. The most promising replacement for Pb is tin (Sn) as well as other metals in group 14. However, the highest recorded power-conversion efficiency of the tin-based solar cell is only 6% [55, 56], and the poorer chemical stability of those alternatives is also a big issue. Up to date, there has not been an optimal solution for nontoxic yet high-efficiency perovskite devices.

Figure 2.5 depicts the crystal structure of lead halide perovskites. Each lead atom is surrounded by six halogen atoms to form an octahedron, which is connected with six neighbouring octahedra at its vertices. In the corner-sharing MX_6^- octahedral framework, the vacancies are filled by either organic ($CH_3NH_3^+$, $CH(NH_2)_2^+$), or inorganic cations (Cs^+). These perovskite structures exist in different crystal phases, depending on external conditions such as pressure or temperature [57–59]. For instance, $CH_3NH_3PbBr_3$ transforms from the orthorhombic phase at below 150 K to the tetragonal phase at 150

K to 240 K and exists in the cubic phase at above 240 K [60].

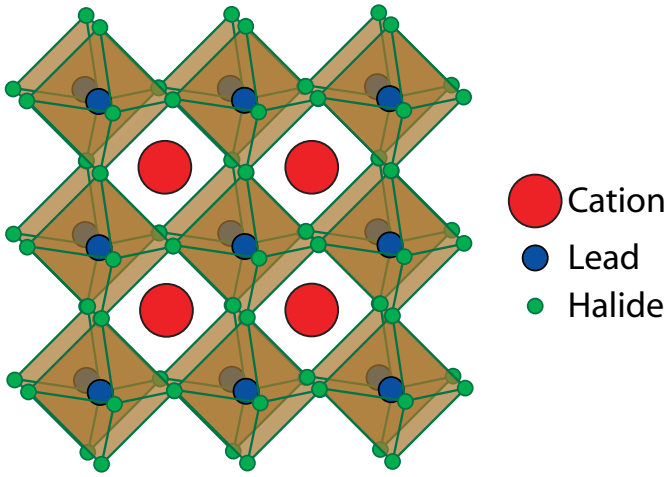

Figure 2.5: Perovskite crystal structures. One lead (blue circles) and six halide (green circles) ions form an octahedron, which shares its corners with the other six octahedra. In order to balance the charge, cations (red circles) are located at the vacancies of the lead halide framework.

2.4.2 Synthesis of Perovskite Crystals

Perovskite crystals can be synthesized in bulk or low-dimensional (quantum-wells, nanowires, nanocrystals) structure by chemical methods. Three-dimensional perovskites can be fabricated by vacuum- and high-temperature synthesis techniques such as one-step spin-coating [61] followed by hot drop-casting [62], two-step spin-coating lead halide solution followed by intercalation [63], intramolecular exchange [64], chemical vapor deposition [46] and so on. These methods produce polycrystalline thin films with the typical thickness of hundreds nanometers. On the other hand, high-quality bulk single crystals have been obtained by inverse temperature crystallization method [65], which provides millimeter-sized crystals with flat surfaces for the optical study of fundamental properties. Furthermore, single crystals can greatly reduce grain boundaries as well as trap states, which usually appear on polycrystalline thin films.

The synthesis of perovskite nanostructures such as quantum-wells or nanocrystals are also widely reported. A common strategy to synthesize such nano-sized crystals is using appropriate surfactants to restrict the growth of the crystals along certain directions. Long-chain organic ligands, such as butylamine [66, 67], phenethylamine [68], are most frequently used to produce high-quality 2D single crystals with high throughput and good reproducibility. Similarly, perovskite colloidal nanocrystals can be synthesized under

ambient conditions. The standard procedure was introduced by Protesescu *et al.* in 2015 [69]. Long-chain alkyl reagents such as oleylamine, octadecene and oleic acid are introduced to restrict the crystal growth in all three dimensions that allows the formation of nanometer-size crystals.

2.4.3 Electronic Band Structures

Despite a large possibility of varying the compositions, all the perovskite semiconductors share similar electronic structures [70–73]. Their band structures are mainly constructed from the [PbX_6] units, where the top valence band is mainly contributed by *s*-orbitals of Pb and the bottom conduction band comprises *p*-orbitals of both Pb and X [74, 75]. The inverted order of the atomic contribution (*p*-like conduction band, *s*-like valence band) makes perovskites distinguishable from conventional (group II-VI, III-V) semiconductors. For example, the bandgap becomes larger with increasing temperature [76] that is in clear contrast to the redshift of the transition energies in conventional semiconductors. Furthermore, the energetic order of bright and dark states is inverted [22] from that in II-V nanocrystals.

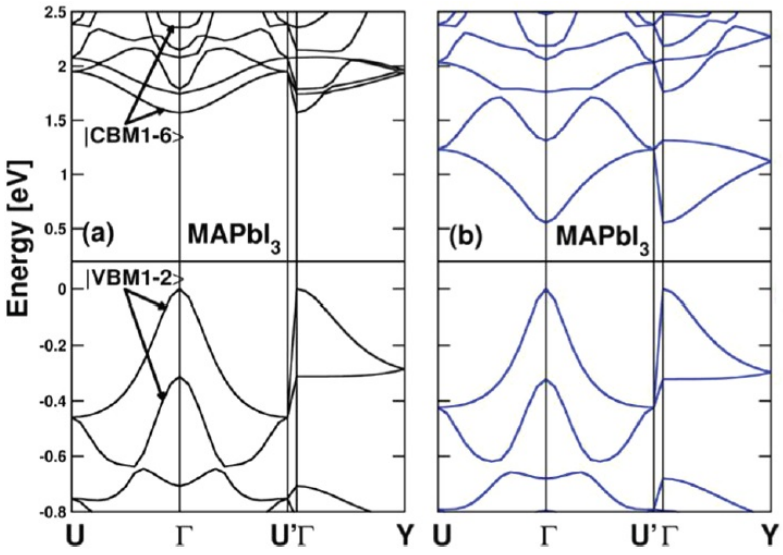

Figure 2.6: Electronic band structures of $CH_3NH_3PbI_3$ perovskite semiconductors at low-temperature orthohombic phase calculated by DFT. Two cases: (a) no spin-orbit coupling and (b) with spin-orbit coupling are taken into consideration. The figure is adapted with permission from Ref. [77]. Copyright 2013 American Chemical Society.

Figure 2.6(a) shows the electronic band structure of $CH_3NH_3PbI_3$ calculated for low-temperature orthohombic phase using density functional density (DFT) method. The fundamental bandgap is predicted at the Γ-point. At high temperatures, perovskite

crystals undergo phase transitions from orthohombic to tetragonal and cubic phases that causes sudden changes on the bandgap as well as the electronic band structures. In particular, the direct bandgap of $APbX_3$ perovskites is located at the Γ- and R-points in the Brillouin zone for orthohombic and cubic phases, respectively [22, 71, 78, 79]. Moreover, in heavy-metal containing semiconductors such as Pb, large spin-orbit coupling [77, 80–82] is expected that causes a huge reduction of the bandgap as shown in Fig. 2.6(b). In perovskite materials, the spin-orbit splitting can be up to $\sim$0.5-1.0 eV.

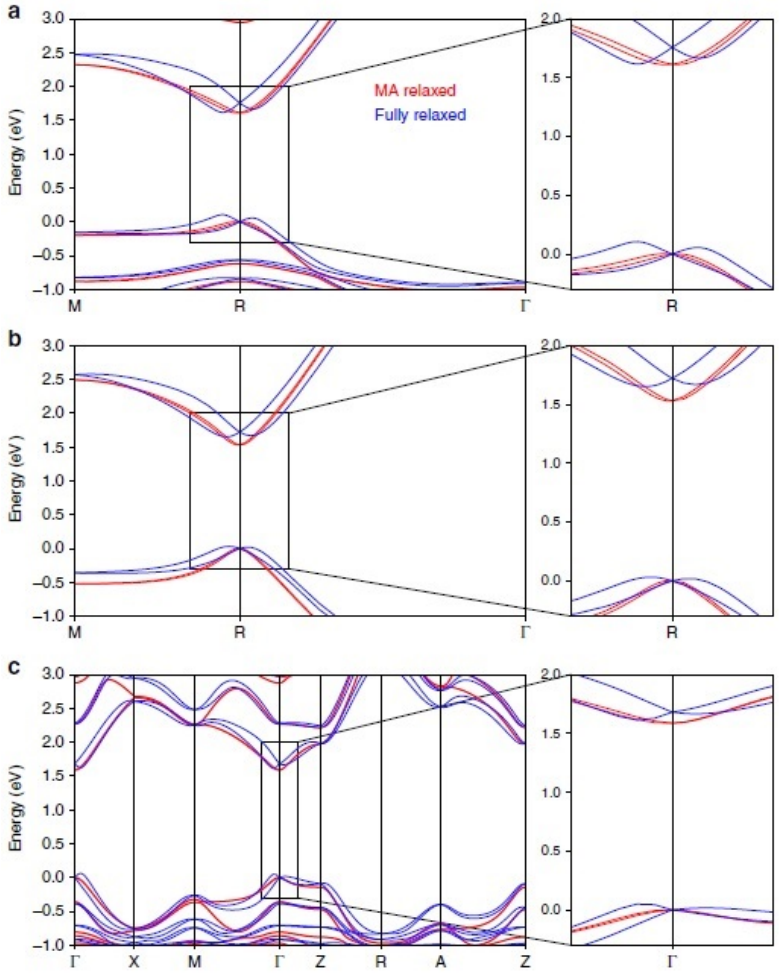

Figure 2.7: Electronic band structures of $CH_3NH_3PbI_3$ perovskite semiconductors at cubic phase computed by density functional theory (DFT) using (a) LDA and (b) HSE approximations. The results are obtained by accounting for two relaxation cases of the organic molecule $CH_3NH_3^+$ (MA^+) only (red lines) and of the whole structure (blue lines). (c) Band structures calculated for tetragonal supercells. Right panels: zoom-in view of the fundamental bandedges, showing Rashba splitting for all the crystal phases. The figure is adapted with permission from Ref. [83].

The calculation shown in Fig. 2.6, however, does not consider the relativistic spin-orbit coupling (Rashba) effects, which arises from the broken inversion symmetry of the crystal. In this regard, even though the cation A^+ does not directly contribute to

the bands, if A^+ is an organic species, the disorder and lattice dynamics can break the inversion symmetry and lead to Rashba effects [71, 84–86]. As a result, the spin-degenerate bands are shifted in k-space for both valence and conduction bands. The Rashba splitting has been predicted theoretically [83, 84, 87] and recently observed experimentally [88]. Figure 2.7 shows the DFT calculation for $CH_3NH_3PbI_3$ taking into account the structural effects at cubic (panel (a), (b)) and tetragonal phases (panel (c)). In all cases, Rashba-split bands are found. The calculated Rashba coefficient is in the order of $\sim$0.1 eVÅ, which is an order of magnitude smaller than the experimental results reported by Niesner *et al.* [88].

In addition, crystal field asymmetries and electron-hole exchange interactions [89] add to the plethora of physical parameters that need to be explored to fully understand the electronic energy landscape and optical transitions of these emergent semiconductors.

References

1. Mahan, G. D. *Condensed matter in a nutshell* (Princeton University Press, 2011).
2. Kittel, C., McEuen, P. & McEuen, P. *Introduction to solid state physics* (Wiley New York, 1976).
3. Yu, P. & Cardona, M. *Fundamentals of semiconductors: Physics and materials properties* (Springer, 2010).
4. Fox, M. *Optical properties of solids* (Oxford University Press, 2010).
5. Manfra, M. J. Molecular beam epitaxy of ultra-high-quality AlGaAs/GaAs heterostructures: Enabling physics in low-dimensional electronic systems. *Annu. Rev. Condens. Matter Phys.* **5,** 347–373 (2014).
6. Dong, J., Teng, J., Chua, S., Foo, B., Wang, Y. & Yin, R. MOCVD growth of 980 nm InGaAs/GaAs/AlGaAs graded index separate confinement heterostructure quantum well lasers with tertiarybutylarsine. *J. Cryst. Growth* **289,** 59–62 (2006).
7. Ishihara, T., Takahashi, J. & Goto, T. Optical properties due to electronic transitions in two-dimensional semiconductors $(C_nH_{2n+1}NH_3)_2$ PbI_4. *Phys. Rev. B* **42,** 11099 (1990).
8. Mitzi, D. B., Feild, C., Harrison, W. & Guloy, A. Conducting tin halides with a layered organic-based perovskite structure. *Nature* **369,** 467 (1994).

9. Klingshirn, C. F. *Semiconductor optics* (Springer Science & Business Media, 2012).

10. Hong, X., Ishihara, T. & Nurmikko, A. Dielectric confinement effect on excitons in PbI_4-based layered semiconductors. *Phys. Rev. B* **45,** 6961 (1992).

11. Qiu, D. Y., Felipe, H. & Louie, S. G. Optical spectrum of MoS_2: Many-body effects and diversity of exciton states. *Phys. Rev. Lett.* **111,** 216805 (2013).

12. Chernikov, A., Berkelbach, T. C., Hill, H. M., Rigosi, A., Li, Y., Aslan, O. B., Reichman, D. R., Hybertsen, M. S. & Heinz, T. F. Exciton binding energy and nonhydrogenic Rydberg series in monolayer WS_2. *Phys. Rev. Lett.* **113,** 076802 (2014).

13. Jiang, Z., Liu, Z., Li, Y. & Duan, W. Scaling universality between band gap and exciton binding energy of two-dimensional semiconductors. *Phys. Rev. Lett.* **118,** 266401 (2017).

14. Blancon, J.-C. *et al.* Scaling law for excitons in 2D perovskite quantum wells. *Nat. Commun.* **9,** 2254 (2018).

15. Andreani, L. C. & Bassani, F. Exchange interaction and polariton effects in quantum-well excitons. *Phys. Rev. B* **41,** 7536 (1990).

16. Jorda, S., Rössler, U. & Broido, D. Fine structure of excitons and polariton dispersion in quantum wells. *Phys. Rev. B* **48,** 1669 (1993).

17. Burstein, E. & Weisbuch, C. *Confined electrons and photons: New physics and applications* (Springer Science & Business Media, 2012).

18. Julier, M., Campo, J., Gil, B., Lascaray, J. & Nakamura, S. Determination of the spin-exchange interaction constant in wurtzite GaN. *Phys. Rev. B* **57,** R6791 (1998).

19. Ekardt, W., Lösch, K. & Bimberg, D. Determination of the analytical and the nonanalytical part of the exchange interaction of InP and GaAs from polariton spectra in intermediate magnetic fields. *Phys. Rev. B* **20,** 3303 (1979).

20. Gil, B., Lefebvre, P., Bretagnon, T., Guillet, T., Sans, J., Taliercio, T. & Morhain, C. Spin-exchange interaction in ZnO-based quantum wells. *Phys. Rev. B* **74,** 153302 (2006).

21. Nirmal, M., Norris, D. J., Kuno, M., Bawendi, M. G., Efros, A. L. & Rosen, M. Observation of the “dark exciton" in CdSe quantum dots. *Phys. Rev. Lett.* **75,** 3728 (1995).

22. Becker, M. A., Vaxenburg, R., Nedelcu, G., Sercel, P. C., Shabaev, A., Mehl, M. J., Michopoulos, J. G., Lambrakos, S. G., Bernstein, N., Lyons, J. L., *et al.* Bright triplet excitons in caesium lead halide perovskites. *Nature* **553,** 189 (2018).

23. Boyd, R. W. *Nonlinear optics* (Elsevier, 2003).

24. Morello, G., Della Sala, F., Carbone, L., Manna, L., Maruccio, G., Cingolani, R. & De Giorgi, M. Intrinsic optical nonlinearity in colloidal seeded grown CdSe/CdS nanostructures: Photoinduced screening of the internal electric field. *Phys. Rev. B* **78,** 195313 (2008).

25. Xing, G., Chakrabortty, S., Chou, K. L., Mishra, N., Huan, C. H. A., Chan, Y. & Sum, T. C. Enhanced tunability of the multiphoton absorption cross-section in seeded CdSe/CdS nanorod heterostructures. *Appl. Phys. Lett.* **97,** 061112 (2010).

26. Chen, W., Bhaumik, S., Veldhuis, S. A., Xing, G., Xu, Q., Grätzel, M., Mhaisalkar, S., Mathews, N. & Sum, T. C. Giant five-photon absorption from multidimensional core-shell halide perovskite colloidal nanocrystals. *Nat. Commun.* **8,** 15198 (2017).

27. Stroscio, M. A. & Dutta, M. *Phonons in nanostructures* (Cambridge University Press, 2001).

28. Kojima, A., Teshima, K., Shirai, Y. & Miyasaka, T. Organometal halide perovskites as visible-light sensitizers for photovoltaic cells. *J. Am. Chem. Soc.* **131,** 6050–6051 (2009).

29. Lee, M. M., Teuscher, J., Miyasaka, T., Murakami, T. N. & Snaith, H. J. Efficient hybrid solar cells based on meso-superstructured organometal halide perovskites. *Science* **338,** 643–647 (2012).

30. Stranks, S. D., Eperon, G. E., Grancini, G., Menelaou, C., Alcocer, M. J., Leijtens, T., Herz, L. M., Petrozza, A. & Snaith, H. J. Electron-hole diffusion lengths exceeding 1 micrometer in an organometal trihalide perovskite absorber. *Science* **342,** 341–344 (2013).

31. Tan, Z. K. *et al.* Bright light-emitting diodes based on organometal halide perovskite. *Nat. Nanotech.* **9,** 687–692 (2014).

32. Cho, H. *et al.* Overcoming the electroluminescence efficiency limitations of perovskite light-emitting diodes. *Science* **350,** 1222–1225 (2015).

33. Ling, Y., Yuan, Z., Tian, Y., Wang, X., Wang, J. C., Xin, Y., Hanson, K., Ma, B. & Gao, H. Bright light-emitting diodes based on organometal halide perovskite nanoplatelets. *Adv. Mater.* **28,** 305–311 (2016).

34. Yassitepe, E. *et al.* Amine-free synthesis of cesium lead halide perovskite quantum dots for efficient light-emitting diodes. *Adv. Funct. Mater.* **26,** 8757–8763 (2016).

35. Xing, J. *et al.* High-efficiency light-emitting diodes of organometal halide perovskite amorphous nanoparticles. *ACS Nano* **10,** 6623–6630 (2016).

36. Lin, K., Xing, J., Quan, L. N., de Arquer, F. P. G., Gong, X., Lu, J., Xie, L., Zhao, W., Zhang, D., Yan, C., *et al.* Perovskite light-emitting diodes with external quantum efficiency exceeding 20 percent. *Nature* **562,** 245 (2018).

37. Zhang, Q., Ha, S. T., Liu, X., Sum, T. C. & Xiong, Q. Room-temperature near-infrared high-Q perovskite whispering-gallery planar nanolasers. *Nano Lett.* **14,** 5995–6001 (2014).

38. Xing, G., Mathews, N., Lim, S. S., Yantara, N., Liu, X., Sabba, D., Grätzel, M., Mhaisalkar, S. & Sum, T. C. Low-temperature solution-processed wavelength-tunable perovskites for lasing. *Nat. Mater.* **13,** 476–480 (2014).

39. Zhu, H., Fu, Y., Meng, F., Wu, X., Gong, Z., Ding, Q., Gustafsson, M. V., Trinh, M. T., Jin, S. & Zhu, X. Lead halide perovskite nanowire lasers with low lasing thresholds and high quality factors. *Nat. Mater.* **14,** 636–642 (2015).

40. Dou, L., Yang, Y. M., You, J., Hong, Z., Chang, W.-H., Li, G. & Yang, Y. Solution-processed hybrid perovskite photodetectors with high detectivity. *Nat. Commun.* **5** (2014).

41. Fang, Y., Dong, Q., Shao, Y., Yuan, Y. & Huang, J. Highly narrowband perovskite single-crystal photodetectors enabled by surface-charge recombination. *Nat. Photonics* **9,** 679–686 (2015).

42. Sutherland, B. R., Johnston, A. K., Ip, A. H., Xu, J., Adinolfi, V., Kanjanaboos, P. & Sargent, E. H. Sensitive, fast, and stable perovskite photodetectors exploiting interface engineering. *ACS Photonics* **2,** 1117–1123 (2015).

43. Ha, S. T., Shen, C., Zhang, J. & Xiong, Q. Laser cooling of organic–inorganic lead halide perovskites. *Nat. Photonics* **10,** 115 (2016).

44. Kitazawa, N., Watanabe, Y. & Nakamura, Y. Optical properties of $CH_3NH_3PbX_3$ (X=halogen) and their mixed-halide crystals. *J. Mater. Sci.* **37,** 3585–3587 (2002).

45. Noh, J. H., Im, S. H., Heo, J. H., Mandal, T. N. & Seok, S. I. Chemical management for colorful, efficient, and stable inorganic–organic hybrid nanostructured solar cells. *Nano Lett.* **13,** 1764–1769 (2013).

46. Ha, S. T., Liu, X., Zhang, Q., Giovanni, D., Sum, T. C. & Xiong, Q. H. Synthesis of organic-inorganic lead halide perovskite nanoplatelets: Towards high-performance perovskite solar cells and optoelectronic devices. *Adv. Opt. Mater.* **2,** 838–844 (2014).

47. Comin, R., Walters, G., Thibau, E. S., Voznyy, O., Lu, Z.-H. & Sargent, E. H. Structural, optical, and electronic studies of wide-bandgap lead halide perovskites. *J. Mater. Chem. C* **3,** 8839–8843 (2015).

48. Jeon, N. J., Noh, J. H., Yang, W. S., Kim, Y. C., Ryu, S., Seo, J. & Seok, S. I. Compositional engineering of perovskite materials for high-performance solar cells. *Nature* **517,** 476–480 (2015).

49. Goldschmidt, V. M. Die gesetze der krystallochemie. *Naturwissenschaften* **14,** 477–485 (1926).

50. Remy, H. & Laves, G. Über Chlorokomplexsalze des zweiwertigen Kupfers. *EurJC* **66,** 401–407 (1933).

51. Weber, D. $CH_3NH_3PbX_3$, ein Pb (II)-system mit kubischer perowskitstruktur/ $CH_3NH_3PbX_3$, a Pb(II)-system with cubic perovskite structure. *Z. Naturforsch. B, J. Chem. Sci.* **33,** 1443–1445 (1978).

52. Weber, D. $CH_3NH_3SnBr_xI_{3-x}$ (x = 0-3), ein Sn(II)-system mit kubischer Perowskitstruktur. *Z. Naturforsch. B, J. Chem. Sci.* **33,** 862–865 (1978).

53. `https://www.nrel.gov/pv/assets/pdfs/pv-efficiency-chart.20181221.pdf`.

54. Cao, Y., Wang, N., Tian, H., Guo, J., Wei, Y., Chen, H., Miao, Y., Zou, W., Pan, K., He, Y., *et al.* Perovskite light-emitting diodes based on spontaneously formed submicrometre-scale structures. *Nature* **562,** 249 (2018).

55. Noel, N. K., Stranks, S. D., Abate, A., Wehrenfennig, C., Guarnera, S., Haghighirad, A.-A., Sadhanala, A., Eperon, G. E., Pathak, S. K., Johnston, M. B., *et al.* Lead-free organic–inorganic tin halide perovskites for photovoltaic applications. *Energy Environ. Sci.* **7,** 3061–3068 (2014).

56. Hao, F., Stoumpos, C. C., Cao, D. H., Chang, R. P. & Kanatzidis, M. G. Lead-free solid-state organic–inorganic halide perovskite solar cells. *Nat. Photonics* **8,** 489 (2014).

57. Gesi, K. Effect of hydrostatic pressure on the structural phase transitions in CH_3NH_3 PbX_3 (X = Cl, Br, I). *Ferroelectrics* **203,** 249–268 (1997).

58. Frost, J. M. & Walsh, A. What is moving in hybrid halide perovskite solar cells? *Acc. Chem. Res.* **49,** 528–535 (2016).

59. Wang, T., Daiber, B., Frost, J. M., Mann, S., Garnett, E., Walsh, A. & Ehrler, B. Indirect to direct bandgap transition in methylammonium lead halide perovskite. *Energy Environ. Sci.* DOI: 10.1039/c6ee03474h (2017).

60. Onoda-Yamamuro, N., Matsuo, T. & Suga, H. Calorimetric and IR spectroscopic studies of phase transitions in methylammonium trihalogenoplumbates (II)†. *J. Phys. Chem. Solids* **51,** 1383–1395 (1990).

61. Jeon, N. J., Noh, J. H., Kim, Y. C., Yang, W. S., Ryu, S. & Seok, S. I. Solvent engineering for high-performance inorganic–organic hybrid perovskite solar cells. *Nat. Mater.* **13,** 897 (2014).

62. Nie, W., Tsai, H., Asadpour, R., Blancon, J.-C., Neukirch, A. J., Gupta, G., Crochet, J. J., Chhowalla, M., Tretiak, S., Alam, M. A., *et al.* High-efficiency solution-processed perovskite solar cells with millimeter-scale grains. *Science* **347,** 522–525 (2015).

63. Burschka, J., Pellet, N., Moon, S.-J., Humphry-Baker, R., Gao, P., Nazeeruddin, M. K. & Grätzel, M. Sequential deposition as a route to high-performance perovskite-sensitized solar cells. *Nature* **499,** 316 (2013).

64. Yang, W. S., Noh, J. H., Jeon, N. J., Kim, Y. C., Ryu, S., Seo, J. & Seok, S. I. High-performance photovoltaic perovskite layers fabricated through intramolecular exchange. *Science* **348,** 1234–1237 (2015).

65. Saidaminov, M. I., Abdelhady, A. L., Murali, B., Alarousu, E., Burlakov, V. M., Peng, W., Dursun, I., Wang, L., He, Y., Maculan, G., *et al.* High-quality bulk hybrid perovskite single crystals within minutes by inverse temperature crystallization. *Nat. Commun.* **6,** 7586 (2015).

66. Dou, L., Wong, A. B., Yu, Y., Lai, M., Kornienko, N., Eaton, S. W., Fu, A., Bischak, C. G., Ma, J., Ding, T., *et al.* Atomically thin two-dimensional organic-inorganic hybrid perovskites. *Science* **349,** 1518–1521 (2015).

67. Tsai, H., Nie, W., Blancon, J.-C., Stoumpos, C. C., Asadpour, R., Harutyunyan, B., Neukirch, A. J., Verduzco, R., Crochet, J. J., Tretiak, S., *et al.* High-efficiency two-dimensional Ruddlesden–Popper perovskite solar cells. *Nature* **536,** 312 (2016).

68. Fu, W., Wang, J., Zuo, L., Gao, K., Liu, F., Ginger, D. S. & Jen, A. K.-Y. Two-dimensional perovskite solar cells with 14.1% power conversion efficiency and 0.68% external radiative efficiency. *ACS Energy Lett.* **3,** 2086–2093 (2018).

69. Protesescu, L., Yakunin, S., Bodnarchuk, M. I., Krieg, F., Caputo, R., Hendon, C. H., Yang, R. X., Walsh, A. & Kovalenko, M. V. Nanocrystals of cesium lead halide perovskites ($CsPbX_3$, X=Cl, Br, and I): Novel optoelectronic materials showing bright emission with wide color gamut. *Nano Lett.* **15,** 3692–3696 (2015).

70. Even, J., Pedesseau, L., Jancu, J.-M. & Katan, C. DFT and k.p modelling of the phase transitions of lead and tin halide perovskites for photovoltaic cells. *Phys. Status Solidi* **8,** 31–35 (2014).

71. Even, J., Pedesseau, L., Katan, C., Kepenekian, M., Lauret, J.-S., Sapori, D. & Deleporte, E. Solid-state physics perspective on hybrid perovskite semiconductors. *J. Phys. Chem. C* **119,** 10161–10177 (2015).

72. Jishi, R. A., Ta, O. B. & Sharif, A. A. Modeling of lead halide perovskites for photovoltaic applications. *J. Phys. Chem. C* **118,** 28344–28349 (2014).

73. He, Y. & Galli, G. Perovskites for solar thermoelectric applications: A first principle study of $CH_3NH_3AI_3$ (A=Pb and Sn). *Chem. Mater.* **26,** 5394–5400 (2014).

74. Umebayashi, T., Asai, K., Kondo, T. & Nakao, A. Electronic structures of lead iodide based low-dimensional crystals. *Phys. Rev. B* **67,** 155405 (2003).

75. Brandt, R. E., Stevanović, V., Ginley, D. S. & Buonassisi, T. Identifying defect-tolerant semiconductors with high minority-carrier lifetimes: Beyond hybrid lead halide perovskites. *MRS Commun.* **5,** 265–275 (2015).

76. Do, T. T. H., Granados del Águila, A., Cui, C., Xing, J., Ning, Z. & Xiong, Q. Optical study on intrinsic exciton states in high-quality $CH_3NH_3PbBr_3$ single crystals. *Phys. Rev. B* **96,** 075308 (2017).

77. Even, J., Pedesseau, L., Jancu, J. M. & Katan, C. Importance of spin-orbit coupling in hybrid organic/inorganic perovskites for photovoltaic applications. *J. Phys. Chem. Lett.* **4,** 2999–3005 (2013).

78. Baikie, T., Fang, Y., Kadro, J. M., Schreyer, M., Wei, F., Mhaisalkar, S. G., Grätzel, M. & White, T. J. Synthesis and crystal chemistry of the hybrid perovskite $(CH_3NH_3)PbI_3$ for solid-state sensitised solar cell applications. *J. Mater. Chem. A* **1,** 5628–5641 (2013).

79. Geng, W., Zhang, L., Zhang, Y.-N., Lau, W.-M. & Liu, L.-M. First-principles study of lead iodide perovskite tetragonal and orthorhombic phases for photovoltaics. *J. Phys. Chem. C* **118,** 19565–19571 (2014).

80. Brivio, F., Butler, K. T., Walsh, A. & Van Schilfgaarde, M. Relativistic quasiparticle self-consistent electronic structure of hybrid halide perovskite photovoltaic absorbers. *Phys. Rev. B* **89,** 155204 (2014).

81. Amat, A., Mosconi, E., Ronca, E., Quarti, C., Umari, P., Nazeeruddin, M. K., Grätzel, M. & De Angelis, F. Cation-induced band-gap tuning in organohalide perovskites: interplay of spin–orbit coupling and octahedra tilting. *Nano Lett.* **14,** 3608–3616 (2014).

82. Filip, M. R. & Giustino, F. GW quasiparticle band gap of the hybrid organic-inorganic perovskite $CH_3NH_3PbI_3$: Effect of spin-orbit interaction, semicore electrons, and self-consistency. *Phys. Rev. B* **90,** 245145 (2014).

83. Frohna, K., Deshpande, T., Harter, J., Peng, W., Barker, B. A., Neaton, J. B., Louie, S. G., Bakr, O. M., Hsieh, D. & Bernardi, M. Inversion symmetry and bulk Rashba effect in methylammonium lead iodide perovskite single crystals. *Nat. Commun.* **9,** 1829 (2018).

84. Azarhoosh, P., McKechnie, S., Frost, J. M., Walsh, A. & Van Schilfgaarde, M. Research update: Relativistic origin of slow electron-hole recombination in hybrid halide perovskite solar cells. *APL Mater.* **4,** 091501 (2016).

85. Whalley, L. D., Frost, J. M., Jung, Y.-K. & Walsh, A. Perspective: Theory and simulation of hybrid halide perovskites. *J. Chem. Phys.* **146,** 220901 (2017).

86. Herz, L. M. How lattice dynamics moderate the electronic properties of metal-halide perovskites? *J. Phys. Chem. Lett.* **9,** 6853–6863 (2018).

87. Zheng, F., Tan, L. Z., Liu, S. & Rappe, A. M. Rashba spin–orbit coupling enhanced carrier lifetime in $CH_3NH_3PbI_3$. *Nano Lett.* **15,** 7794–7800 (2015).

88. Niesner, D., Wilhelm, M., Levchuk, I., Osvet, A., Shrestha, S., Batentschuk, M., Brabec, C. & Fauster, T. Giant Rashba splitting in $CH_3NH_3PbBr_3$ organic-inorganic perovskite. *Phys. Rev. Lett.* **117,** 126401 (2016).

89. Tanaka, K., Takahashi, T., Ban, T., Kondo, T., Uchida, K. & Miura, N. Comparative study on the excitons in lead-halide-based perovskite-type crystals $CH_3NH_3PbBr_3$ and $CH_3NH_3PbI_3$. *Solid State Commun.* **127,** 619–623 (2003).

Chapter 3

Optical Spectroscopy Techniques

The exciton properties of the lead halide perovskite semiconductors were studied by both steady-state and time-resolved spectroscopy techniques. In this chapter, the instrumentation used throughout this thesis will be introduced. The working principles of the techniques as well as the data analysis procedure will also be discussed.

3.1 Steady-State Absorption, Reflectance and Photoluminescence Spectroscopy

3.1.1 Experimental Setup

Absorption (A), reflection (R) and photoluminescence (PL) spectroscopy are standard and powerful techniques to study the photophysical properties of semiconductors. The absorption, reflection and emission processes are associated with the optically allowed transitions between valence and conduction bands. Furthermore, scattering processes can be also probed by near-resonant PL experiments that provides information of the forbidden transitions. Therefore, investigating how the semiconductors absorb and emit light will be important to understand the electronic band structures of semiconductors. Since reflection and photoluminescence are surface-sensitive, a flat surface is crucial. The grain boundaries and the roughness of the sample surface cause unexpected broadening that, in turn, may obscure spectral features, especially those having close energies.

A schematic representation of the steady-state absorption, reflection and photoluminescence measurements is shown in Fig. 3.1. In the absorption and reflection experiments, the sample was excited by unpolarized broadband light sources as represented by the dark-red and orange arrows, respectively. Whereas, in the PL measurements, a linearly polarized laser was used (blue arrow). The directions of excitation and detection, pointing along $\boldsymbol{k}_{\mathbf{Exc}}$ and $\boldsymbol{k}_{\mathbf{Det}}$), are both perpendicular to the sample surface. The

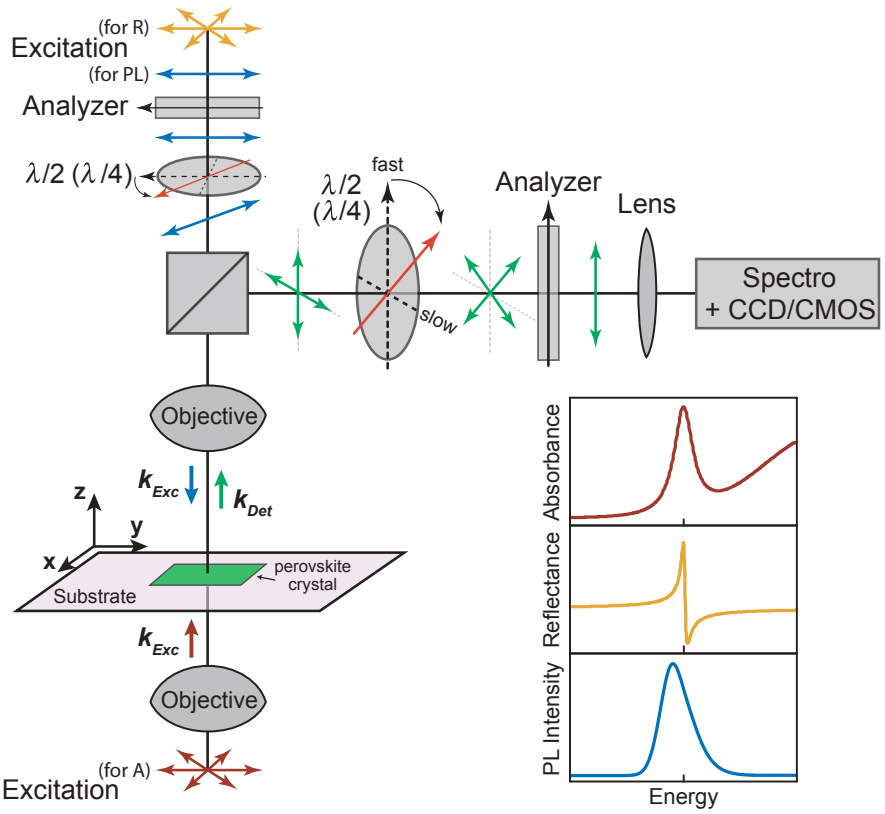

Figure 3.1: Schematic setup for absorption (A), reflection (R) and photoluminescence (PL) measurements. For absorption and reflection experiments, the sample was excited by unpolarized broadband light sources as represented by the dark-red and orange arrows, respectively. For PL measurements, a linearly polarized laser was used (blue arrow). The excitation beams were focused onto the sample surface through microscope objectives. The signal was dispersed by a single-grating spectrometer and detected by a CCD or CMOS camera. The directions of the excitation and detection are indicated by $\boldsymbol{k}_{\mathbf{Exc}}$ and $\boldsymbol{k}_{\mathbf{Det}}$. A polarizer set, including a linear polarizer (analyzer) and a $\lambda/2$ or $\lambda/4$ waveplate, can be installed to control the polarization of the excitation and detected photons. Examples for the lineshapes of the absorption, reflectance and PL spectra are shown by the dark-red, orange and blue curves, respectively.

excitation beams were focused onto the sample surface through microscope objectives. The optical signals were collected through an objective, dispersed by a single-grating spectrometer and recorded by a charged coupled device (CCD) or complementary metal-oxide semiconductor (CMOS) camera. The perovskite crystal was mounted in a cryostat fed by a continuous flow of liquid helium. The sample temperature can be controlled by a resistive heater integrated inside the cryostat.

For the polarization-resolved photoluminescence experiments, two sets of polarizers were separately used on the excitation and detection paths. In each set, a linear polarizer (analyzer) were used to calibrate the polarization response of the setup. The linear and

circular polarization of the photons were controlled by a half waveplate ($\lambda/2$) and a quarter waveplate ($\lambda/4$), respectively.

3.1.2 Absorption Spectra: Elliot Theory

The absorption profile of direct-bandgap semiconductors is discussed by Eq. (2.12)-(2.14) in Section 2.1.2. Considering the excitonic effects, the total absorption coefficient $\alpha_j(E)$ of the j^{th} transition includes the contributions from exciton bands expressed by the first term and the contribution from the continuum band given by the second term in Eq. (3.1) [1, 2]:

$$\alpha_j(E) = \frac{4\pi e^2\hbar}{\sqrt{\varepsilon}cEm_0^2}|M^j_{\text{v}-\text{c}}|^2\left(\frac{1}{a^3_{Xj}}\left[A_x(E_{g,j}-E_{b,j}-E)+\sum_{n>1}\frac{1}{n^3}A_b(E_{g,j}-\frac{E_{b,j}}{n^2}-E)\right]\right.$$
$$\left.+\left(\frac{2m^*_j}{\hbar^2}\right)^{3/2}\frac{\sqrt{E_{b,j}}}{2}\int_{E_{g,j}}^{\infty}\frac{A_b(E'-E)}{1-\exp\left[-2\pi\sqrt{E_{b,j}/(E'-E_{g,j})}\right]}dE'\right), \tag{3.1}$$

where E is the photon energy, ε is the static dielectric function; $M^j_{\text{v}-\text{c}}$ is the matrix element of the j-valence-conduction transition; a_{Xj} is the exciton radius, and m^*_j is the effective mass of the j-exciton. The energy of the n^{th}-exciton of the j-band can be expressed as $E_{g,j}-E_{b,j}/n^2$, where $E_{b,j}$ is the corresponding binding energy. In Eq. (3.1), the broadening of exciton and continuum band are described by A_x and A_b functions, respectively, which are either Lorentzian or Gaussian function. At much higher energies than binding energy (*i.e.* $E \gg E_{b,j}$), the continuum term reduces to $(E-E_{g,i})^{1/2}$ as deduced in Eq. (2.15). A typical absorption spectrum of a 3D crystal described by Elliot theory is shown in Fig. 3.1 by the dark-red curve.

3.1.3 Reflectance Spectra: Lorentz Model

Lorentz model considers each exciton as a single oscillating dipole, which has resonant energy of E_0. The oscillation is damped through the interaction between the carriers and phonons. The complex dielectric function $\widetilde{\varepsilon}(E)$ can be expressed as a sum of N oscillating dipoles with different resonance energies $E_{0,j}$ [3]:

$$\widetilde{\varepsilon}(E) = \varepsilon_\infty + \frac{\hbar^2 Ne^2}{\varepsilon_0 m_0}\sum_j \frac{F_j}{E^2_{0,j}-E^2-i\hbar\gamma_j E}, \tag{3.2}$$

where E is the photon energy, ε_∞ is the high-frequency dielectric constant, $\hbar$ is the reduced Planck constant, N is the total number of oscillating dipoles, e is free-electron charge, ε_0 is the electric permittivity of vacuum, m_0 is the free-electron rest mass, j denotes the j-optical transition whose resonance energy is $E_{0,j}$, γ_j is the j-linewidth and F_j is the j-oscillator strength that satisfies the sum rule $\sum_j F_j = 1$. The frequency-dependent refractive index is deduced by $\widetilde{n}(E) = \sqrt{\widetilde{\varepsilon}(E)}$. The real and imaginary parts of $\widetilde{n}(E)$ or $\widetilde{\varepsilon}(E)$) are essential for understanding the optical properties of materials, such as absorption and reflection. The absorption coefficient is correlated with the extinction coefficient (imaginary part of $\widetilde{n}(E)$) as $\alpha(E) = 4\pi\kappa E/hc$, where h is Planck constant and c is the light velocity in vacuum.

(a) In bulk medium

The reflectance of a semi-infinite medium can be directly calculated by an usual Fresnel equation given by [3]:

$$R(E) = \left|\frac{\widetilde{n}(E) - 1}{\widetilde{n}(E) + 1}\right|^2, \tag{3.3}$$

where the complex refractive index $\widetilde{n}(E)$ = $\sqrt{\widetilde{\varepsilon}(E)}$.

(b) In superlattice/multiple-quantum-well system

In a superlattice system, one needs to take into account the superposition of the exciton resonances and multiple reflection/transmission events at the interfaces. Schematic of an N-layer structure is shown in Fig. 3.2. The media are indexed by positive integers m, where m = 1, 2,..., N. In order to simulate the experimental conditions, we consider the first layer as vacuum (blank space), the alternatively stacked barriers (light-green rectangles) and wells (orange rectangles). The whole structure lies on a SiO_2/Si substrate (white and gray rectangles). The z-axis points downwards with the origin z = 0 at the first interface between the medium m = 1 and m = 2.

In the reflectance measurement using a backscattering configuration, both the incident and collected light are normal to the crystal plane. The light wave in the m^{th} medium is represented by the propagation wavevector $\boldsymbol{k_m}$ and the electric field $\boldsymbol{E_m}$. At the interfaces, a wave can either be transmitted or reflected. Therefore, in each medium m, there are two waves propagating along z-direction ($\boldsymbol{k_m}$, $\boldsymbol{E_m}$) and (-z)-direction ($\boldsymbol{k'_m}$, $\boldsymbol{E'_m}$).

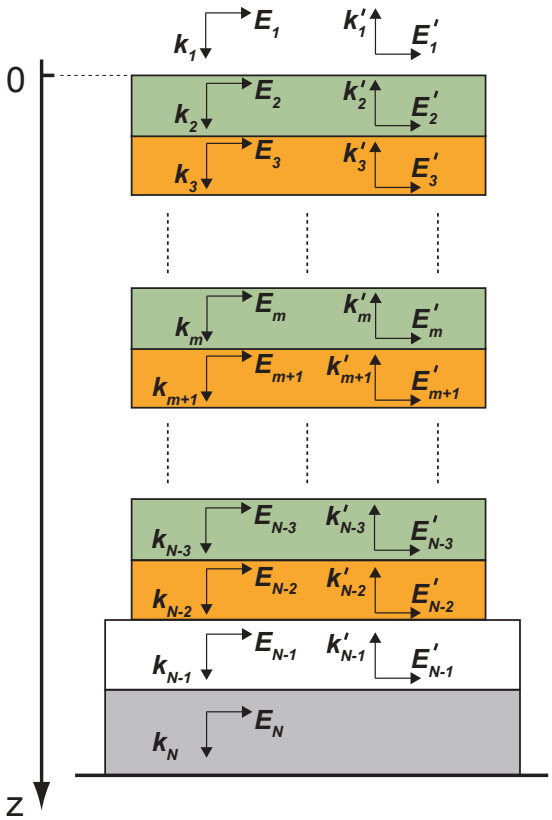

Figure 3.2: Schematic of an N-layer structure with the top vacuum (blank space), $(N-3)$ layers of alternatively stacked barriers (light-green rectangles) and wells (orange rectangles), a 285-nm-thick SiO_2 layer (white rectangle) on top of an infinitely thick Si medium (grey rectangle). The z-axis points downwards with the origin set at the first interface. The media are consecutively indexed by positive integers m, where m = 1, 2,..., N. Light waves propagating along z $(-z)$ direction are represented by the wavevector $\boldsymbol{k_m}$ $(\boldsymbol{k'_m})$ and electric field $\boldsymbol{E_m}$ $(\boldsymbol{E'_m})$.

At the interfaces, for example between m and $m+1$, boundary conditions of continuity have to be strictly met:

$$E_m + E'_m = E_{m+1} + E'_{m+1}, \tag{3.4}$$

$$\frac{dE_m}{dz} + \frac{dE'_m}{dz} = \frac{dE_{m+1}}{dz} + \frac{dE'_{m+1}}{dz}, \tag{3.5}$$

The electric fields propagating in the m^{th} medium reaching the interface between m^{th} and $(m+1)^{\text{th}}$ medium are expressed as $E_m = E_{0,m}\exp(ik_m z_{m,m+1})$ and $E'_m = E'_{0,m}\exp(-ik_m z_{m,m+1})$. In the expression, $k_m = kn_m = k\sqrt{\varepsilon_m}$ is the corresponding wavevector in medium m, where $k = |\boldsymbol{k_1}|$, $n_m = \sqrt{\varepsilon_m}$ is refractive index, where ε_m is dielectric function/constant, $z_{m,m+1} = \sum_{j=2}^{m} t_j$ is the position of the $(m, m+1)$-interface, where t_i is the thickness of individual media.

Solving equations (3.4)-(3.5) gives:

$$\begin{bmatrix} E_m \\ \\ E'_m \end{bmatrix} = M_{m,m+1} \begin{bmatrix} E_m \\ \\ E'_m \end{bmatrix} \tag{3.6}$$

where $M_{m,m+1}$ is the transfer matrix expressed as:

$$M_{m,m+1} = \begin{bmatrix} \frac{n_m+n_{m+1}}{2n_m} \exp[ikz_{m,m+1}(n_{m+1}-n_m)] & \frac{n_m-n_{m+1}}{2n_m} \exp[-ikz_{m,m+1}(n_{m+1}+n_m)] \\ \\ \frac{n_m-n_{m+1}}{2n_m} \exp[ikz_{m,m+1}(n_{m+1}+n_m)] & \frac{n_m+n_{m+1}}{2n_m} \exp[-ikz_{m,m+1}(n_{m+1}-n_m)] \end{bmatrix}$$

Equation (3.6) is applied for all interfaces, leading to:

$$\begin{bmatrix} E_1 \\ \\ E'_1 \end{bmatrix} = M_{1,2}M_{2,3}...M_{N-1,N} \begin{bmatrix} E_N \\ \\ E'_N \end{bmatrix} = M \begin{bmatrix} E_N \\ \\ 0 \end{bmatrix} \tag{3.7}$$

where

$$M = \prod_{m=1}^{N-1} M_{m,m+1} = \begin{bmatrix} m_{11} & m_{12} \\ \\ m_{21} & m_{22} \end{bmatrix}$$

The reflection R and transmission T are expressed as follow:

$$R = \left| \frac{E'_1}{E_1} \right| = \left| \frac{m_{21}}{m_{11}} \right|^2, \tag{3.8}$$

$$T = \left| \frac{E_N}{E_1} \right|^2 = \left| \frac{1}{m_{11}} \right|^2, \tag{3.9}$$

which suggest the strong dependence of the reflectance and transmitance spectra on the number of layers. In order to model the optical responses of the multiple-quantum-well or multilayer structures, the thickness of the samples needs to be known.

3.1.4 From Reflection to Absorption: Kramer-Kronig Analysis

The Lorentz model discussed in Section 3.1.3 reveals the correlation between the real (n) and imaginary (κ) parts of the complex refractive index ($\widetilde{n}$). By complex number

analysis, n and κ can be calculated from the other via Kramers-Kronig relationship as [3]:

$$n(E) = 1 + \frac{2}{\pi}\mathrm{P}\int_0^\infty \frac{E'\kappa(E')}{E'^2 - E^2}dE', \tag{3.10}$$

$$\kappa(E) = -\frac{2}{\pi E}\mathrm{P}\int_0^\infty \frac{E'^2[n(E') - 1]}{E'^2 - E^2}dE', \tag{3.11}$$

where P denotes the principle value of the integral. Since both reflection and absorption coefficients are derived from the complex refractive index, $R(E)$ and $\alpha(E)$ are also correlated. It commonly happens in practice that only either absorption (thin films, nanostructures) or reflection (bulk crystal) can be measured. Therefore, by measuring one quantity, Eqs. (3.10) and (3.11) allow us to derive the other.

3.1.5 Photoluminescence Spectra

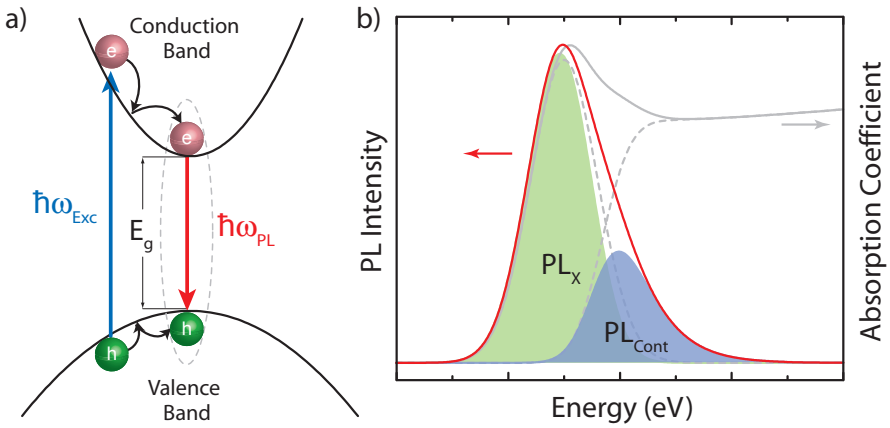

Figure 3.3: Photoluminescence process in semiconductors. (a) Schematic of the photoluminesce process. An incident photon with $\hbar\omega_{\mathrm{Exc}} \geq E_g$ is absorbed, creating an electron in the conduction band and a hole in the valence band. These photo-excited carriers quickly relax to the corresponding bandedges and radiatively recombine, emitting a photon $\hbar\omega_{\mathrm{PL}}$ (b) Photoluminescence spectrum (red solid line) calculated from the absorption spectrum (gray solid line) and thermal population of the photo-excited carriers described by Fermi-Dirac function. The total PL is decomposed into the exciton $\mathrm{PL_X}$ (green shaded area) and continuum $\mathrm{PL_{cont}}$ (blue shaded area) parts.

The photoluminescence process is more complicated than the reflectivity and absorption. The emission of a photon requires the absorption of a high-energy photon followed by relaxation processes, if there is an excess of energy. Figure 3.3(a) shows a simplified picture of how light is emitted in a semiconductor. A valence electron initially at the valence band absorbs a photon energy $\hbar\omega_{\mathrm{Exc}} \geq E_g$ and is excited to the conduction band,

leaving a hole in the valence band. The energetic carriers then quickly relax to the corresponding band extrema by emitting phonons. Depending on the strength of Coulomb interactions, the electrons and holes can couple to form an exciton if $E_b \geq k_B T$, and later radiatively recombine to emit a photon $\hbar\omega_{\mathrm{PL}}$, or can instantaneously emit a photon from the bandedges if $E_b < k_B T$.

The lineshape of the photoluminescence spectrum is affected by the thermal distribution of the carriers in different bands and the overlap of the carrier wavefunctions. Thermal population of the photo-excited carriers at the energy E is described by Fermi-Dirac distribution: $f(E,T) = (1+C\exp(E/k_B T))^{-1}$, where C is a constant. Whereas, the wavefunction overlap is proportional to the oscillator strength of the transition, which is reflected in the absorption spectrum. The product of these two components results in the PL spectrum as shown in Fig. 3.3(b). In the presence of multiple bands, the carrier/exciton relaxation processes need to be taken into account to model the PL lineshape.

3.2 Time-Resolved Photoluminescence and Absorption Spectroscopy

Besides the use of steady-state spectroscopy to understand the electronic band structures, the questions of how the carrier population is built up at different bands and decays from the initial excitation, requires time-resolved techniques. By using pulsed lasers, the transient states of the systems can be resolved. The temporal resolution is limited by the electronic response of the detectors and the laser pulse width.

3.2.1 Time-Resolved Photoluminescence

Time-resolved photoluminescence spectroscopy records the intensity of light emission as a function of time after a short flash of laser excitation. In our experiments, the excitation was provided by a femtosecond pulsed laser operating at 800 nm whose frequency is doubled by a non-linear β-barium borate (BBO) crystal to provide 400 nm light. The experimental setup for the time-resolved PL is similar to that for the steady-state PL measurement as shown in Fig. 3.1. However, instead of the spectrometer and CCD/CMOS, a single-photon avalanche photodiode (APD) was used that is sensitive to single photon detection due to the large internal gain as well as the high signal-to-noise

ratio. The APD is connected to a time-correlated single photon counting (TCSPC) system. The temporal resolution of the APD is about 60 ps. Since the technique is based on single-photon counter, very low excitation fluences were used in order to avoid multiexciton formation and to ensure that for each laser-pulse, less than one exciton is promoted in the case of nanocrystals. The luminescence decay signal can be filtered by suitable cut-off filters.

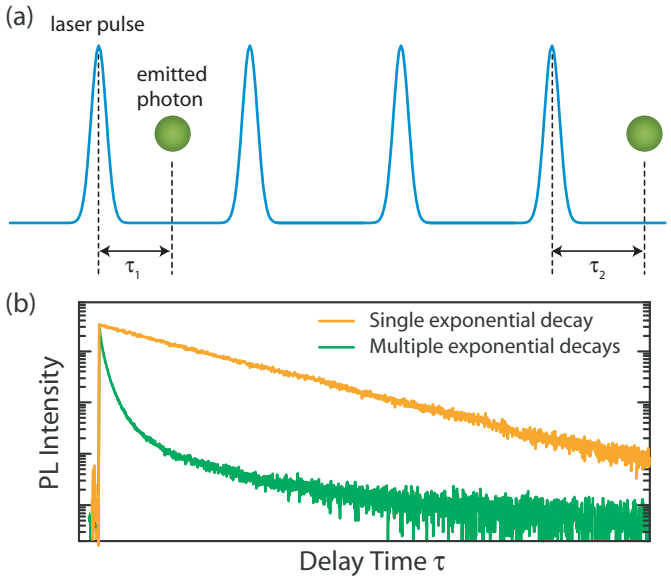

Figure 3.4: (a) Single-photon counting principle. The APD starts counting from 0 when the laser pulse reach the sample, and detects an emitted photon after a desired time τ_1. After few cycles, another photon emitted at a desired time τ_2 is detected. The repetition rate was controlled by a pulse-picker to ensure that only a single photon can be detected at a time. The counting process is repeated for different delay time τ_i over the acquisition time. (b) PL decay curves obtained by summing up the number of photons emitted at each τ_i. The PL decay trace can comprise a single (orange curve) or multiple (green curve) exponential decay channels.

Figure 3.4(a) describes the single-photon counting principle of the APD-TCSPC system used in our experiments. The excitation photons, generated from a laser pulse, arrive on the sample. An emitted photon at a delay time τ_1 after the excitation is collected by the APD. The sample is excited repetitively by many laser pulses, whose repetition rate is controlled by a pulse-picker to ensure that only a single photon can be detected at a time. If the single photon probability condition is met, no photon will be detected in the next few cycles. The detection is enabled again and another photon emitted at a desired time τ_2 is counted.

After the acquisition time, the number of photons emitted at each delay time τ_i will be summed up to obtain the PL decay curves as shown in Fig. 3.4(b) as an example. The

time-resolved PL profile reflects the decay of the carrier population over time, including the radiative and non-radiative recombination processes as $\tau_{\mathrm{PL}}^{-1} = \tau_{\mathrm{R}}^{-1} + \tau_{\mathrm{NR}}^{-1}$. Depending on the energy spectrum of each particular system, the decay curve can comprise single (orange curve) or multiple (green curve) exponential decay channels. In the simplest case of the sample with single excited state and 100% quantum yield, the only decay time is identical with the radiative PL lifetime. However, in most of the practical cases, multiple time constants can be extracted from the PL decay that correspond to different dynamic processes.

3.2.2 Transient Absorption Spectroscopy

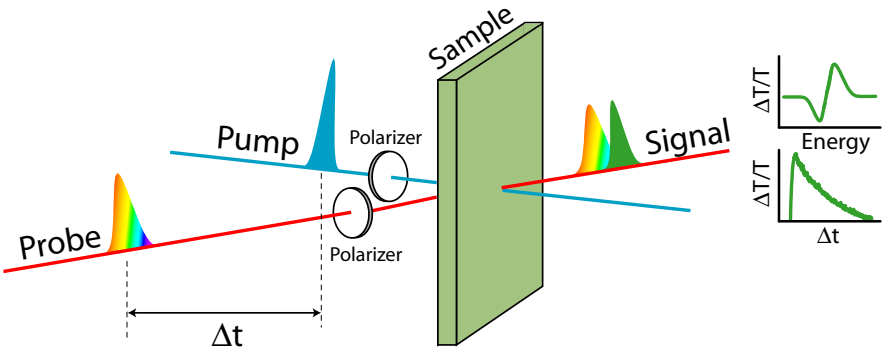

Figure 3.5: Pump-probe geometry for transient absorption spectroscopy. The pump pulse excites carriers in the sample, while the broadband probe pulse arrives after a controlled delay time Δt, to measure the pump-induced changes in the transmission, $\Delta T/T$ (or absorption) after the pump excitation. The signal $\Delta T/T$ is mapped out as a function of energy and delay time.

Transient absorption spectroscopy, also known as pump-probe technique, is a method to track the evolution of the absorption spectrum of a system after being excited. The pump-probe geometry is illustrated in Fig. 3.5. In our experiments, a pulsed laser is divided into two beams (1) to provide *pump* pulses via an optical parametric amplifier and (2) to generate broadband *probe* pulses after focusing on a CaF_2 or sapphire window. A pump pulse excites carriers in the sample, while a probe pulse, arrives after different controlled delay time Δt. The signal is recorded by a CMOS detector, and the pump-induced changes in the absorption spectrum are computed as a function of energy and Δt. Polarizers can be installed along the pump and probe optical paths for polarization-resolved measurements.

The pump beam after the amplifier has the repetition rate of 1 kHz. Before reaching the sample, the excitation beam is directed through a mechanical chopper, which is syn-

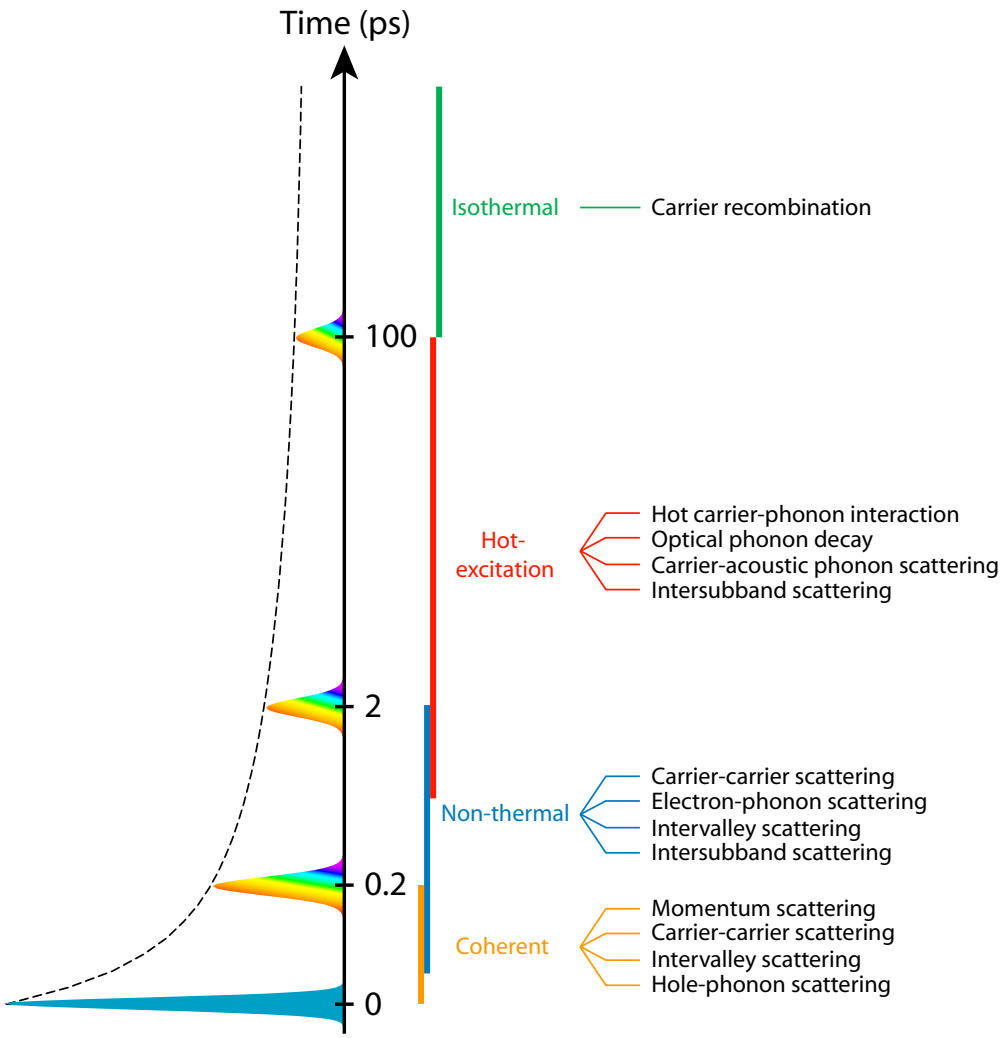

Figure 3.6: Carrier relaxation regimes in semiconductors at different time after the photo-excitation at time zero. The photo-induced **coherence** of the intrinsic states is typically destructed within the first ∼200 fs. After that, the carriers are scattered to the real band-dispersion, while the distribution among the states cannot be described by a temperature. The **non-thermal** population lasts for ∼2 ps, before scattering processes drive the system to the **hot-excitation** regime (∼1-100 ps). The carriers thermalize then recombine after >100 ps in an **isothermal** regime.

chronized to the amplifier, in such a way that the pump pulses are alternatively allowed or blocked to pass. Thus, the sample is alternatively excited ('pump-on') or non-excited ('pump-off'), and the transmission spectrum are accordingly recorded for each of the cases. The differential transmission ($\Delta T/T$) is calculated by the relative difference between the transmitted probe spectra when pump-on and pump-off with respect to the transmission when pump-off, *i.e.*, $\Delta T/T = (T_{\mathrm{pump-on}} - T_{\mathrm{pump-off}})/T_{\mathrm{pump-off}}$. The evolution of the transmission spectra is resulted from the changes in the transient population of the photo-excited carriers. In semiconductors, before reaching thermodynamic equilibrium states, the photo-excited carriers undergo different relaxation processes,

which can be categorized into four main regimes: coherent, non-thermal, hot-carrier and isothermal regimes [4], as summarized in Fig. 3.6.

In brief, the ultrashort laser pulse excites carriers from ground states to excited states. The excitation harnesses a well-defined phase at early time that is called as **coherent** regime. The photo-induced coherence decays via scattering events and is typically destructed within $\sim$200 fs after the laser excitation. As a result, the carriers acquire momentum to scatter from the light-cone to the real band-dispersion. At this stage, the carrier distribution over the states cannot be described by a temperature. This **non-thermal** regime typically dominates till $\sim$2 ps, before the scattering processes drive the system to **hot-excitation** regime, where the carrier population is well characterized by a temperature. From high-energy states, the hot carriers release excessive energy to reach the bandedges within $\sim$1-100 ps, and eventually return to the ground states via radiative or non-radiative recombination. The last **isothermal** regime occurs beyond $\sim$100 ps.

References

1. Elliott, R. J. Intensity of optical absorption by excitons. *Phys. Rev.* **108,** 1384 (1957).
2. Grilli, E., Guzzi, M., Zamboni, R. & Pavesi, L. High-precision determination of the temperature dependence of the fundamental energy gap in gallium arsenide. *Phys. Rev. B* **45,** 1638 (1992).
3. Fox, M. *Optical properties of solids* (Oxford University Press, 2010).
4. Shah, J. *Ultrafast spectroscopy of semiconductors and semiconductor nanostructures* (Springer Science & Business Media, 2013).

Chapter 4

Excitonic Properties in Lead Halide Perovskite Bulk Crystals

A number of theoretical and experimental studies have been conducted on lead halide perovskites (LHPs) raising many interesting questions, since the observations seem to contradict each other. Particularly, the dominant process governing the optical responses of lead halide perovskites at room temperature remains controversial between free-carriers and excitons [1–9]. Despite of different measurements, including magneto-absorption, temperature-dependent and optical absorption, exciton binding energies are reported over a wide range: 2-55 meV for $CH_3NH_3PbI_3$ [1, 2], 15-100 meV for $CH_3NH_3PbBr_3$ [3–9] and 50 meV for $CH_3NH_3PbCl_3$ [9]. Knowledge of the binding energy between electrons and holes is critically important for device design and operation and for unravelling the photophysics of the materials. Therefore, optical studies on high-quality crystals are important to clarify the photophysics and energy structures of lead halide perovskites. This chapter will present a systematic investigation on the intrinsic optical properties of high-quality lead halide perovskite bulk crystals using temperature-dependent reflectance and photoluminescence (PL) spectroscopy techniques. The studied compositions include the hybrid organic-inorganic $CH_3NH_3PbBr_3$, $CH_3NH_3PbI_3$ and all-inorganic $CsPbBr_3$ perovskites.

4.1 Multiple Exciton Transitions

4.1.1 Optical Characterizations of $CH_3NH_3PbBr_3$

Figure 4.1 shows the typical low-temperature (T = 10 K) reflectance (top black curve) and PL (bottom green curve) spectra measured on the preprared $CH_3NH_3PbBr_3$ crystal. Single crystals greatly reduce grain boundaries as well as trap states, which usually appear on polycrystalline thin films [10, 11]. Indeed, evidenced in this work, no trap

states have been detected in the optical spectra.

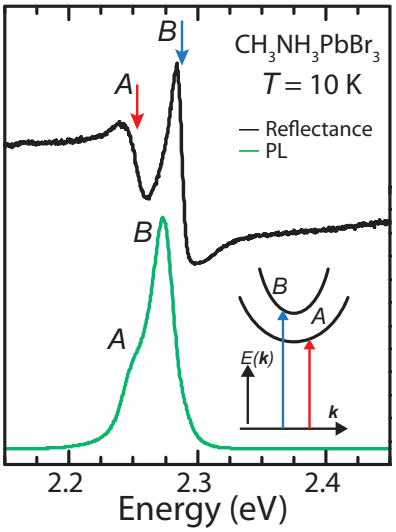

Figure 4.1: Reflectance and photoluminescence spectra taken at low-temperature (T = 10 K) on high-quality $CH_3NH_3PbBr_3$ single crystal. Resonances A ($\sim$2.244 eV) and B ($\sim$2.280 eV) are clearly resolved in both reflectance (top black curve) and PL (bottom green curve) spectra. Inset: schematic energy diagram for direct optical transitions associated with intrinsic free-excitons A and B given by red and blue arrows, respectively.

Two sharp spectral resonances labelled as A and B at energy positions $\sim$2.244 eV and $\sim$2.280 eV, respectively, are clearly resolved in the reflectance spectrum corresponding to intrinsic free-exciton transitions. Their derivative-like lineshapes resemble direct excitonic features observed in the reflectance spectra of other direct-bandgap semiconductors such as bulk GaAs [12] and ZnO [13], CdS thin films [14] and MoS_2 monolayers [15]. In such systems, an exciton is formed by an electron and a hole at the same $\boldsymbol{k}$-point; therefore, it has zero wavevector (*i.e.* $\boldsymbol{k_X} = \boldsymbol{k_e} - \boldsymbol{k_h} = \mathbf{0}$) [16]. A schematic energy diagram in exciton representation is shown in the inset of Fig. 4.1, where red and blue arrows denote free-exciton transitions A and B, respectively.

The PL spectrum exhibits two discernible contributions. A high-energy structure at $\sim$2.270 eV originates from radiative recombination of free-exciton B (X_B). At the low-energy side of X_B, a shoulder at approximately the same energy as spectral resonance A in the reflectance spectrum can be distinguished, arising from radiative recombination of low-energy exciton A (X_A). The good energy matching between the reflectance features and the emission peaks confirms the high quality of the investigated $CH_3NH_3PbBr_3$ single crystal. Noticeably, the high-energy X_B has larger contribution to the total PL intensity than the lowest-energy X_A. The intensity distribution will be discussed further in Section 4.2.2.

4.1.2 Temperature-dependent Reflectance and Photoluminescence Spectra

To unravel the nature of the excitonic transitions, we monitored the changes on the reflectance and PL spectra upon temperature variations. Figure 4.2(a) and (b) respectively show the reflectance and normalized PL spectra (blue solid lines) at selected temperatures from T = 10 K (bottom) to T = 280 K (top). All the spectra are vertically shifted for clarity. The $CH_3NH_3PbBr_3$ crystal undergoes a structural transition at T = 150 K, which is spectroscopically revealed in Fig. 4.2(a) and (b) as a sudden change of the corresponding spectra. The phase-transition temperature agrees very well in both reflectance and PL experiments and also with previous reports in $CH_3NH_3PbBr_3$ compound [4–6].

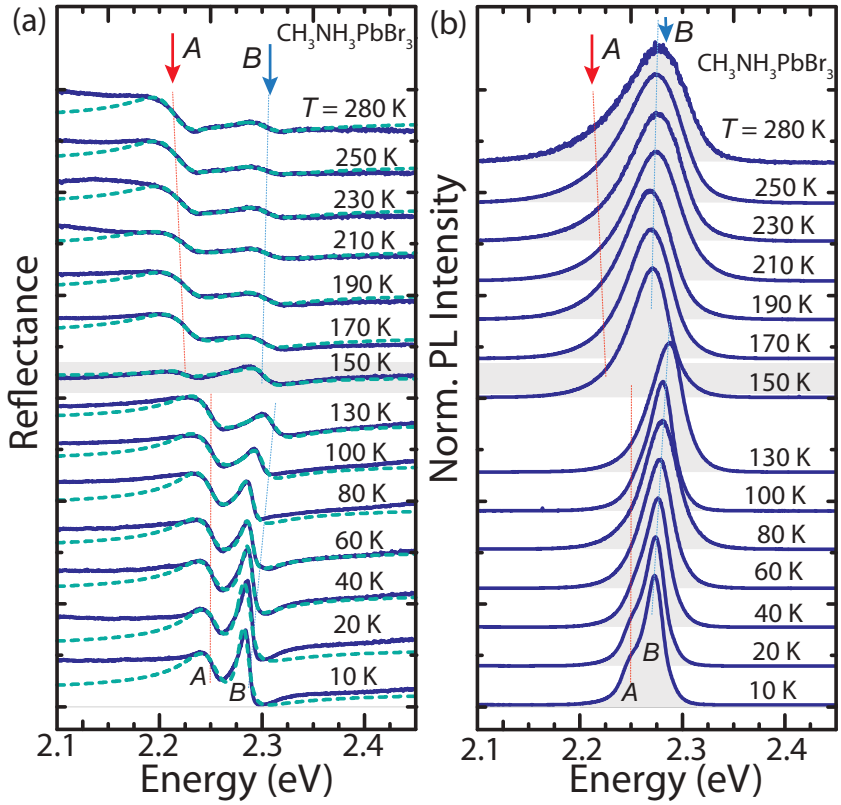

Figure 4.2: (a) Reflectance spectra (blue solid lines) at selected temperature from 10 K (bottom) to 280 K (top). The green dashed lines are fitting curves using two Lorentz oscillators. The red and blue dotted lines are guidelines. The phase transition occurring at 150 K is highlighted. The spectra are vertically shifted for clarity. (b) Same as (a) for PL spectra.

The behaviour on temperature can be classified according to structural phases: orthorhombic (T < 150 K) and tetragonal-cubic (T > 150 K) phases. For simplicity, low-temperature phase stands for orthorhombic phase, whereas above 150 K, we will

refer to as high-temperature phase, and no distinction will be done between cubic and tetragonal crystal structures. First, we describe the reflectance spectra (see Fig. 4.2(a)). When increasing temperature from 10 K to 130 K (low-temperature phase), the spectral position of high-energy exciton B shifts to higher energies (blue shift), its amplitude monotonically decreases and its resonance linewidth increases. On the other hand, low-energy exciton A hardly changes with temperature, whose energy position, amplitude and linewidth are roughly constant. At the phase-transition temperature (T = 150 K), the whole spectrum shifts to lower energies (red shift) and the reflectance amplitude of X_A suddenly drops, while that of X_B remains unperturbed by the phase change.

At the high-temperature phase, X_A recovers and exhibits a pronounced red-shift with increasing temperature, while its amplitude and linewidth are more likely constants. On the other hand, the exciton transition X_B does not show significant energy changes, while its amplitude decreases and its linewidth increases with increasing temperature. It is worth noting that X_B is gradually smeared out and becomes hardly visible at elevated temperatures ($T \geq$ 230 K); in contrast, X_A is still pronounced up to 280 K, indicating a large difference between binding energies (E_b) of excitons A and B. For the high-energy X_B, $E_{b,B}$ is smaller than or comparable to the thermal energy k_BT at 230 K, where k_B is the Boltzmann constant ($k_BT \sim$ 20 meV), whereas for low-energy exciton A, $E_{b,A}$ is much larger than k_BT at 280 K. In addition to the distinct binding energies, opposite energy shifts of the optical transitions with temperature also suggest different nature of free-excitons A and B.

Figure 4.2(b) depicts the normalized PL spectra (blue solid lines) at the same temperatures as shown in Fig. 4.2(a). Overall, the energy structure of the PL agrees well with the reflectance at all temperatures. First, contributions from exciton levels A and B can be distinguished until $T \leq$ 40 K. The temperature rise causes a blue-shifted energy and a broader linewidth of X_B that obscures the contribution from X_A. Consequently, low-energy feature X_A is no longer visible at above $T \sim$ 40 K. This trend remains until 130 K, just below the phase transition. The dominant contribution of the high-energy exciton B to the total PL intensity is non-trivial and will be left for discussion.

At the high-temperature phase, the PL spectral position does not show significant variations, which is consistent with the almost unaffected reflectance in this temperature range (see Fig. 4.2(a)). Although most of the emitted light arises from radiative recombination of free-exciton B, the lineshape remains asymmetric at the low-energy side of the PL spectrum that originates from free-exciton A. This asymmetry increases

with increasing temperature and is particularly prominent at $T \geq 200$ K. Moreover, the integrated PL intensity is studied as a function of excitation power at all temperatures as shown in Fig. 4.3. The power dependence is fitted by the equation of power law: $I = \alpha P^{\beta}$, where α is the PL intensity acquired with a power unit and β indicates the number of photons involved in the process. The power analysis results in superlinear power dependence ($\beta > 1$) at all temperatures that suggests the existence of more than a single recombination process. Indeed, in the case of a single emissive channel, a linear power dependence, *i.e.,* β = 1 is expected, whereas a sublinear behaviour is typical for nanocrystals or bound states.

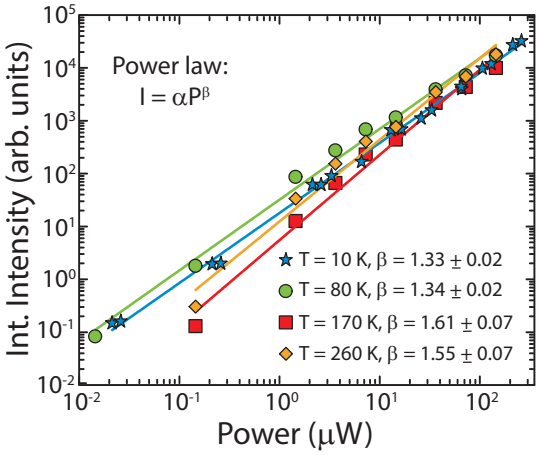

Figure 4.3: Power dependence of the integrated PL intensity in a log-log scale at different temperatures, including low- and high-temperature structural phases of $CH_3NH_3PbBr_3$. The dashed lines are power laws fitted to the data. The non-linear dependence ($\beta > 1$) at all temperatures suggests more than a single recombination channel in the PL of $CH_3NH_3PbBr_3$.

4.1.3 Resonant Energies

The experimental reflectance curves are fitted using the usual Fresnel expression for a semi-infinite medium as adapted from Eq. (3.2) and (3.3) for two classes of oscillators $j = A, B$, resulting in the fitting curves shown by green dashed lines in Fig. 4.2(a). In the region of exciton features A and B, excellent agreement is observed between the experimental reflectance and fitting curves at all temperatures. The extracted energies of X_A and X_B are plotted as a function of temperature in Fig. 4.4(a). The abrupt change due to the orthorhombic-tetragonal phase transition is highlighted at 150 K. Exciton B located at ~2.280 eV (at ~2.300 eV after 150 K) shows a blue-shift with increasing temperature, which is opposite to the red-shift of free-excitons in conventional semiconductors such

as GaAs [17], InP [18] and ZnS [19]. The unconventional shift of the optical resonance to high-energies has been previously reported in Pb-based compounds [20] and is a common characteristic of lead halide perovskites [1, 4, 6, 21]. It has been attributed to the reduced overlap of the s-p (p-p) antibonding in the valence (conduction) band. As a result, both valence and conduction bands are energetically lowered, while the valence band exhibits a larger decrease in energy, leading to the blueshift of X_B with increasing temperature [22–24].

On the other hand, the optical transition X_A occurs at lower energy of $\sim$2.244 eV (at $\sim$2.220 eV after 150 K) and exhibits a *traditional* red-shift with increasing temperature. The trend is more clearly seen after 150 K. The opposite energy responses of X_A and X_B to temperature evidence for different origins of free-excitons A and B.

4.1.4 Exciton Binding Energies

By applying Lorentz model on the reflectance spectra (see Fig. 4.2(a)), the oscillator strengths of both excitonic transitions are found to be constant over the whole temperature range, except for the discontinuity at phase transition ($T \sim 150$ K) (see Fig. 4.5).

On the other hand, the amplitude of X_B decay exponentially as shown in Fig. 4.4(b) that can be well reproduced by an Arrhenius-like equation given by $A_R(T)$ = $A_{0,R}$(1 + $C\exp(-E_a/k_BT)$)$^{-1}$ (cyan solid line). This function typically describes a dissociation process with activation energy E_a. In our case, it is equal to the exciton binding energy. Since the reflectance amplitude does not show any discontinuity even at the phase transition, the binding energy of X_B should be the same for all structural phases. Similar suggestions have been made recently [4]. From the fitting, the binding energy of X_B is estimated to be $E_{b,B}$ = 21 $\pm$ 3 meV, which is consistent with the experimental reflectance where exciton B becomes weak after $\sim$230 K (see Fig. 4.2(a)). Remarkably, the binding energy agrees well with recent works on $CH_3NH_3PbBr_3$ perovskite [6, 7, 9].

In the hydrogen model for Wannier-Mott excitons, binding energy and Bohr radius are expressed as E_b = $(\mu/m_0)(R_H/\varepsilon_r^{*2})$ and a = $(m_0/\mu)\varepsilon_r^* a_H$, respectively, where R_H = 13.6 eV is the Rydberg energy and a_H = 0.053 nm is the Bohr radius of the hydrogen atom. We use the effective mass as previously addressed as μ_B = 0.13m_0 [3, 7]. Hence, the effective dielectric constant is estimated to be ε_r^* = 9.18 $\pm$ 0.66. The Bohr radius is, therefore, a_B = 3.74 $\pm$ 0.27 nm. Both ε_r^* and a_B values are in good agreement with previous literature reports [6, 7].

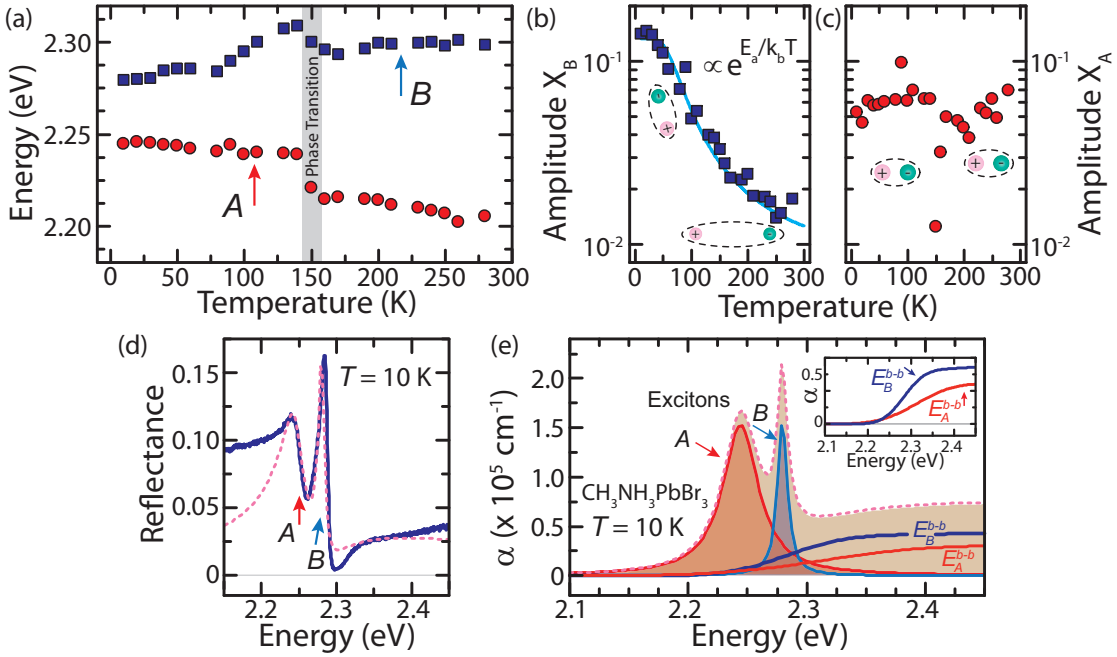

Figure 4.4: (a) Resonance energies of free-exciton A (red circles) and B (blue squares) versus temperature as extracted from Lorentz model in Fig. 4.2(a). Error bars are comparable to the symbols sizes. (b) Reflectance amplitude of X_B (blue squares) as a function of temperature along with the fitting curve (cyan solid line) by an Arrhenius-like equation (see text). The cartoon illustrates a free-exciton, where the distance (black dashed line) between electron (green circle) and hole (pink circle) displays the coupling strength of the exciton at low- (tightly bound electron-hole pair) and high- (weakly bound electron-hole pair) temperature ranges. (c) Reflectance amplitude of X_A versus temperature with the same representation for excitons. The electron-hole pair is tightly bound at all temperatures, except at the phase-transition temperature T = 150 K. (d) Experimental reflectance at 10 K (blue solid line) along with the fitting curve (pink dotted line) derived from the combination of Elliot theory and Kramers-Kronig relationship (see text). (e) Total absorption coefficient as extracted from the model in (d) is shown by the pink dotted line. Different contributions includes: excitonic bands X_A and X_B (shaded area under the red and blue Lorentzian-shaped solid line, respectively), the corresponding continuum bands $E_A^{\mathrm{b-b}}$ and $E_B^{\mathrm{b-b}}$ (areas under dark-orange and dark-blue solid lines, respectively.

Figure 4.4(c) shows the reflectance amplitude of exciton A. It does not change significantly with temperature, except for the phase transition, indicating that the binding energy $E_{b,A}$ is much larger than k_BT at room temperature. In this case, the reflectance amplitude of the excitonic feature cannot be used to determine its binding energy. In order to overcome this issue, Fig. 4.4(d) shows the experimental reflectance (blue solid line) at T = 10 K along with the model combining Elliot theory and Kramers-Kronig relationship. Elliot theory, which is normally used to explain the absorption of direct

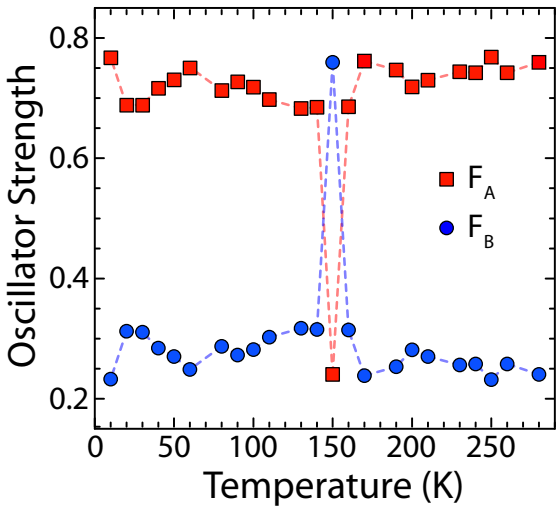

Figure 4.5: Oscillator strength of excitons A (red squares) and B (blue circles) as a function of temperature obtained by the dipole oscillator model (Lorentz model).

band-gap semiconductors, is converted to reflectance via Kramers-Kronig transformation (see Section 3.1.2). In this particular case, amplitudes of both excitons and the associated continuum bands are parameterized. The binding energy of X_A is variable, while that of X_B is set to 21 meV as calculated above. The exciton energies and linewidths are also fixed according to the aforementioned Lorentz model fitting in Fig. 4.2(a). The band-to-band transition (or continuum) energies are accordingly set as E_j^{b-b} = $E_{b,j}$ + $E_{0,j}$ (j = A, B). The calculated curve, given by the pink dotted line, shows good agreement with the experimental reflectance, especially the excitonic features and the continuum bandedge regions are well reproduced. The spectral band beyond ∼2.4 eV does not follow, since higher energy bands are not included. By this computational method, the lower and upper bound of the binding energy of X_A are determined, giving $E_{b,A}$ = 90 ± 30 meV (see Fig. 4.6).

The giant binding energy results in a large exciton mass evaluated as m_A^* = (0.56 ± 0.27)m_0 and a small exciton Bohr radius calculated as a_A = 0.87 ± 0.48 nm. These values are comparable to the large free-exciton binding energies and effective masses in oxide semiconductors such as CuO_2 [25, 26] and ZnO [27–29]. The large $E_{b,A}$ makes free-exciton A stable at room temperature and explains why it persists in the reflectance spectra up to 280 K (see Fig. 4.2(a)).

In the absorption spectrum (see Fig. 4.4(e)), free-exciton features A and B are reproduced at energies of ∼2.244 eV and ∼2.280 eV. They are represented by shaded areas under red and blue Lorentzian-shaped solid lines, respectively. The corresponding energies for band-to-band transitions are found at $E_B^{\mathrm{b-b}} \sim 2.301$ eV and $E_A^{\mathrm{b-b}} \sim 2.334$

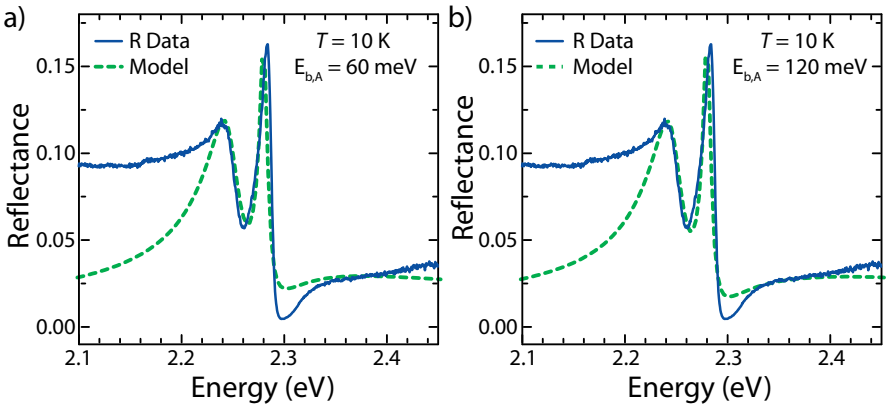

Figure 4.6: Experimental reflectance spectrum at 10 K (blue dots) along with the fitting by the combination of Elliot theory and Kramers-Kronig relationship using (a) $E_{b,A}$ = 60 meV and (b) $E_{b,A}$ = 120 meV. The modelled curves reasonably follow the experimental data, with the best fitting obtained with $E_{b,A}$ = 90 meV.

eV. Intriguingly, although X_A has lower energy than X_B, the band-to-band edge A lies slightly above the band-to-band edge B by ∼33 meV owing to large $E_{b,A}$. Since the binding energies of both excitons are not affected by structural phases, the energy shifts with temperature of the continuum bands should follow those of excitons A and B. With increasing temperature from 10 K, it is expected that $E_B^{\mathrm{b-b}}$ approaches $E_A^{\mathrm{b-b}}$ to get close at approximately 140 K, just below the phase transition. At the high-temperature phase, $E_A^{\mathrm{b-b}}$ red-shifts further from $E_B^{\mathrm{b-b}}$. The intricate energy landscape with non-trivial temperature dependence, including level crossing, may lead to a complicated optical response such as relaxation and recombination of photo-excited electron-hole pairs.

4.1.5 Optical Transitions in Other Perovskites

In order to unravel the role of the chemical components in the electronic band structures of lead halide perovskite materials, the cation and anion were alternatively changed while the other parts were kept intact. Particularly, as compared to $CH_3NH_3PbBr_3$ discussed in Section 4.1.1-4.1.4, the anion Br^- was changed to I^- in the hybrid organic-inorganic $CH_3NH_3PbI_3$, and the cation $CH_3NH_3^+$ was changed to Cs^+ in the all-inorganic $CsPbBr_3$. We have conducted similar reflectance and photoluminesce experiments as a function of temperature on different lead halide perovskite crystals made of $CH_3NH_3PbI_3$ and $CsPbBr_3$.

Figure 4.7(a) depicts the reflectance (gray solid line) and photoluminescence spectra (blue solid line) taken at T = 10 K for $CH_3NH_3PbI_3$ bulk crystals. In the reflectance measurement, three exciton resonances labelled as A, B and C are clearly resolved at

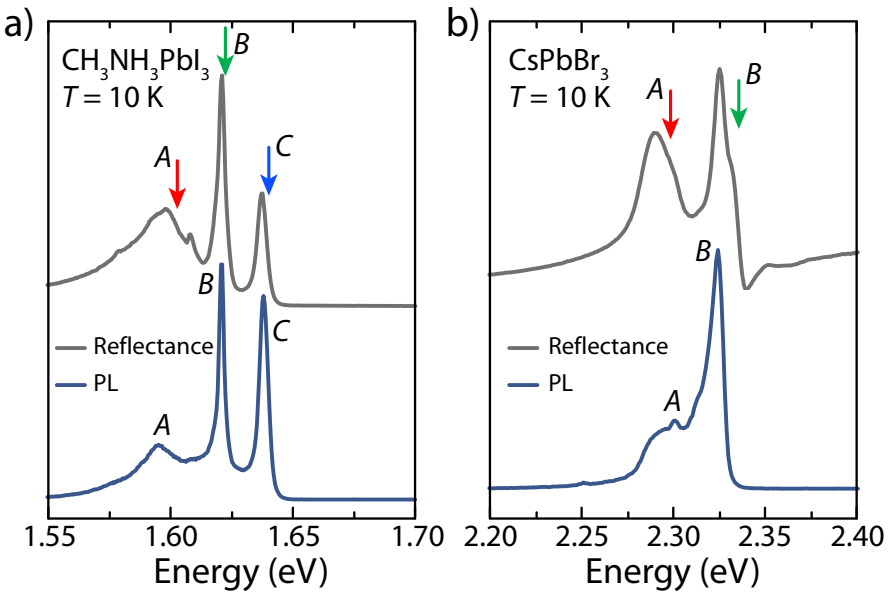

Figure 4.7: (a) Reflectance and photoluminescence spectra of the $CH_3NH_3PbI_3$ crystal taken at T = 10 K. Three resonances labeled as A, B, C located at ∼1.602 eV, ∼1.620 eV and ∼1.637 eV, respectively, are clearly resolved in both reflectance (top gray curve) and PL (bottom blue curve) spectra. (b) Reflectance and photoluminescence spectra of the $CsPbBr_3$ crystal taken at T = 10 K. Two resonances located at ∼2.292 eV and ∼2.323 eV are resolved in both reflectance (top gray curve) and PL (bottom blue curve) spectra.

∼1.602 eV, ∼1.620 eV and ∼1.637 eV, respectively. The PL spectrum consists of three features located at ∼1.595 eV, ∼1.621 eV and ∼1.638 eV. The excellent agreement between the spectral positions of the reflectance and PL spectra proves that three resonances are intrinsic optical transitions of $CH_3NH_3PbI_3$. On the other hand, the optical spectra of $CsPbBr_3$ reveal two main transitions labelled as A and B in Fig. 4.7(b). In the reflectance spectrum (gray solid line), the energies of X_A and X_B are ∼2.292 eV and ∼2.323 eV, respectively. In addition, on the high-energy shoulder of X_B, we observe another resonance at ∼2.331 eV, which may potentially arise from the localized effects. Besides the pronounced oscillator strength, the exciton nature of the resonances A and B is further confirmed by two emission features at ∼2.292 eV and ∼2.323 eV in the PL spectrum (blue solid line). In both compounds, the lowest-energy exciton X_A has lowest contribution to the total PL emission that is similar to the observation in $CH_3NH_3PbBr_3$ (see Fig. 4.1).

The behaviour of the excitons are monitored by varying the temperature from T = 10 K to 300 K. Figure 4.8(a) shows the reflectance spectra (gray solid lines) measured on $CH_3NH_3PbI_3$ at selected temperature. All the spectra are vertically shifted for clarity. Three resonances are clearly resolved at below 30 K. As increasing temperature, the

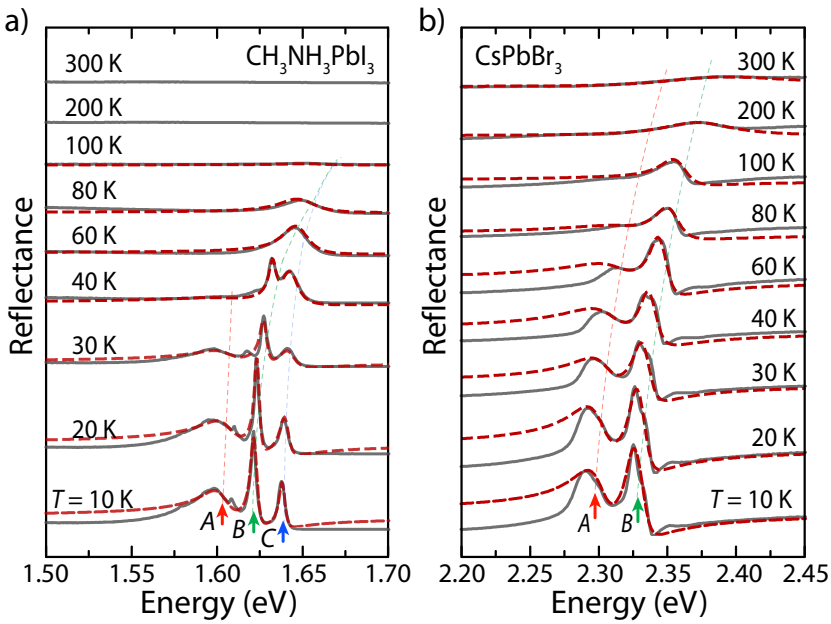

Figure 4.8: Reflectance spectrum taken at selected temperatures from T = 10 K to 300 K for (a) $CH_3NH_3PbI_3$ and (b) $CsPbBr_3$ crystals. As increasing temperature, all transitions exhibit blueshift. The red, green and blue dashed lines are guidelines. The spectra are vertically shifted for clarity. The dark-red dashed lines are fitting curves optimized for three and two Lorentz oscillators for $CH_3NH_3PbI_3$ in (a) and for $CsPbBr_3$ in (b), respectively.

linewidths of the features get broader and the amplitudes decrease. The exciton X_A becomes very weak at 40 K and hardly resolved at higher temperatures. Similarly, X_B and X_C exhibit broader linewidths and weaker amplitudes as temperature increases. From ∼60 K, X_B and X_C gradually merge and become a single resonance at ∼100 K. No resonance is observed at ∼200 K and above. The rapid weakening of the exciton resonances in the reflectance spectra upon temperature variation suggests small binding energies that activate the exciton dissociation at high temperatures. In addition, the absence of exciton resonances from ∼200 K is also due to the phase transition of the $CH_3NH_3PbI_3$ crystal from orthorhombic to tetragonal structure at ∼160 K [30, 31]. Besides the temperature-induced changes in the lineshape, the resonance energies are also shifted. In particular, X_B and X_C exhibit blueshift with increasing temperature, whereas, the energy of X_A remains almost unshifted until the exciton dissociates. The temperature-dependent energies of X_B and X_C in $CH_3NH_3PbI_3$ are comparable to X_B in $CH_3NH_3PbBr_3$ (see Fig. 4.2), while the unshifted X_A exciton at low-temperature range is similar between these two hybrid organic-inorganic compounds.

The responses of the optical properties to temperature have been also investigated

on $CsPbBr_3$ (see Fig. 4.8(b)). The reflectance spectra (gray solid lines) are shown at selected temperature from 10 K (bottom) to 300 K (top). As increasing temperature, the spectral positions of both excitons X_A and X_B shift to the high-energy side, while the amplitudes decrease and the widths get broader. Resonance X_A is almost smeared out after 80 K, while X_B remains until T ~200 K. In the investigated temperature range, no phase transition is observed and the $CsPbBr_3$ crystal structure exists in orthohombic phase [32]. Comparing $CsPbBr_3$ with $CH_3NH_3PbBr_3$, the behaviours of the high-energy transition X_B on both crystals are analogous, while the low-energy transition X_A responses oppositely to temperature.

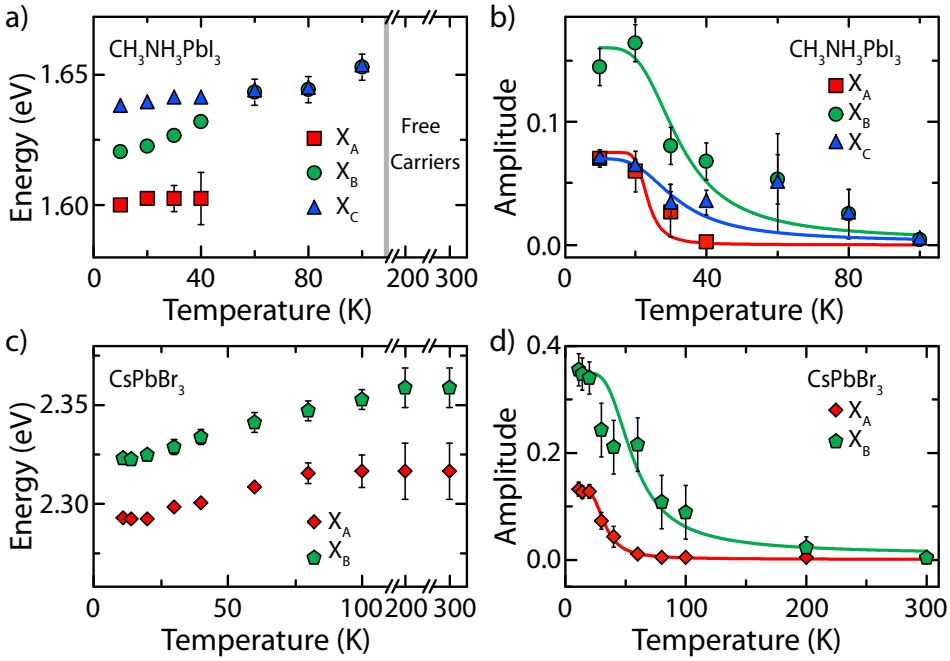

Figure 4.9: (a) Resonance energies of X_A (red squares), X_B (green circles) and X_C (blue triangles) of $CH_3NH_3PbI_3$ at different temperatures. X_A is not spectrally resolvable at above 40 K, while X_B and X_C persist until 100 K. At higher temperatures, most of the excitons dissociate into free carriers. (b) Reflectance amplitudes of the exciton components X_A (red squares), X_B (green circles) and X_C (blue triangles) in $CH_3NH_3PbI_3$ as a function of temperature. The individual amplitude is extracted from the Lorentz fitting. The amplitude decay follows Arrhenius function (colored solid lines), from which, exciton binding energies can be evaluated. (c) Energies and (d) reflectance amplitudes of X_A (red diamonds) and X_B (green pentagons) of $CsPbBr_3$ as a function of temperature. Similarly, the amplitudes are individually fitted by Arrhenius functions (color solid lines) to extract exciton binding energies.

The resonance energies extracted from the Lorentz fitting in Fig. 4.8(a) are shown in Fig. 4.9(a) for three excitons X_A, X_B and X_C of $CH_3NH_3PbI_3$ (colored symbols). Exciton X_A located at ~1.602 eV remains unshifted with temperature. On the other hand,

X_B and X_C shift to high-energy side with increasing temperature. The unconventional shift of the optical resonance to high energies has been previously reported in Pb-based compounds [20] and is a common characteristic of lead halide perovskites [2, 4, 6, 21]. The reflectance amplitude of each resonances is plotted as a function of temperature (see Fig. 4.9(b)). The temperature range is shown until 100 K, at which, the crystal exists in orthorhombic phase. The amplitude decays (colored symbols) are fitted by Arrhenius equations (red, green and blue lines), from which, the binding energies for X_A, X_B and X_C are determined as $E_{b,A} = 8 \pm 2$ meV, $E_{b,B} = 12 \pm 3$ meV and $E_{b,C} = 11 \pm 4$ meV, respectively. On the other hand, the energies of X_A and X_B of $CsPbBr_3$ (colored symbols) are shown in Fig. 4.9(c). With increasing temperature, both resonances exhibit blueshift while their amplitudes decays (see Fig. 4.9(d), colored symbols). The Arrhenius fitting (red and green lines) results in the binding energies of $E_{b,A} = 15 \pm 2$ meV for X_A and $E_{b,B} = 19 \pm 3$ meV for X_B. The value of $E_{b,B}$ in $CsPbBr_3$ is comparable to that in $CH_3NH_3PbBr_3$, while the binding energy of X_A in $CsPbBr_3$ is much smaller than that in $CH_3NH_3PbBr_3$.

In general, we find multiple exciton transitions dominating the optical spectra of all the investigated perovskite compounds. In each material, different excitons have distinct properties, including the temperature-induced energy shift and the exciton binding energy. Table 4.1 summarizes the exciton properties in orthohombic phase of the three lead halide perovskite compounds studied in this chapter.

4.2 Discussion

4.2.1 Origins of the Exciton Transitions

We discuss the potential origins of the exciton transitions within the free-carrier representation for pervoskites. Previous studies on $CH_3NH_3PbBr_3$ and $CsPbBr_3$ reported optical transitions behaving similarly to X_B [4–6, 34], whereas X_C has been discussed in $CH_3NH_3PbI_3$ [1]. In the orthorhombic phase, these excitons are widely accepted to originate from carriers at the Γ-point of the Brillouin zone [35–37]. Nevertheless, none of the current theoretical calculations have suggested the existence of the low-energy exciton X_A in perovskite materials. Relativistic Rashba effects have been considered, predicting the indirect nature of the fundamental band-gap of organo-lead halide perovskites [22, 38, 39]. Two spin-polarized bands are separated evenly from the original high-symmetry

Table 4.1: Exciton properties of different compounds in orthorhombic phase

	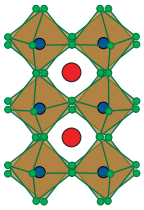	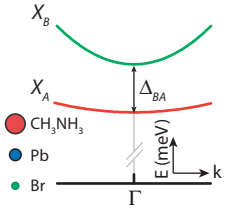	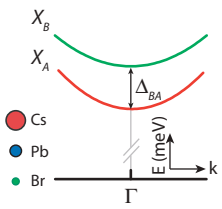
Energy splitting	Δ_{BA} = 20 meV Δ_{CA} = 37 meV	Δ_{BA} = 36 meV	Δ_{BA} = 31 meV
Reduced mass	$\mu_A = 0.08m_0$ $\mu_B = 0.11m_0$ $\mu_C = 0.10m_0$ ([7])	$\mu_A = 0.56m_0$ $\mu_B = 0.13m_0$	$\mu_A = 0.06m_0$ $\mu_B = 0.08m_0$ ([33])
Binding energy	$E_{b,A}$ = 8 meV $E_{b,B}$ = 12 meV $E_{b,C}$ = 11 meV	$E_{b,A}$ = 90 meV $E_{b,B}$ = 21 meV	$E_{b,A}$ = 15 meV $E_{b,B}$ = 19 meV

point in both conduction band (CB) and valence band (VB). The stronger splitting in $\boldsymbol{k}$-space expected at CB leads to momentum mismatch, which forbids direct transitions at the bandedges. In our observation, both X_A and X_B present clear signatures of direct transitions as revealed by pronounced oscillator strengths, large absorption coefficient and strong photoluminescence emission. Recently, giant Rashba spin-splitting has been experimentally evaluated on $CH_3NH_3PbBr_3$ single crystals, giving an energy increase of 160 meV of the VB maximum with respect to the original maximum at the Γ-point [40]. By noting the stronger Rashba effect at CB, the energy difference between the direct transition (at Γ-point) and the indirect transitions (at the spin-degenerated band edges) would be larger than 300 meV. However, the transition energies $E_A^{\mathrm{b-b}}$ and $E_B^{\mathrm{b-b}}$ differ by only ∼33 meV in the case of $CH_3NH_3PbBr_3$ for example, which is smaller by an order of magnitude. Therefore, the described picture about Rashba-induced indirect-direct transitions seems to be insufficient to explain the coexistence of excitons A, B and C.

We recall the different temperature responses of the exciton energies particularly in $CH_3NH_3PbBr_3$ (see Fig. 4.4(a)). Based on prior calculations, X_B is formed by carriers at Pb(s-orbital)-Br(p-orbital) antibonding and Pb(p-orbital)-Br(p-orbital) antibonding states in VB and CB, respectively [3, 37, 41, 42]. On the other hand, the energy-shift of X_A to temperature is opposite to X_B and the redshifted energy of X_A becomes clearer

after 150 K. We suggest that the bonds between organic cations ($CH_3NH_3^+$) and halide anions (Br^-) may induce additional energy levels, from which the optical transition with energy $E_A^{\mathrm{b-b}}$ arises.

This scenario agrees well with our observation on $CsPbBr_3$ and $CH_3NH_3PbI_3$ crystals, where multiple classes of excitons present. When the cation is replaced by Cs^+, the high-energy exciton (X_B) behaves similarly, while the behaviors of the low-energy exciton (X_A), such as temperature-induced shift and binding energy, changes significantly. Whereas, when we alter the halide anion by I^-, both high- and low-energy excitons are affected. Not only the number of optical transitions near the bandedges changes, but also the binding energies of the excitons are much lower. The precise origins of these excitons are not completely understood. A unified theoretical model, which can correlate our observations, spin-orbit coupling, Rashba effects and include the role of cations is needed to provide complete understanding on the complex band structures of the lead halide perovskite family.

4.2.2 Exciton Dynamics

The PL profiles of all the compounds exhibit similar intensity distribution of different emitting channels. The lowest-energy exciton contribute the least to the overall PL intensity, while it should hold most of the population at low temperature. We take $CH_3NH_3PbBr_3$ as a representative system to discuss the counter-intuitive intensity profile. The physical pictures are similar for $CsPbBr_3$ and $CH_3NH_3PbI_3$.

In Fig. 4.10(a), the experimental PL spectrum of $CH_3NH_3PbBr_3$ at 10 K (blue solid line) is fitted with two Lorentzians, in which, the spectral positions of the low-energy emission peak is fixed to the energy of X_A obtained from the reflectance fitting. As can be seen, the fitting (green dashed line) matches well with the experimental data and reveals a counter-intuitive behaviour: emission from high-energy exciton B (shaded blue area) has a much larger contribution than the lowest-energy exciton A (shaded red area) to the total PL intensity. Indeed, the intensity ratio is $I_B/I_A \sim 3.2$. This ratio increases with increasing temperature (see Fig. 4.2(b) and Fig. 4.11). At above 40 K, radiative recombination from excitonic band B dominates the light emission in $CH_3NH_3PbBr_3$. However, the asymmetric PL profile on the low-energy side reveals the weaker but non-zero contribution of X_A. This asymmetry is commonly observed in lead halide perovskites at room temperature [10, 43, 44] and is opposite to the normal

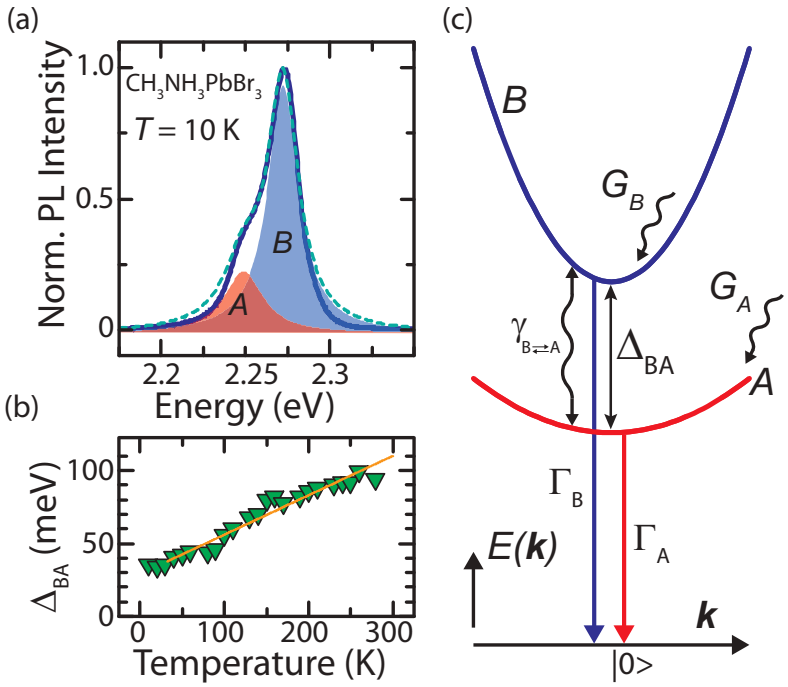

Figure 4.10: (a) PL spectrum at 10 K of $CH_3NH_3PbBr_3$ (blue solid line) along with the fitting curve (green dashed line) using values from the reflectance modelling. The Lorentzian contributions from X_A and X_B to the total PL are represented by shaded red and blue areas, respectively. The intensity ratio is I_B/I_A = 3.2. (b) Energy splitting Δ_{BA} between excitonic levels B and A (green triangles) as a function of temperature. The orange solid line is a phenomenological linear fitting. (c) Schematic representation of free-exciton bands A and B. The symbols are used in the kinetic three-level model.

intensity distribution in conventional semiconductors.

The PL intensity $I_j(E,T)$ resulted from excitonic recombination can be defined as $I_j(E,T) = N_j(E,T)\alpha_j(E,T)$ [18], where $N_j(E,T)$ and $\alpha_j(E,T)$ are population and absorption coefficient at the excitonic energy level X_j ($j = A, B$), respectively. The absorption coefficient is proportional to oscillator strength ($\alpha_j \propto F_j$) [45]. From the reflectance fitting, the oscillator strength of X_B is found to be ~3 times smaller than that of X_A (see Fig. 4.4(e) and Fig. 4.5). Thus, oscillator strengths are not the reason for the striking PL distribution. Therefore, the population term needs to be considered. In the case of non-interacting energy states, the thermal populations of photo-excited excitons on levels A and B depend on their energy splitting $\Delta_{BA}(T) = E_{0,B}(T) - E_{0,A}(T)$, whose temperature dependence is shown in Fig. 4.10(b). At 10 K, Δ_{BA} = 36 meV is much larger than thermal energy ($k_BT < 1$ meV), and this holds true at all temperatures. Such a large energy difference implies that the majority of excitons resides on the lowest-energy band A (see Fig. 4.10(c)). Therefore, in this scenario, contribution from high-energy level B to the total PL intensity should be negligible. Nevertheless, we observe the

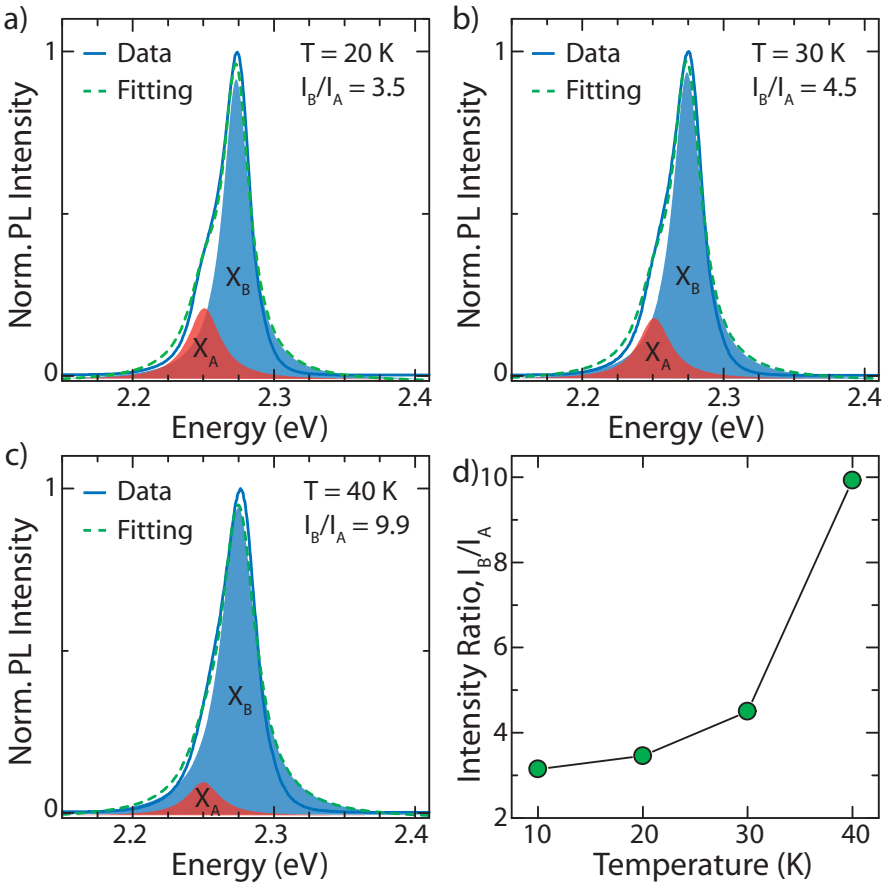

Figure 4.11: (a)-(c) Experimental PL spectra (blue solid lines) from 20 K to 40 K along with fitting curves (green dashed lines) using values from the reflectance modelling. The Lorentzian contributions from free-excitons A and B to the total PL are represented by the areas under red and blue Lorentzian-shaped curves, respectively. (d) Intensity ratio I_B/I_A versus temperature from 10 K to 40 K.

opposite case: X_B dominates the PL spectrum. Similar analyses have been done at higher temperatures from 20 K to 40 K (see Fig. 4.11(a)-(c)) that give similar results. With increasing temperature, the intensity ratio I_B/I_A increases (see Fig. 4.11(d)).

To gain insights into the asymmetric PL profile, we employ a kinetic three-level model illustrated in Fig. 4.10(c) to describe the population of excitons A and B. The schematic energy diagram includes ground state $|0\rangle$, excitonic bands A (red curve) and B (blue curve), where the curvatures are proportional to the estimated effective masses μ_A and μ_B. The rate equations are given as:

$$\frac{dN_A}{dt} = G_A - \Gamma_A N_A - \gamma_{A\to B} N_A + \gamma_{B\to A} N_B, \tag{4.1}$$

$$\frac{dN_B}{dt} = G_B - \Gamma_B N_B - \gamma_{B\to A} N_B + \gamma_{A\to B} N_A, \tag{4.2}$$

where G_A and G_B are generation rates of excitons at levels A and B, respectively,

satisfying $G_A + G_B = 1$. Γ_A and Γ_B are radiative recombination rates of X_A and X_B, respectively, satisfying $\Gamma_A/\Gamma_B \approx F_A/F_B \sim 3$. Thermal coupling between A and B bands occurs via absorption or emission of phonons whose energies matches Δ_{BA}. The non-radiative $A \rightarrow B$ and $B \rightarrow A$ relaxation rates are given by $\gamma_{A\rightarrow B} = \gamma_o p(T)$ and $\gamma_{B\rightarrow A} = \gamma_o(p(T)+1)$, respectively, where γ_o is the relaxation rate at zero-temperature and $p(T) = (\exp(\Delta_{BA}/k_BT) - 1)^{-1}$ is the Bose-Einstein phonon population at lattice temperature T.

The solution of Eq. (4.1) and (4.2) in the steady-state regime (*i.e.*, $dN_{A(B)}/dt = 0$) yields the PL intensity ratio between X_A and X_B as:

$$\frac{I_B}{I_A} = \frac{G_B + \gamma_{A\rightarrow B}/\Gamma_A}{G_A + \gamma_{B\rightarrow A}/\Gamma_B}. \tag{4.3}$$

The solution at 10 K can be further simplified by noting that $A \rightarrow B$ requires the absorption of the Δ_{BA} phonon mode. At 10 K, this process is negligible ($p \approx 0$), while phonon emission is always possible ($p + 1 \approx 1$). Therefore, exciton flow from $A \rightarrow B$ ($B \rightarrow A$) is forbidden (allowed). The relaxation rate $\gamma_{B\rightarrow A}$ is factorized in terms of Γ_B for a dimensional analysis.

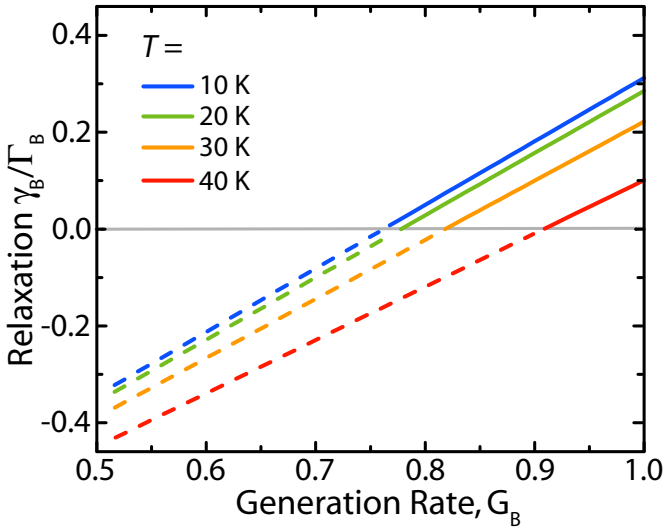

Figure 4.12: Non-radiative relaxation rate $\gamma_{B\rightarrow A}$ factorized in terms of radiative recombination rate Γ_B as a function of the generation rate (G_B) of electron-hole pairs at the high-energy level B. With increasing temperature, G_B shifts to higher values and $\gamma_{B\rightarrow A}$ decreases.

To explain the asymmetric PL profile, we focus on the solutions of Eq. ((4.3)). Given the experimental intensity ratio $I_B/I_A \sim 3.2$, we find physical solutions for $\gamma_{B\rightarrow A}$ only if the generation rates of excitons A and B are inequivalent. Specifically, we

find the minimum (maximum) threshold as G_B = 0.76 (G_A = 0.24) (see Fig. 4.12). The generation rates imply that at least 76 percent of photo-generated carriers form free-excitons at level B. The more electron-hole pairs are generated at the B-band, the faster they relax from B to A. Considering the extreme case, where all excitons are created at level B (*i.e.* G_B = 1, G_A = 0), $\gamma_{B\rightarrow A}$ reaches its maximum value at $\sim$0.3 Γ_B. It means that non-radiative relaxation of excitons from $B \rightarrow A$ is much slower than direct radiative recombination from high-energy level B. We argue that exciton generation and relaxation pathways may depend on excitation wavelength. Here, under non-resonant excitation, electron-hole pairs are more efficiently created at level B. The non-equivalent generation rates of excitons at A- and B-bands, together with long relaxation time constant ($T_{B\rightarrow A} = 1/\gamma_{B\rightarrow A}$), explain for the highly asymmetric profile of the low-temperature PL spectrum (see Fig. 4.10 and Fig. 4.11).

In this simplified model, the increment of I_B/I_A implies that the higher the temperature, the more asymmetric the generation rates and the slower the relaxation from B to A. The increase of Δ_{BA} with increasing temperature also leads to lower relaxation rate $\gamma_{B\rightarrow A}$. Longer relaxation times at higher temperatures explain for the stronger contribution of free-excitons that radiatively recombine from level B to the PL spectrum with increasing temperature. In order to describe the underlying physics behind the slow exciton dynamics in organo-lead halide perovskites, one may need to consider Rashba effects, internal electric fields and dynamic disorder of the organic moieties [37, 38].

4.3 Conclusion

We have shown that high-quality lead halide perovskite crystals provide a powerful platform to investigate the fundamental optical properties of these semiconductors. We have shown that different classes of free-exciton transitions are responsible for the optical responses of perovskite materials at low temperature. We find distinctive binding energies for high- and low-energy excitons. These results reconcile the wide range of exciton binding energies reported in lead halide perovskites. Moreover, we find that under non-resonant photo-excitation, electron-hole pairs are more efficiently created at the high-energy band, and the subsequent non-radiative relaxation time to the low-energy level, is longer than exciton radiative lifetime that are responsible for the counter-intuitive PL profile. Since semiconducting lead halide perovskites share similar electronic band structures, our results are general for other compounds and may be considered for future

theoretical calculations.

References

1. D'Innocenzo, V., Grancini, G., Alcocer, M. J., Kandada, A. R. S., Stranks, S. D., Lee, M. M., Lanzani, G., Snaith, H. J. & Petrozza, A. Excitons versus free charges in organo-lead tri-halide perovskites. *Nat. Commun.* **5** (2014).

2. Lin, Q., Armin, A., Nagiri, R. C. R., Burn, P. L. & Meredith, P. Electro-optics of perovskite solar cells. *Nat. Photonics* **9,** 106–112 (2015).

3. Tanaka, K., Takahashi, T., Ban, T., Kondo, T., Uchida, K. & Miura, N. Comparative study on the excitons in lead-halide-based perovskite-type crystals $CH_3NH_3PbBr_3$ and $CH_3NH_3PbI_3$. *Solid State Commun.* **127,** 619–623 (2003).

4. Sestu, N. *et al.* Absorption F-sum rule for the exciton binding energy in methylammonium lead halide perovskites. *J. Phys. Chem. Lett.* **6,** 4566–4572 (2015).

5. Kunugita, H. *et al.* Excitonic feature in hybrid perovskite $CH_3NH_3PbBr_3$ single crystals. *Chem. Lett.* **44,** 852–854 (2015).

6. Tilchin, J., Dirin, D. N., Maikov, G. I., Sashchiuk, A., Kovalenko, M. V. & Lifshitz, E. Hydrogen-like Wannier-Mott excitons in single crystal of methylammonium lead bromide perovskite. *ACS Nano* **10,** 6363–6371 (2016).

7. Galkowski, K. *et al.* Determination of the exciton binding energy and effective masses for methylammonium and formamidinium lead tri-halide perovskite semiconductors. *Energy Environ. Sci.* **9,** 962–970 (2016).

8. Zheng, K., Zhu, Q., Abdellah, M., Messing, M. E., Zhang, W., Generalov, A., Niu, Y., Ribaud, L., Canton, S. E. & Pullerits, T. Exciton binding energy and the nature of emissive states in organometal halide perovskites. *J. Phys. Chem. Lett.* **6,** 2969–2975 (2015).

9. Comin, R., Walters, G., Thibau, E. S., Voznyy, O., Lu, Z.-H. & Sargent, E. H. Structural, optical, and electronic studies of wide-bandgap lead halide perovskites. *J. Mater. Chem. C* **3,** 8839–8843 (2015).

10. Saidaminov, M. I., Abdelhady, A. L., Murali, B., Alarousu, E., Burlakov, V. M., Peng, W., Dursun, I., Wang, L., He, Y., Maculan, G., *et al.* High-quality bulk hybrid perovskite single crystals within minutes by inverse temperature crystallization. *Nat. Commun.* **6,** 7586 (2015).

11. Shi, D. *et al.* Low trap-state density and long carrier diffusion in organolead trihalide perovskite single crystals. *Science* **347,** 519–522 (2015).

12. Sell, D., Dingle, R., Stokowski, S. & DiLorenzo, J. Observation of polaritons in GaAs: A new interpretation of the free-exciton reflectance and luminescence. *Phys. Rev. Lett.* **27,** 1644 (1971).

13. Lagois, J. & Hümmer, K. Experimental and theoretical effects of surface layers and spatial dispersion on the free exciton reflectance of ZnO. *Phys. Status Solidi (b)* **72,** 393–402 (1975).

14. Perna, G., Capozzi, V., Pagliara, S., Ambrico, M. & Lojacono, D. Reflectance and photoluminescence characterization of CdS and CdSe heteroepitaxial films deposited by laser ablation technique. *Thin Solid Films* **387,** 208–211 (2001).

15. Mak, K. F., He, K., Shan, J. & Heinz, T. F. Control of valley polarization in monolayer MoS_2 by optical helicity. *Nat. Nanotech.* **7,** 494–498 (2012).

16. Fox, M. *Optical properties of solids* (Oxford University Press, 2010).

17. Kim, C., Lautenschlager, P. & Cardona, M. Temperature dependence of the fundamental energy gap in GaAs. *Solid State Commun.* **59,** 797–802 (1986).

18. Zilli, A., De Luca, M., Tedeschi, D., Fonseka, H. A., Miriametro, A., Tan, H. H., Jagadish, C., Capizzi, M. & Polimeni, A. Temperature dependence of interband transitions in wurtzite InP nanowires. *ACS Nano* **9,** 4277–4287 (2015).

19. Van Doorn, C. Temperature dependence of the energy-gap in ZnS. *Physica* **20,** 1155–1156 (1954).

20. Dey, P., Paul, J., Bylsma, J., Karaiskaj, D., Luther, J., Beard, M. & Romero, A. Origin of the temperature dependence of the band gap of PbS and PbSe quantum dots. *Solid State Commun.* **165,** 49–54 (2013).

21. Zhang, Q., Su, R., Liu, X., Xing, J., Sum, T. C. & Xiong, Q. H. High-quality whispering-gallery-mode lasing from cesium lead halide perovskite nanoplatelets. *Adv. Funct. Mater.* **26,** 6238–6245 (2016).

22. Amat, A., Mosconi, E., Ronca, E., Quarti, C., Umari, P., Nazeeruddin, M. K., Grätzel, M. & De Angelis, F. Cation-induced band-gap tuning in organohalide perovskites: interplay of spin–orbit coupling and octahedra tilting. *Nano Lett.* **14,** 3608–3616 (2014).

23. Foley, B. J., Marlowe, D. L., Sun, K., Saidi, W. A., Scudiero, L., Gupta, M. C. & Choi, J. J. Temperature dependent energy levels of methylammonium lead iodide perovskite. *Appl. Phys. Lett.* **106,** 243904 (2015).

24. Dar, M. I., Jacopin, G., Meloni, S., Mattoni, A., Arora, N., Boziki, A., Zakeeruddin, S. M., Rothlisberger, U. & Grätzel, M. Origin of unusual bandgap shift and dual emission in organic-inorganic lead halide perovskites. *Sci. Adv.* **2,** e1601156 (2016).

25. Gross, E. Optical spectrum of excitons in the crystal lattice. *Nuovo Cimento Suppl.* **3,** 672–701 (1956).

26. Kazimierczuk, T., Fröhlich, D., Scheel, S., Stolz, H. & Bayer, M. Giant Rydberg excitons in the copper oxide Cu2O. *Nature* **514,** 343–347 (2014).

27. Reynolds, D. C., Look, D. C. & Jogai, B. Optically pumped ultraviolet lasing from ZnO. *Solid State Commun.* **99,** 873–875 (1996).

28. Bagnall, D., Chen, Y., Zhu, Z., Yao, T., Koyama, S., Shen, M. Y. & Goto, T. Optically pumped lasing of ZnO at room temperature. *Appl. Phys. Lett.* **70,** 2230–2232 (1997).

29. Hanada, T. in *Oxide and Nitride Semiconductors* (Springer, 2009).

30. Whitfield, P., Herron, N., Guise, W., Page, K., Cheng, Y., Milas, I. & Crawford, M. Structures, phase transitions and tricritical behavior of the hybrid perovskite methyl ammonium lead iodide. *Sci. Rep.* **6,** 35685 (2016).

31. Diroll, B. T., Guo, P. & Schaller, R. D. Unique optical properties of methylammonium lead iodide nanocrystals below the bulk tetragonal-orthorhombic phase transition. *Nano Lett.* **18,** 846–852 (2018).

32. Hirotsu, S., Harada, J., Iizumi, M. & Gesi, K. Structural phase transitions in $CsPbBr_3$. *J. Phys. Soc. Jpn.* **37,** 1393–1398 (1974).

33. Protesescu, L., Yakunin, S., Bodnarchuk, M. I., Krieg, F., Caputo, R., Hendon, C. H., Yang, R. X., Walsh, A. & Kovalenko, M. V. Nanocrystals of cesium lead halide perovskites ($CsPbX_3$, X=Cl, Br, and I): Novel optoelectronic materials showing bright emission with wide color gamut. *Nano Lett.* **15,** 3692–3696 (2015).

34. Liu, Z., Shang, Q., Li, C., Zhao, L., Gao, Y., Li, Q., Chen, J., Zhang, S., Liu, X., Fu, Y., *et al.* Temperature-dependent photoluminescence and lasing properties of $CsPbBr_3$ nanowires. *Appl. Phys. Lett.* **114,** 101902 (2019).

35. Baikie, T., Fang, Y., Kadro, J. M., Schreyer, M., Wei, F., Mhaisalkar, S. G., Grätzel, M. & White, T. J. Synthesis and crystal chemistry of the hybrid perovskite $(CH_3NH_3)PbI_3$ for solid-state sensitised solar cell applications. *J. Mater. Chem. A* **1,** 5628–5641 (2013).

36. Geng, W., Zhang, L., Zhang, Y.-N., Lau, W.-M. & Liu, L.-M. First-principles study of lead iodide perovskite tetragonal and orthorhombic phases for photovoltaics. *J. Phys. Chem. C* **118,** 19565–19571 (2014).

37. Even, J., Pedesseau, L., Katan, C., Kepenekian, M., Lauret, J.-S., Sapori, D. & Deleporte, E. Solid-state physics perspective on hybrid perovskite semiconductors. *J. Phys. Chem. C* **119,** 10161–10177 (2015).

38. Azarhoosh, P., McKechnie, S., Frost, J. M., Walsh, A. & Van Schilfgaarde, M. Research update: Relativistic origin of slow electron-hole recombination in hybrid halide perovskite solar cells. *APL Mater.* **4,** 091501 (2016).

39. Zheng, F., Tan, L. Z., Liu, S. & Rappe, A. M. Rashba spin–orbit coupling enhanced carrier lifetime in $CH_3NH_3PbI_3$. *Nano Lett.* **15,** 7794–7800 (2015).

40. Niesner, D., Wilhelm, M., Levchuk, I., Osvet, A., Shrestha, S., Batentschuk, M., Brabec, C. & Fauster, T. Giant Rashba splitting in $CH_3NH_3PbBr_3$ organic-inorganic perovskite. *Phys. Rev. Lett.* **117,** 126401 (2016).

41. Umebayashi, T., Asai, K., Kondo, T. & Nakao, A. Electronic structures of lead iodide based low-dimensional crystals. *Phys. Rev. B* **67,** 155405 (2003).

42. Brandt, R. E., Stevanović, V., Ginley, D. S. & Buonassisi, T. Identifying defect-tolerant semiconductors with high minority-carrier lifetimes: Beyond hybrid lead halide perovskites. *MRS Commun.* **5,** 265–275 (2015).

43. Alias, M. S., Dursun, I., Saidaminov, M. I., Diallo, E. M., Mishra, P., Ng, T. K., Bakr, O. M. & Ooi, B. S. Optical constants of $CH_3NH_3PbBr_3$ perovskite thin films measured by spectroscopic ellipsometry. *Opt. Express* **24,** 16586–16594 (2016).

44. Nedelcu, G., Protesescu, L., Yakunin, S., Bodnarchuk, M. I., Grotevent, M. J. & Kovalenko, M. V. Fast anion-exchange in highly luminescent nanocrystals of cesium lead halide perovskites ($CsPbX_3$, X= Cl, Br, I). *Nano Lett.* **15,** 5635–5640 (2015).

45. Lanzani, G. *The photophysics behind photovoltaics and Photonics* (John Wiley & Sons, 2012).

Chapter 5

Coexistence of Anisotropic and Isotropic Exciton in Layered Lead Halide Perovskites

The fast growing field of atomically thin semiconductors urges for a profound understanding of non-hydrogenic two-dimensional excitons, which entirely determine the optical responses. Recent years have witnessed the resurgence of atomically-thin semiconductors with a variety of crystal lattices and exciton binding energies up to hundreds meV [1–3] that are suitable for investigating the peculiar excitonic properties induced by electron-hole exchange interactions. Here, we chose lead halide semiconductors with two-dimensional (2D) perovskite lattice as a representative of non-conventional 2D systems. The solution processable layer-structure offers unique opportunities for precisely manipulating Coulomb interaction through tuning quantum- and dielectric confinement while maintaining strong optical responses [3]. In this chapter, we will discuss coexistence of anisotropic and isotropic excitons in atomically-thin perovskite quantum-wells as a result of the interplay between the electron-hole exchange interaction, spin-orbit (Rashba) coupling and internal electric field. The exciton dynamics will be also presented.

5.1 Sample Preparation and Characterization

The two-dimensional perovskite $(PEA)_2PbI_4$ crystals were synthesized by a supersaturation precipitation method as previously reported in [4]. One mmol PbI_2 and 2 mmol PEAI were dissolved in 1 mL γ-butyrolactone solution. The precursor solution was stored in an open vial under ambient atmosphere. After several days, the solvent volatilized gradually and some flake-like crystals grew on the top surface of the solution. The single-crystal structure was confirmed by X-ray diffraction (see Fig. 5.1).

The crystal naturally grows in a stable layered structure, which comprises alternatively

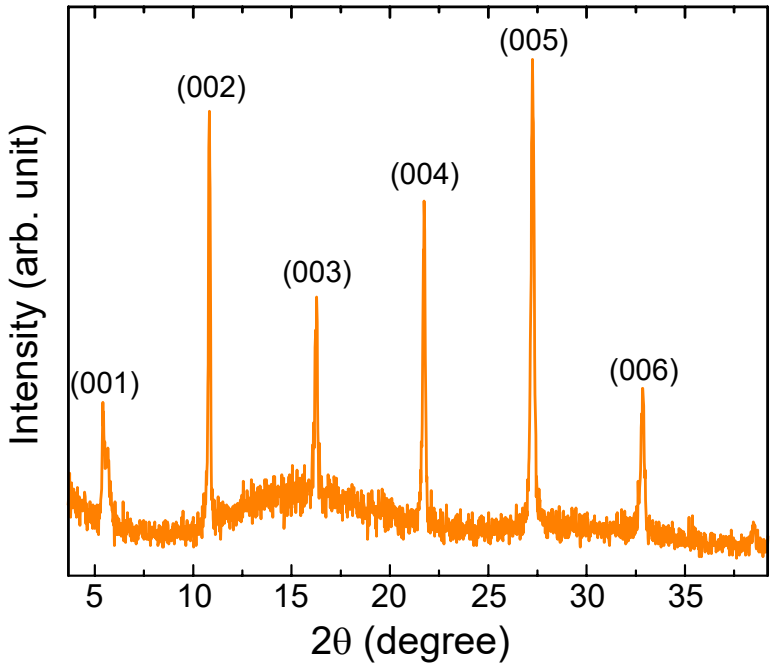

Figure 5.1: X-ray diffraction (XRD) spectrum of the synthesized 2D perovskite single crystal. The narrow lines of the XRD spectra indicates good crystallinity of the crystal.

stacked layers of $[PbI_6]^{4-}$ octahedra and long-chain organic molecules $C_6H_5C_2H_4NH_3^+$. The inorganic framework sandwiched between two organic barriers, forms (multiple) quantum-wells. Moreover, the minimal surface fluctuation and low defect-level severely diminish inhomogeneous broadening of the optical spectra that allows for the observation of the exciton fine-structure.

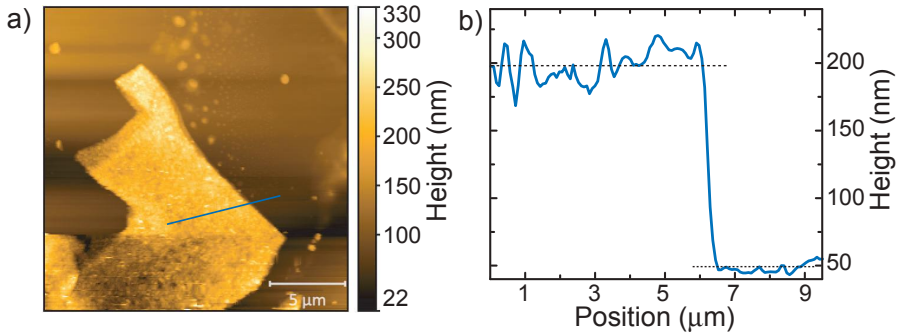

Figure 5.2: (a) AFM image of the exfoliated sample. (b) Height profile along the blue line, revealing the sample thickness of 149±12 nm. Considering the thickness of an inorganic $[PbI_6]^{4-}$ layer as 0.636 nm and of an organic $[PEA]^+$ layer as 1.004 nm, the investigated sample consists of approximately ∼182 barrier-well layers.

Due to weak interlayer forces, the as-synthesized 2D perovskite crystals can be mechanically exfoliated on a cleaned SiO_2/Si substrate using a scotch tape method, which has been widely applied for two-dimensional semiconductors with van der Waals bonded layers such as graphene and transition metal dichalcogenides (TMDs) [5]. The

produced flakes have lateral dimensions of micrometers and typical thickness ranging from few tens to hundreds nanometers. The samples having macroscopic continuity and hundred-nanometer thickness can be obtained with high and homogeneous optical quality. The data presented in this chapter belong to a nanostructure with micrometer in-plane dimensions and ∼150-nm thick (see Fig. 5.2), corresponding to about ∼91 couples of barrier-well layers. Noticeably, unlike TMDs, all of the perovskite flakes exhibit strong optical responses regardless of the number of layers. Furthermore, the samples are very stable in the experimental conditions, *i.e.* in high vacuum and at low temperature.

5.2 Bright Exciton Transitions

5.2.1 Reflectance and Photoluminescence

The sample was mounted in a cryostat fed by continuous flow of liquid helium. All the optical experiments were performed at $T \sim 5.9$ K (unless otherwise mentioned) in a back-scattering configuration as shown in Fig. 3.1. The excitation light sources, focused through a microscope objective (NA = 0.45), are a halogen white lamp for reflectance and a continuous-wave 488-nm laser for micro-photoluminescence (μ-PL) experiments. The excitation and detection represented by $\boldsymbol{k}_{\mathbf{Exc}}$ and $\boldsymbol{k}_{\mathbf{PL}}$ were aligned in parallel with the out-of-plane crystal $\boldsymbol{c}$-axis. The optical signals were collected by the same objective in a back-scattering configuration, dispersed by a single-grating (600 grooves/mm) spectrometer with 800-mm focal length and recorded by a nitrogen-cooled silicon-CCD camera.

Figure 5.3(a) shows the typical PL spectrum of the nanostructure. An emission peak arising at ∼2.3064 eV (X_1) exhibits a weak intensity and a linewidth of ∼15 meV. Interestingly, the spectrum is mainly contributed by the sharp features appearing at higher energies of ∼2.3368 eV (X_2) and ∼2.3418 eV (X_3), whose individual linewidths are ∼4.0 meV. At even higher energy, an emission structure arises at ∼2.3815 eV (X_4). The zoom-in view of X_4 (inset Fig. 5.3(a)) shows a comparable linewidth but an intensity of roughly three orders of magnitude weaker than X_3. The narrow PL linewidths are comparable to that of high-quality GaAs/AlGaAs and GaN/AlGaN quantum-wells structure [6, 7]. The spectral positions are consistent over many flakes, revealing the macroscopic homogeneity of the high-quality crystals.

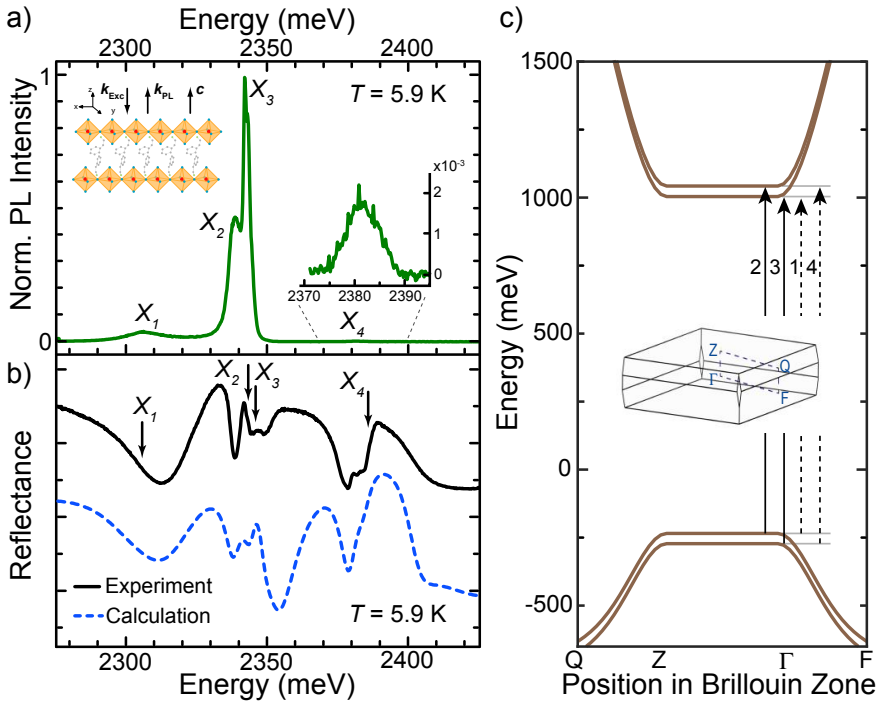

Figure 5.3: (a) Low-temperature photoluminescence spectrum showing intrinsic exciton transitions X_i (i = 1, 2, 3, 4). Inset: zoom-in view of X_4. (b) Low-temperature experimental (black solid curve) and calculated (blue dashed curve) reflectance spectra. The exciton resonances (X_i) are indicated by black arrows. (c) Electronic band structure of $(PEA)_2PbI_4$ showing the lowest-lying conduction and highest-lying valence bands around Γ-point of the first Brillouin zone. Optical transitions are labelled 1-4 from low-high energy, where solid (dashed) arrows illustrate large (small) oscillator strengths.

Reflectance spectra of the same layered nanostructure are presented in Fig. 5.3(b). The experimental curve (black solid line) contains multiple features within the PL energy range. Taking into account the superposition of excitonic resonances and multiple reflection/transmission events at the interfaces, we modelled the reflectance profile of the investigated perovskite multiple quantum-well sample, with N = 185 media, including the top vacuum, 91 pairs of organic-inorganic layers and SiO_2/Si substrate. The exciton contribution is considered in the complex dielectric function of the $[PbI_6]^{4-}$ layers, which consists of four oscillating dipoles associated to the four resonances X_i (i = 1, 2, 3, 4) in the PL spectrum (see Fig. 5.3(a)). The theoretical reflectance was calculated by using the transfer-matrix method as discussed in Chapter 3, Section 3.1.3. The calculated curve (blue-dashed-line) qualitatively reproduces the features in the experimental spectrum. Importantly, if any of the four X_i-dipoles is absent, the overall lineshape of the experimental reflectance cannot be reproduced (see Fig. 5.4). The non-zero oscillator strengths of all the X_i-transitions are signatures of intrinsic and optically active excitons.

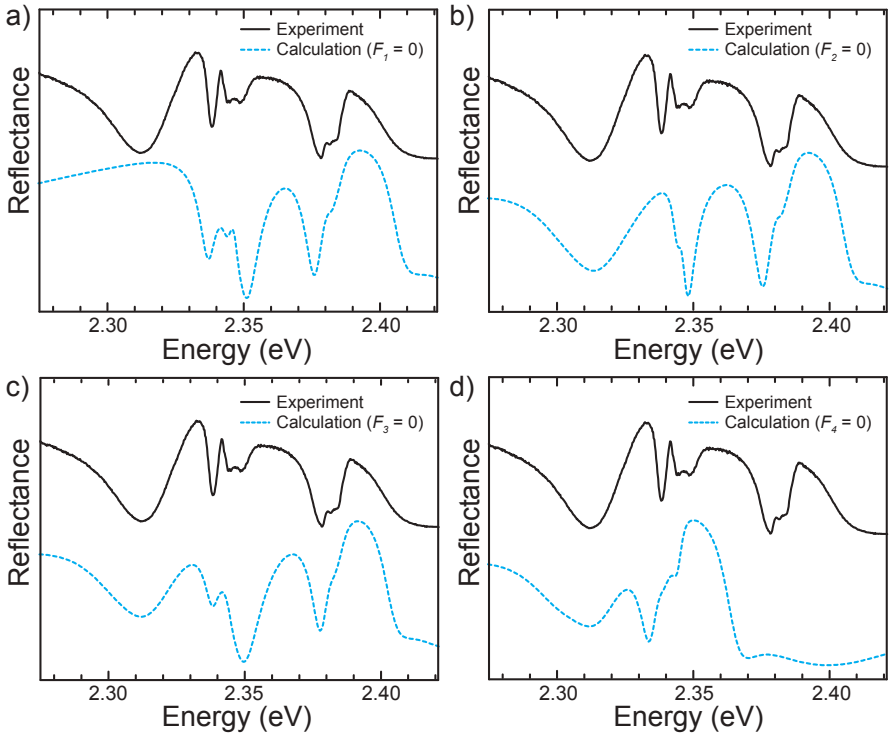

Figure 5.4: Calculated reflectance spectra when oscillator strength (F_i) of an individual transition (X_i) is set to zero: (a) $F_1 = 0$, (b) $F_2 = 0$, (c) $F_3 = 0$ and (d) $F_4 = 0$. As seen, if any of the exciton resonance is absent, the calculation (blue dashed lines) cannot reproduce the lineshape of experimental spectra (black solid lines). Therefore, all the observed features in the PL spectra carry non-zero oscillator strengths corresponding to optically allowed direct transitions.

The observed optical transitions are further supported by a band structure calculation. Figure 5.3(c) shows the band dispersions near the Γ-point in the first Brillouin zone. In each unit cell consisting of two inorganic layers and two organic layers sandwiched between them, an internal electric field, across the organic layers along z-direction, alters the confining potentials at the inorganic layers and makes the adjacent quantum-wells inequivalent. Therefore, the inorganic layers contribute different bands of distinct energies that lead to multiple transitions near the fundamental bandedge. Four optical transitions are labelled 1 to 4 for low- to high-energy, where the transitions 1 and 4 (dashed arrows) are weaker than the transitions 2 and 3 (solid arrows). The energy difference between the band-to-band transitions, $\Delta_{21} \sim 44.4$ meV, $\Delta_{32} \sim 3.2$ meV and $\Delta_{43} \sim 44.4$ meV, are in excellent agreement with experimental values (see Fig. 5.3(a)-(b)).

5.2.2 Anisotropic Linearly-Polarized Excitons

The exciton properties are studied by polarization-resolved luminescence using the setup shown in Fig. 3.1. Linear polarizers were used to calibrate the polarization response of the setup. The linear polarization of the excitation and detected photons were controlled by half-wave plates ($\lambda/2$) on the corresponding optical paths. At non-resonant excitation conditions (E_{Exc} = 2.5410 eV), we find that at a fixed detection angle (φ), the PL spectrum remains unchanged while varying the incident laser direction θ from 0 (red curve), π/2 (black curve) to π (gray curve) in the crystal plane (see Fig. 5.5(a)). The homogeneous spatial profile of the PL intensity (inset Fig. 5.5(a)) unambiguously indicates the in-plane isotropic perovskite lattice.

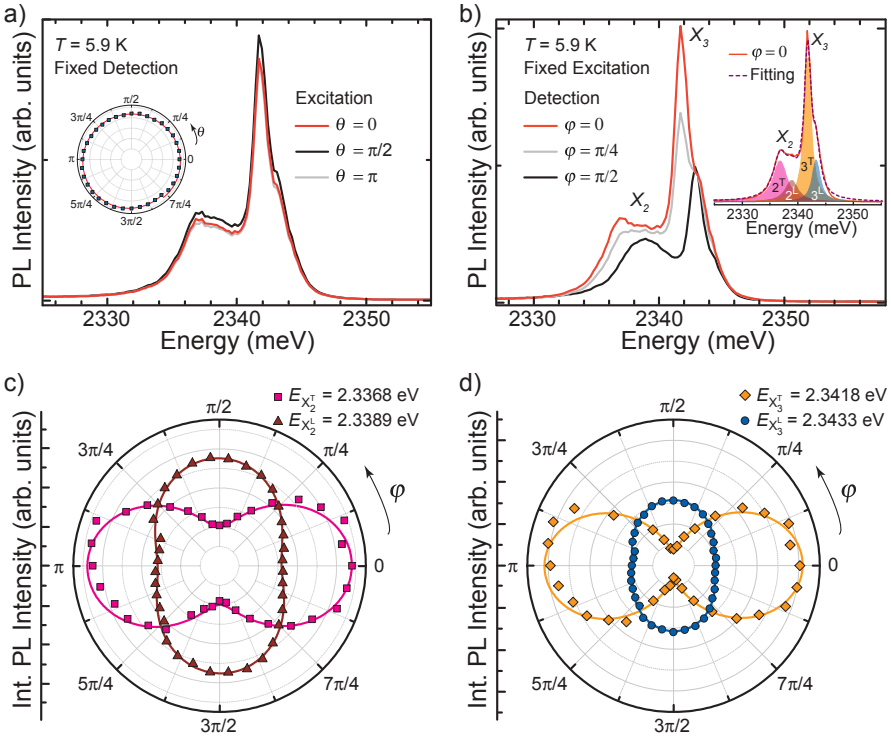

Figure 5.5: (a) PL spectra acquired at a fixed (linear) detection angle φ while varying the excitation (linear) polarization θ from 0 (red curve), π/2 (black curve) to π (gray curve). Inset: integrated PL intensity of X_2 and X_3 excitons by varying the linear polarization (θ) of the excitation (blue squares). The intensity profile is fitted by a sinusoidal function (red solid line). (b) Photoluminescence spectra at selected detection angles φ = 0 (red curve), $\pi/4$ (grey curve) and $\pi/2$ (black curve) by fixing the excitation polarization θ. Inset: typical fitting (violet dashed line) to a spectrum (red solid line) with four Lorentzian-shaped components (colour-filled areas). Integrated PL intensity versus φ for (c) X_2^T (pink squares), X_2^L (brown triangles) and (d) X_3^T (orange diamonds), X_3^L (blue circles). Coloured solid lines are sinusoidal fitting curves.

In contrast, by using any fixed excitation angle, the PL spectrum changes dramatically

with different detection polarization (see Fig. 5.5(b)). The PL emission intensity is the strongest when being detected in parallel to the polarization axis of the analyzer (φ = 0, red curve). It gradually weakens with increasing φ (grey curve) and becomes minimal when the detection direction is perpendicular to the analyzer ($\varphi = \pi/2$, black curve). Remarkably, the spectral position clearly shifts to higher energies when varying φ from 0 to $\pi/2$. The periodic intensity variation and reversible energy shift over a 2π-cycle reveal that the emissive X_2 and X_3 exciton features compose of strongly linearly-polarized components. Given the in-plane *isotropic* absorption of the two-dimensional perovskite lattice, the existence of *anisotropic* excitons is striking. Therefore, the linear polarization of X_2 and X_3 in layered perovskite nanostructures should be clearly distinguished from that observed in black phosphorous [8] or rhenium-dichalcogenides [9, 10], which exhibits anisotropic absorption in the crystal plane. Our results otherwise suggest that the anisotropic excitons in perovskite quantum-wells stem from the intrinsic electron-hole exchange interaction.

The PL spectrum can be well fitted by four Lorentzian-shaped curves (inset Fig. 5.5(b)) centered at 2.3368 eV (X_2^T), 2.3389 eV (X_2^L), 2.3418 eV (X_3^T) and 2.3433 eV (X_3^L). The peaks X_2^T and X_2^L, X_3^T and X_3^L are similarly broad pairwise with the linewidths of $\sim$1.9 meV. The fitting criteria including peak positions and full-widths at half-maxima are kept the same for all the polarization-resolved PL spectra, while the constituent intensities are parameterized and plotted against detection angle φ (coloured-symbols, Fig. 5.5(c),(d)). The intensity profiles, fitted by sinusoidal functions (coloured-solid-lines) clearly show the orthogonal orientation of the emitting dipoles X_2^T (X_3^T) and X_2^L (X_3^L). Furthermore, X_2^T and X_2^L orient in parallel with X_3^T and X_3^L, respectively. The high degree of optical alignment indicates the doublet multiplicity of the bright excitons X_2 and X_3, each of which is split into two singlets. From our statistical study (Table 5.1), the averaged longitudinal-transverse splitting is $\Delta_2^{\mathrm{LT}} \sim \Delta_3^{\mathrm{LT}} = (1.6 \pm 0.6)$ meV, while the energy separation between X_2 and X_3 is $\Delta_{32} = (4.4 \pm 1.0)$ meV. Interestingly, the resolved energy spacings are one-order-of-magnitude larger than the longitudinal-transverse splitting of excitons in GaAs QWs [11]. Moreover, $\Delta_{2,3}^{\mathrm{LT}}$ are comparable to the bright exciton fine-structure splitting in nanocrystals such as II-VI [12], MoS_2 [13], $CsPbBr_3$ [14] and larger than that in $CsPbI_3$ perovskite quantum dots [15].

Table 5.1: Electron-hole exchange interaction energies.

Sample No.	Δ_2^{LT} (meV)	Δ_3^{LT} (meV)
1	2.0	1.9
2	1.5	2.2
3	1.3	1.5
4	1.2	1.4
5	1.4	1.6
6	2.3	1.9
7	2.1	1.5
8	1.0	1.1
Average	1.6 ± 0.6	1.6 ± 0.6

5.2.3 Exchange Interaction versus Zeeman Effects in Magnetic Field

The origin of the exchange-induced fine-structure splitting is revealed by using a strong external magnetic field, which is a powerful tool to investigate the exciton fine-structure in semiconductors. Figure 5.6(a) shows an intensity mapping of the unpolarized-resolved PL spectra as a function of B-field strength in Faraday configuration ($\boldsymbol{B} \parallel \boldsymbol{k}_{\mathbf{Exc}} \parallel \boldsymbol{c}$). At zero-field, an energy splitting of $\sim$1.3 meV is observed between L- and T-branches of X_2 and of X_3. The energy positions of the L- and T-components are nearly constant until $\sim$5 T. As the field strength increases, these modes are progressively further separated, and a splitting of $\sim$3.1 meV is clearly resolved at the highest employed B-field (30 T). The quasi-linear field-dependence of the energy separation between the subbands reveals that the magnetic response is entirely dominated by Zeeman effects. The diamagnetic shift is negligible due to the tightly-bound character of the excitons.

In addition to the energy shifts, a strong magnetic field alters the polarization properties of the PL emission. It induces a circular polarization on the PL of the exciton subbands as shown in Fig. 5.6(b). For instance, at B = 10 T the σ^+- and σ^--detected PL spectra exhibit different profiles. While X_2^T and X_3^T dominate the σ^--detected (red curve) spectrum, X_2^L and X_3^L become more pronounced in σ^+-configuration (blue curve). Within the energy range of interest, each spectrum was fitted by four Lorentzian peaks, where the energies and full-widths at half-maxima were kept the same at each field. The degree of circular polarization (DCP) is quantified as $\mathrm{DCP} = (\mathrm{I}_{\sigma^-} - \mathrm{I}_{\sigma^+})/(\mathrm{I}_{\sigma^-} + \mathrm{I}_{\sigma^+})$, where I_{σ^-} (I_{σ^+}) denotes the PL intensity of each component collected by σ^- (σ^+)-

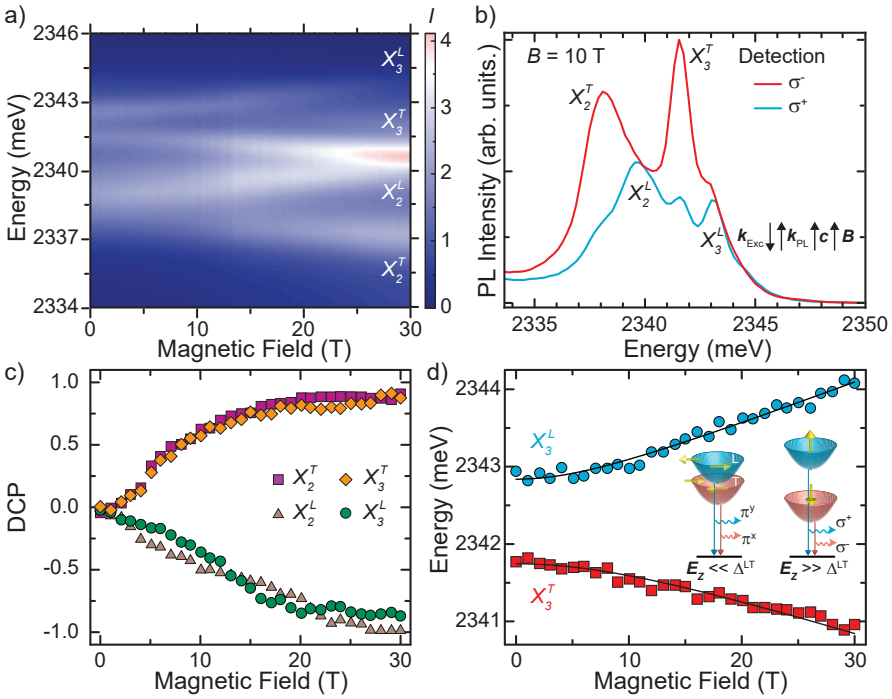

Figure 5.6: (a) Intensity mapping of the unpolarized-resolved PL spectra in a Faraday configuration ($\boldsymbol{B} \parallel \boldsymbol{c} \parallel \boldsymbol{k}_{\mathbf{exc}} \parallel \boldsymbol{k}_{\mathbf{PL}}$) in magnetic fields from 0 to 30 T. (b) Circularly-polarized resolved σ^- (red curve) and σ^+ (blue curve) PL spectra at B =10 T. (c) Magnetic-field-dependent degree of circular polarization of longitudinal (X_2^L, green circles; X_3^L, brown triangles) and transverse (X_2^T, pink squares; X_3^T, orange diamonds) excitons subbands. (d) Energies of X_3^L (blue circles) and X_3^T (red squares) as a function of B. The fitting (black curves) includes long-range e-h exchange (Δ^{LT}) and Zeeman energies ($E_Z = g_X \mu_B$). Inset: scheme illustrating the polarization and spin-configurations (yellow arrows) of the X^L (blue paraboloid) and X^T (red paraboloid) exciton subbands at low- ($E_Z \ll \Delta^{\mathrm{LT}}$) and at high-fields ($E_Z \gg \Delta^{\mathrm{LT}}$) limits.

detection.

Figure 5.6(c) shows the DCP of X_2^T (pink squares), X_2^L (brown triangles), X_3^T (orange diamonds) and X_3^L (green circles) as a function of magnetic field. For all components, the DCP starts from zero and remains below 10% at below ∼5 T, then increases linearly with increasing B and eventually saturates at ∼90% at ∼20 T. The DCP arises from the population contrast between spin-up and spin-down excitons via the Zeeman splitting induced by high magnetic fields. The field-dependent energies of X_3^T (red squares) and X_3^L (blue circles) are shown in Fig. 5.6(d) as a prototypical example. The energy for each subband in the magnetic field can be described by [16]:

$$E_X^{\mathrm{L,T}}(B) = E_X^{\mathrm{L,T}}(0) \pm \frac{1}{2}\sqrt{(\Delta^{\mathrm{LT}})^2 + (g_X \mu_B B)^2}, \tag{5.1}$$

where Δ^{LT} denote the longitudinal-transverse splitting induced by the long-range e-h exchange interaction at zero-field, g_X is the effective exciton gyromagnetic factor and μ_B is the Bohr magneton. The "$+$" and "$-$" signs describe the increasing and decreasing energies of the X^L and X^T subbands, respectively. By fitting the data to Eq. (5.1), effective g-factors for X_2 and X_3 are determined as $(+1.7 \pm 0.1)$ and $(+1.8 \pm 0.1)$, respectively. The obtained values are comparable to other lead-iodide perovskites crystals [17–19].

The magnetic-field response of the exciton doublets X_2 and X_3 prove the assignment of Δ^{LT} to be resulted from e-h exchange interactions. At zero-field, spin-up and spin-down excitons gets mixed by an unconventionally strong long-range electron-hole exchange interaction that opens a sizeable energy gap (fine-structure) at bright exciton bands. A pair of orthogonally oriented longitudinal and transverse excitons (blue and red paraboloids, Inset Fig. 5.6(d)) arises that carry in-plane spins (yellow arrows). In combination with the propagation of excitons along a preferential direction, the light emission is linearly-polarized at B = 0 T. At low magnetic fields ($g_X \mu_B B \ll \Delta^{\mathrm{LT}}$), the mixing between exciton spin-up and spin-down is strong, resulting in no apparent change in the energy of L- and T-subbands (Fig. 5.6(a),(d)) and the DCP of the PL emission remains small (Fig. 5.6(b),(c)). At intermediate fields, the Zeeman energy starts overcoming the effect of the e-h exchange interaction and the subbands get further separated (Fig. 5.6(d)) that is directly correlated with the increase of DCP of X^L and X^T components (Fig. 5.6(c)). At the limit of high fields ($g_X \mu_B B \gg \Delta^{\mathrm{LT}}$), all energies shift linearly and show a large separation. Concomitantly, a high degree of circular polarization can be resolved, due to the well-defined orientation of out-of-plane exciton spin-up and spin-down that selectively couple to $\sigma^{\pm}$-light (Inset Fig. 5.6(d)). The magnetic-field dependency of the energy shift and the switch from linear to circular polarization of the light emission at high magnetic fields, clearly reveals the strong exchange-induced splitting of bright excitons into L- and T-modes in layered perovskite semiconductors at zero-magnetic field.

5.2.4 Isotropic Spin-Polarized Excitons

On the other hand, the PL emission of exciton X_1 is not linearly polarized (see Fig. 5.7). Instead, it exhibits circular ($\sigma^{\pm}$) polarization, which is induced either by resonant excitation with circularly polarized light or by external magnetic fields. Figure 5.8(a) shows

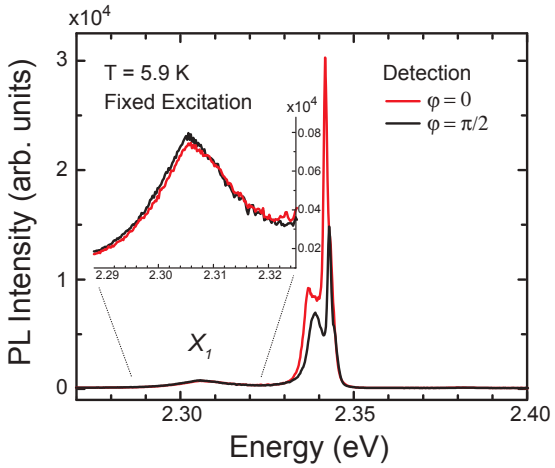

Figure 5.7: Full PL spectra taken with a fixed excitation polarization while varying the detection angle φ = 0 (red curve) and $\pi/2$ (black curve). While X_2 and X_3 show strong linear polarization, the PL intensity of X_1 is unchanged (inset). It indicates that X_1 is an isotropic exciton.

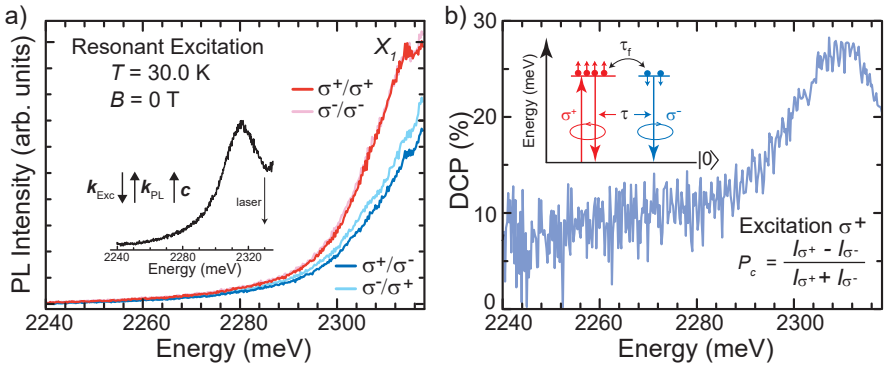

Figure 5.8: (a) Circularly polarized PL spectra under resonant excitation (E_{Exc} = 2.3308 eV, inset). Varying the polarization of excitation and detection between σ^+ and σ^-, results in co-polarized: σ^+/σ^+ (red curve), σ^-/σ^- (pink curve) and counter-polarized: σ^+/σ^- (blue curve), σ^-/σ^+ (light-blue curve) spectra. (b) Degree of circular polarization under resonant σ^+-excitation. Inset: energy diagram illustrating the light-induced spin-polarization of X_1, resulted from the competition between spin-flip $(1/\tau_f)$ and radiative recombination $(1/\tau)$ rates. (c) Circularly-polarized σ^+ (orange curve) and σ^- (violet curve) PL spectra at T = 5.9 K under magnetic field (B = 7 T) in a Faraday geometry. (d) Degree of circular polarization versus magnetic field. Inset: energy diagram illustrating the spin-subbands of X_1 split by the Zeeman effect. The symbols involved in the rate equation model are shown.

four PL spectra by using resonant excitation at E_{Exc} = 2.3308 eV (inset). Resonantly excited by σ^+ (σ^-)-polarized light, the PL spectrum acquired with the σ^+ (σ^-)-detection is depicted by the red (pink) curve. In these co-polarization configurations, *i.e.* σ^+/σ^+ and σ^-/σ^-, the PL emission has maximum intensity, whereas, it becomes weaker in the counter-polarization configurations, *i.e.* σ^+/σ^- (blue-curve) and σ^-/σ^+ (light-blue-

curve). Consequently, a net degree of circular polarization (DCP), quantified by a helicity parameter $P_c = (I_{\sigma^+} - I_{\sigma^-})/(I_{\sigma^+} + I_{\sigma^-})$, where I_{σ^+} (I_{σ^-}) denotes the integrated PL intensity collected by σ^+ (σ^-)-detection while using σ^+-excitation, can be obtained as a function of photon energy (see Fig. 5.8(b)).

We attribute the DCP to the optically induced spin-polarization of X_1. Under a resonant excitation, the σ^+ (σ^-)-polarized photons are directly converted into spin-up (spin-down) excitons, given by the optical selection rule. The competition between the spin-flip ($1/\tau_f$) and the radiative recombination ($1/\tau$) rates determines the steady-state equilibrium of the light-induced imbalance in the spin-population (inset Fig. 5.8(b)), resulting in a nonzero circular polarization of the PL. In our perovskite quantum-wells, the spin-injection reaches the maximum value of $\sim$27% at the peak energy of X_1. The resolved spin-polarization suggests comparable spin-flip and radiative recombination rates of excitons in lead-halide perovskites.

5.3 Discussion

The rich phenomenology of multiple exciton transitions in the two-dimensional perovskite nanostructures strongly suggests a non-trivial electronic energy spectrum. Previously reported PL spectra on similar compounds ($(C_4H_9NH_3)_2PbBr_4$, $(C_6H_{13}NH_3)_2PbI_4$) composed of totally four emission features [1, 18, 20]. The most intense peaks were assigned to recombination of optically-passive (dark) excitons [18], which were disallowed by spin selection rule and by geometrical configuration ($\boldsymbol{k_{Exc}} \perp \boldsymbol{c}$), respectively. In addition, the lowest-energy emission channel was attributed to biexciton luminescence formed from the weakly emitting and higher-lying exciton, which was assigned to the only optically-active (bright) band. This previously proposed picture, mostly elaborated by optically-forbidden transitions, cannot explain the various optically-allowed exciton bands in our experiment, which are corroborated by bright and narrow PL emission, non-zero oscillator strengths and prominent polarization properties. In the following, we will discuss in more details the origin and properties of the excitons in 2D perovskites.

5.3.1 Electron-Hole Exchange Interaction

We attribute the spatial anisotropy of bright excitons X_2 and X_3 to the constituent longitudinal and transverse excitons of the degenerated X_2 (and X_3) bands, whose

dipole moments are perpendicularly oriented. The energy spacing (Δ_2^{LT}, Δ_3^{LT}) is caused by the non-analytical long-range part of the electron-hole exchange interaction. Since the Coulomb e-h exchange interaction is proportional to the overlap between electron- and hole-wavefunctions [11, 21], it is substantially enhanced for tightly bound electron-hole pairs within the same quantum-well layer. The long-range exchange splitting is $\sim$2.0 meV in $(PEA)_2PbI_4$, which is remarkably larger than the exchange-induced fine-structure splitting in conventional III-V quantum-wells [7, 11] and comparable to that in monolayer transition-metal-dichalcogenides [22, 23] predicted by theory. Such a sizeable e-h exchange interaction clearly evidences for the large oscillator strengths, and therefore, the bright nature of excitons X_2 and X_3.

5.3.2 Internal Electric Field and Rashba Effect

Although the e-h exchange interaction produces longitudinal and transverse modes in X_2 and X_3 excitons, no linear polarization or preferential optical alignment is resolved on the lowest-energy exciton band X_1. Alternatively, the considerable spin-polarization is resolved. The vanishing electron-hole exchange interaction on the X_1 branch can originate from the symmetry of involved electronic bands and/or the reduced overlap between electron- and hole-wavefunctions [11, 21], while the latter one is the dominant factor. The reduction of wavefunction overlap likely arises from the indirect-like character of X_1 in real and/or momentum space.

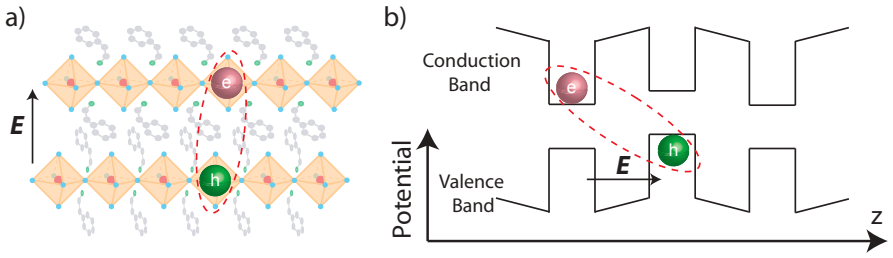

Figure 5.9: (a) Upon excitation, electrons and holes are generated in the inorganic layers. Due to Coulomb interaction, the electron and hole in different quantum-well layers can bound together to form an interlayer exciton. (b) The theoretical calculation reveals a local electric field across the layers in one unit cell, leading to the tilting of the band alignment. As a result, an optical transition energy can occur from the interlayer excitons, whose energy is smaller and oscillator strength is weaker than those of intralayer excitons.

The calculation suggests that electrons and holes of X_1 separately lie on the adjacent inequivalent quantum-well layers as a result of the internal electric field (see Fig. 5.9).

The carriers can couple via Coulomb interaction to form interlayer exciton. The spatial separation lessens the e-h wavefunction overlap.

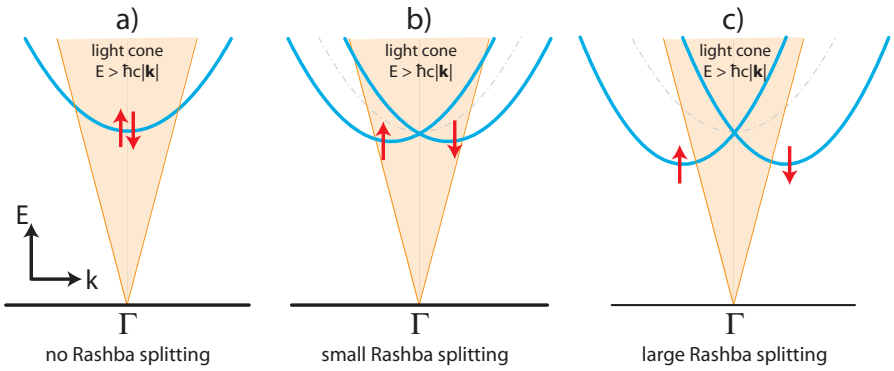

Figure 5.10: Momentum-indirect exciton induced by Rashba effects. Different scenarios are shown for (a) no Rashba splitting, *i.e.*, direct transition, (b) small Rashba splitting within the light-cone, *i.e.*, indirect-like transition but still optically allowed and (c) large Rashba splitting out of the light-cone, *i.e.*, indirect transition and opticaly forbidden.

On the other hand, the transition at X_1 can also be momentum-indirect. The interfacial disorder in the layered structures may break the inversion symmetry of the crystal and cause a Rashba term, which splits the band in momentum space and simultaneously introduce momentum-dependent spin-polarized states on the X_1 band (see Fig. 5.10 for different splitting scenarios). The Rashba-split bands with opposite spin orientations can selectively couple to circularly polarized light. In lead-halide perovskites, the momentum-splitting in conduction and valence bands is not exactly identical causing a slight momentum mismatch at the band extrema [24]. As a result, the overlap between electron- and hole-wavefunctions is reduced and the e-h exchange interaction is consequently suppressed. In both scenario, while the inherent indirect-like properties, caused by the internal electric fields and/or Rashba effects, turn the optical transition X_1 darker, Coulomb interaction keeps its oscillator strength non-zero. However, we argue that Rashba effects may be important to explain the spin-polarization found on X_1. The Rashba-split bands with opposite spin orientations selectively couple to circularly polarized photons. Future calculation considering additional terms such as electron-hole exchange interaction and Rashba effects will be needed.

In further details, the whole feature located at $\sim$2.3064 eV might arise not only from X_1 radiative recombination, but also other exciton species. By continuous excitation, the PL intensity of this structure increases linearly with excitation power, while at high pumping fluences, it shows a sub-quadratic power-dependence (see Fig. 5.11). Hence,

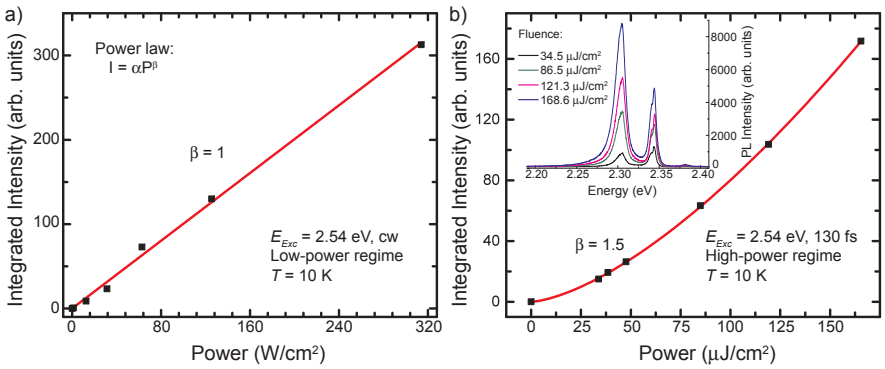

Figure 5.11: Integrated intensity I of the X_1 peak plotted as a function of excitation power (black squares) at (a) low-power regime using continuous-wave laser and at (b) high-power regime using femtosecond laser. The data are fitted by power law $I = \alpha P^{\beta}$ (red line), where α is the power coefficient, P is the excitation power and β determines the linear/non-linear processes. By using low power, the emission of X_1 increases linearly with P (β = 1), resembling exciton behaviour. Further increasing laser power results in the superlinear power-dependence with β = 1.5 ($<$2). Therefore, we argue that at high-power excitation, the whole feature at $\sim$2.3064 eV (at T = 5.9 K) may contain not only exciton X_1 but also higher-order exciton species. Further experiments are required to unravel all the components of the whole feature.

we do not exclude that when using strong laser power, biexciton luminescence might arise at energies close to exciton X_1. Further experiments are required to unravel all the components of the whole feature.

5.4 Exciton Dynamics

The exciton dynamics in 2D perovskite are studied intensively by transient absorption (TA) and time-resolved photoluminescence (TRPL) spectroscopy. Each technique is useful for a certain timescale. While TA works for ultrafast processes occurring within subpico- to pico-second, TRPL probes the radiative processes occurring in tens of pico- to nano-second timescale.

5.4.1 Linear Absorption

Figure 5.12 shows the linear absorption spectrum of the 2D perovskite flake acquired at T = 10 K (black solid line). The spectrum exhibits a broad feature at $\sim$2.4 eV that lie in the range of the exciton resonances in the reflectance and PL spectra (see Fig. 5.3). On the high-energy side, the continuum band appears with a broadening at the bandedge and remains almost constant at higher energy. This behaviour is resulted from

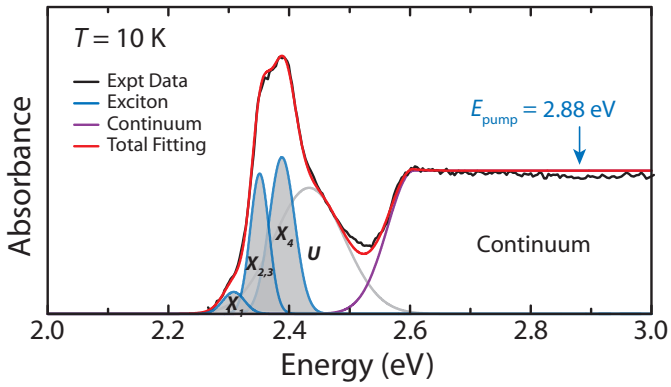

Figure 5.12: Low-temperature linear absorption spectrum (T = 10 K) of 2D perovskite. The experimental absorption spectrum (black solid line) shows the exciton features at the same energy range as observed in the reflectance and PL measurements. The spectrum is decomposed into exciton components (blue solid lines), modelled by Gaussian curves and continuum band (purple solid line), modelled by the convolution of a Gaussian and Heaviside functions as derived in Eq. (2.28). An energy structure U (gray solid line) arises on the high-energy side of the excitons. The overall fitting (solid red line) agree well with the experimental data. In transient absorption measurement, the excitation energy was $E_{\text{pump}} = 2.88$ eV.

the energy-independent density of state, which is typical in two-dimensional systems (see Fig. 1.1(b) and Eq. (2.28)).

The absorption spectrum is decomposed into exciton and continuum components. The exciton resonances X_i (i = 1, 2, 3, 4) are modelled by Gaussian-shaped curves (blue solid lines and grey shaded areas), whose peaks are set to the corresponding energies observed in the reflectance measurement. Due to the small energy separation between X_2 and X_3 ($\sim$5 meV), which is comparable to the energy-resolution of the setup, they will be discussed under a common notation $X_{2,3}$. In particular, the energies of X_1, $X_{2,3}$ and X_4 are (2.307$\pm$0.001) eV, (2.349$\pm$0.003) eV and (2.388$\pm$0.001) eV, respectively. The absorption from the continuum band is fitted by the convolution of a Gaussian, for the edge broadening, and a Heaviside function, for the high-energy region (purple solid line). The bandedge is determined to be $\sim$2.55 eV. Therefore, the binding energies of the exciton ($E_b = E_g - E_X$) in this structure are in the range of $\sim$200 meV. A broad feature (gray solid line) growing in between X_4 and the bandedge may arise from the excited exciton states and/or phonon-assisted transition. Further experiments are required to explicate the origin of U. The total fitting is given by the red solid line, which agrees well with the experimental data.

From the understanding on the energy structures, we proceed to get more insights

into the exciton dynamics, particularly how excitons form and decay after the photo-excitation. The transient absorption measurements were conducted by using a non-resonant excitation, E_{pump} = 2.88 eV.

5.4.2 Exciton Formation and Relaxation

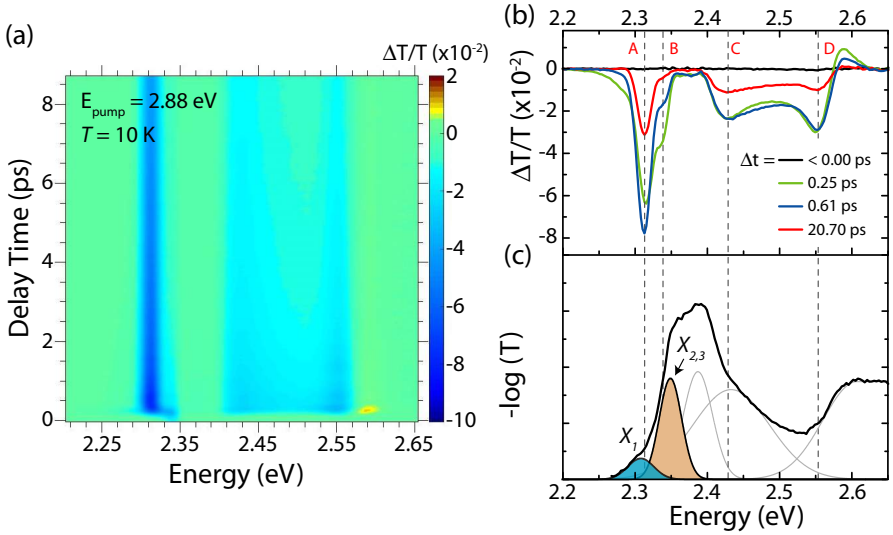

Figure 5.13: Transient absorption at low-temperature ($\boldsymbol{T}$ = 10 K). (a) Pseudo-color ($\Delta T/T$) representation of transient transmission spectra for the 2D perovskite flake using excitation energy of 2.88 eV with pumping fluence of 4.7 μJcm^{-2}. The average number of excited electron-hole pairs is $N \sim 10^{13}$ cm^{-2}. (b) Transient transmission spectra at selected pump-probe time delays from 0.25 ps to 20.7 ps (colored solid lines). Four main features are denoted as A, B, C, D. (c) The linear absorption spectrum (black solid line) together with its compositions including X_1 (blue shaded area), $X_{2,3}$ (pink shaded area) and others (gray solid lines) shown for easy comparison with (b).

Figure 5.13(a) shows the pseudo-color representation of the transient transmission ($\Delta T/T$) as a function of probe energy and delay time (Δt), obtained by using non-resonant excitation (E_{pump} = 2.88 eV) at T = 10 K. The pumping fluence of 4.7 μJcm^{-2} was used to create an average number of excited electron-hole pairs of $\sim 10^{13}$ cm^{-2}. We observe four pronounced pump-induced absorption (PIA) features (negative $\Delta T/T$) located at below 2.35 eV and around $\sim$2.40-2.55 eV. On the high-energy side, a pump-induced bleaching (PIB) feature (positive $\Delta T/T$) arises at $\sim$2.58 eV. The dynamic process first starts with the growth of a PIA feature at $\sim$2.34 eV, which decays very fast at early time. During the decay of this feature, the signals from the other PIA and PIB features raise. The extracted transient transmission spectra at selected time delay in the first 20 ps are shown in Fig. 5.13(b) by the colored curves. Four main PIA features are

labelled as A, B, C, D from low to high energy. The linear absorption spectrum and its compositions are shown in Fig. 5.13(c) in the same energy scale for easy comparison. Particularly, we find that the energy of A and B are close to the exciton resonances X_1 and $X_{2,3}$, while C matches with the broad feature U. The energy of D and the accompanied PIB occur at the band edge. Surprisingly, no PIB is observed at the exciton resonances in our TA spectra that is in contrast to the widely reported TA features in perovskite [25–29] as well as other semiconductors [30, 31].

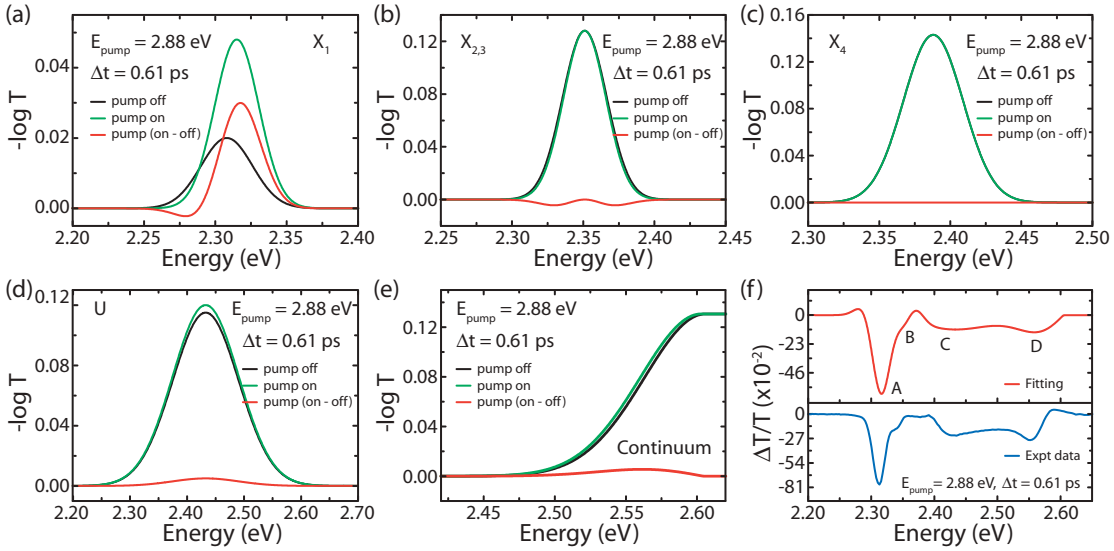

Figure 5.14: Possible individual contribution to the TA spectra from (a) X_1, (b) $X_{2,3}$, (c) X_4, (d) U and (e) continuum. The same fitting procedure as presented in Fig. 5.12(c) has been processed for the absorption spectra acquired by the broadband probe without pump (black curves) and 0.61 ps after the pump excitation (green curves). The pump-induced changes in absorption (red curves) are plotted by taking the difference between the green and black curves. The total pump-induced change obtained by summing up all the individual components in panels (a)-(e) is shown in (f) (red curve, upper panel) and compared with the experimental spectrum (blue curve, lower panel). The fitting can reproduce four main features A, B, C, D in experiment.

In order to get more insight on the TA spectra, we apply the same fitting procedure as presented in Fig. 5.12 for the absorption spectra taken without pump and with pump. A representative TA spectrum acquired at the delay time 0.61 ps is chosen. Figure 5.14 shows the individual contribution from the excitons and continuum band to the TA spectrum. Each component in the case of the pump-off (black curves), pump-on (green curves) and their spectral difference (red curves) is accordingly plotted in panel (a)-(e). The most pronounced pump-induced absorption change arises around the energy of X_1 as shown in panel (a). Without the prior excitation, the X_1 resonance appears at $\sim$2.307 eV.

Under the non-resonant excitation, the absorption feature shifts, for example, to ∼2.315 eV at 0.61 ps after the pump pulse. Furthermore, the oscillator strength becomes stronger, while the resonance width is slightly narrower by ∼3 meV. The blueshift together with the enhanced absorption results in the strong PIA feature peaked at ∼2.33 eV. On the other hand, $X_{2,3}$ (panel (b)) shows a slightly narrowing linewidth due to the pump, leading to two PIB features on two sides of the exciton energy. The feature X_4 (panel (c)) does not exhibit a visible change, while U (panel (d)) has slightly gained absorption that is responsible for the PIA feature C. The continuum bandedge (panel (e)) shifts to the low-energy side by ∼3 meV, leading to the PIA near the bandedge region. The total change is obtained in panel (f) (red curve), which is in good agreement with the experimental spectrum (blue curve). Four main features A, B, C, D are reproduced. Particularly, A is mainly contributed by the change on X_1 energy, while B is resulted from the superposition of the small bleaching on $X_{2,3}$ and the PIA on X_1. Feature C arises from the enhanced absorption in U, while the bandgap energy shift causes the PIA feature D.

The complicated exciton structures of 2D perovskites suggest that several factors may cause the pump-induced absorption in the TA spectra. In the following section, we will discuss different effects, such as the band-filling effects, exciton-exciton interaction, bandgap renormalization and the formation of new states.

5.4.3 Origins of the TA Features

(a) Burstein-Moss Band-Filling Model

The blueshift of the bandgap energies upon light excitation was first observed in doped InSb samples. The anomalous shift was explained independently by Burstein and Moss [32, 33] that has been further considered as a light- (also electro- and chemically) induced dynamic process in intrinsic semiconductors [34–36]. Upon above-bandgap excitation, electrons and holes are generated in conduction and valence bands. The carriers undergo coherent and nonthermal process, then scatter with phonons and thermalize near the bandedges. As a result of Pauli exclusion principle, these bandedge states cannot host more carriers and the followed probe beam excites carriers to higher-energy states. Therefore, in transient absorption, the Burstein-Moss band-filling model gives rise to the blueshift of the optical transitions, which scales with the carrier density.

(b) Exciton-exciton interactions

In semiconductors, the attractive and repulsive interactions between excitons cause energy shifts from its original position. In a simple picture, the exciton-exciton interactions can be qualitatively described by the Lennard-Jones potential [37, 38]:

$$\Delta E = C\left[\left(\frac{r_0}{r_s}\right)^a - \left(\frac{r_0}{r_s}\right)^b\right], \tag{5.2}$$

where C is the scaling parameter, r_s is the distance between excitons, r_0 is the interexciton distance to minimize ΔE. The exponents a and b equal to 12 and 6, respectively in the atomic case but may vary in the exciton case [39]. In Eq. (5.2), the positive term r_s^{-a} describes the repulsive force due to Pauli exclusion, which causes a blueshift of the resonance. On the other hand, the negative term r_s^{-b} is the van der Waals attractive interaction leading to a redshift of the exciton energy.

In most of the cases, a is larger than b, leading to the domination of the repulsive force in the short range, and the attractive force dominates in the long range. In analogy, when the exciton concentration is high, the shorter interparticle distance gives rise to the blueshifted spectra. Whereas, at the lower density regime, the redshift is observed instead.

(c) Bandgap renormalization

The energy shift of the exciton resonance can be also caused by the bandgap renormalization. By spin-exchange interaction, the Pauli exclusion principle does not allow the electrons with identical spins to occupy the same state. Furthermore, the Coulomb repulsive force between the carriers carrying the same charge further enhances the interparticle distance. As a result, the bandgap energy decreases. On the other hand, the existing carriers in the system can screen the Coulomb interaction between electrons and holes. If the bandgap renormalization is larger than the binding energy screening, the exciton energy will shift to the low-energy side. The energy renormalization of the bandgap and the screening effects are sensitive to the carrier density.

(d) Formation of new state

In addition to the pump-induced changes, the pump can induce the formation of new multiplex particles such as trions and biexcitons, which are sensitive to the carrier density.

At the energy of the new states, the absorption is enhanced that in turn, results in the enhanced absorption feature.

In our case, mechanism (a), (b) and (d) may lead to the changes in the absorption at X_1 and $X_{2,3}$ energy, while the PIA feature D is most likely caused by (c). Due to the unclear origin of U, the enhanced absorption at this energy and the associated PIA feature C need further investigation.

5.4.4 Carrier Dynamics

(a) Transient Absorption

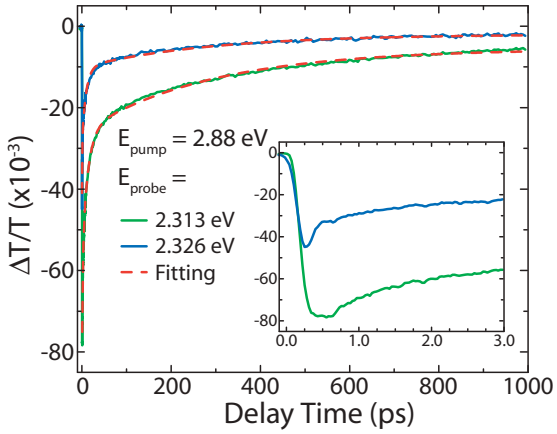

Figure 5.15: Dynamics of the PIA extracted at feature A detected at E_{probe} = 2.313 eV (green solid line) and feature B detected at E_{probe} = 2.326 eV (blue solid line). Each dynamic curve is fitted by three exponential components shown by the red dashed lines. Inset: zoom-in view of the decay curves at early time.

Figure 5.15 shows the dynamics extracted at E_{probe} = 2.313 eV (green solid line) for the dynamic of X_1, and at E_{probe} = 2.326 eV (blue solid line) for the dynamic of the change on $X_{2,3}$. The latter energy is chosen because the drop between A and B features in the TA spectrum (see Fig. 5.14(f)) is caused by the bleach in $X_{2,3}$. Therefore, the whole structure including A and B is built by the superposition of the PIA on X_1 and the PIB on $X_{2,3}$. Overall, the dynamics at 2.313 eV and 2.326 eV are similar at long delay time, whereas, the zoom-in view in early time (inset) shows an additional fast decay component of the high-energy feature in the first picosecond, which corresponds to the growing time of the low-energy one.

Each decay is well fitted with a triple-exponential function: $\Delta T/T = y_0 + A_1 e^{-t/\tau_1} + A_2 e^{-t/\tau_2} + A_3 e^{-t/\tau_3}$, where y_0 is the background value, τ_1, τ_2, τ_3 are the time constants of the decay channels and A_1, A_2, A_3 are the amplitude of each decays. The fitting

Table 5.2: Fitting parameters for the TA decay in Fig. 5.15.

	E_A = 2.313 eV	E_B = 2.326 eV
τ_1 (ps)	2.0 ± 0.2	0.5 ± 0.1
A_1	-0.027 ± 0.001	-0.020 ± 0.001
τ_2 (ps)	13 ± 1	9 ± 1
A_2	-0.031 ± 0.005	-0.019 ± 0.003
τ_3 (ps)	288 ± 30	288 ± 30
A_3	-0.020 ± 0.003	-0.008 ± 0.001

parameters are shown in Table 5.2. The overall fittings are shown by the red dashed lines. As seen from the table, the first decay time of E_B is 0.5 ps, which is comparable to the growing time of the feature E_A (see inset Fig. 5.15). After the first rapid decay, B decays with relatively similar trace as A with $\tau_{2,B}$ lies within the range of $\tau_{1,A}$ and $\tau_{2,A}$, while τ_3 are the same for both energies. The similarity of the dynamics at long-time scale suggests that $\tau_{2,B}$ and $\tau_{3,B}$ are caused by the population decay in X_1 while τ_1 is attributed to the carrier relaxation from the high-energy $X_{2,3}$ to the low-energy exciton X_1 band.

(b) Time-resolved PL

Figure 5.16 presents the background-subtracted photoluminescence decay of the 2D perovskite sample (blue solid line) upon a non-resonant excitation $E_{\text{pump}} = 3.1$ eV. Three exponential decay components are used to reproduce the decay behaviour of the PL. The overall fitting is shown by the green dashed line and the fitting parameters are given in the inset table. The assignment of the time constants is made based on the contribution of each emissive channel to the PL (see Fig. 5.3) and time-resolved PL spectra (see Fig. 5.16). The most pronounced feature contributing ∼90.3% to the total PL, originates from the recombination of the brightest excitons X_2 and X_3. A weaker feature, which contributes ∼9.2% to the PL decay, can be assigned to X_1. The modest residual ∼0.5% likely arises from the weakly emitting exciton X_4. The fast PL decays of all the radiative recombination channels support for the bright nature of the excitons. Furthermore, the faster decay of X_2 and X_3 as compared to X_1 suggests the larger oscillator strengths of X_2 and X_3 as compared to that of X_1.

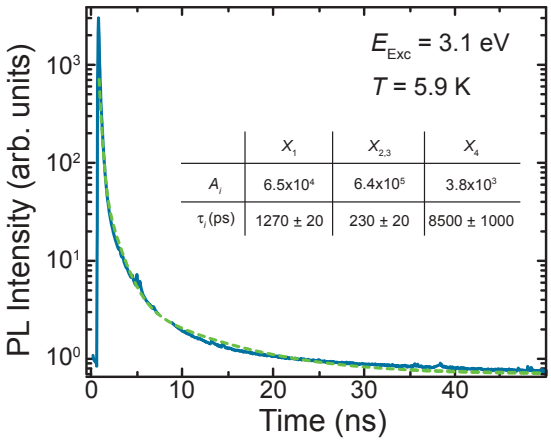

Figure 5.16: Time-resolved PL decay of 2D perovskite nanostructures (blue solid line) measured at T = 5.9 K under the excitation energy of 3.1 eV. The PL decay is fitted by three exponential components (green dashed line) corresponding to the constituent emission channels in the PL spectrum.

5.5 Conclusion

In conclusion, we elucidated the decisive role of the Coulomb electron-hole exchange interaction on the anisotropic exciton transitions of two-dimensional lead-halide perovskite semiconductors. Simultaneously, the strong electron-hole exchange coupling is quenched in isotropic spin-polarized bands by the interplay of other factors, such as internal electric-field and Rashba effects. The striking Coulomb interaction in two-dimensional perovskite, which can be practically manipulated, and the exciton fine-structure highlighted here, offer unique opportunities for the understanding of these unconventional spin-interacting processes in atomically-thin semiconductors. Furthermore, the stability of high-order exciton complexes (*e.g.* biexcitons) and their fine-structure are also expected, due to the large exciton binding energies that opens a new research direction along many-body physics. Establishing a complete understanding on the electronic band structure will be a challenging topic for the future of perovskite materials, and will shed light on the strong light-matter interactions in atomically-thin semiconductors for novel device applications.

References

1. Ishihara, T., Takahashi, J. & Goto, T. Optical properties due to electronic transitions in two-dimensional semiconductors $(C_nH_{2n+1}NH_3)_2$ PbI_4. *Phys. Rev. B* **42,** 11099 (1990).

2. Hong, X., Ishihara, T. & Nurmikko, A. Dielectric confinement effect on excitons in PbI_4-based layered semiconductors. *Phys. Rev. B* **45,** 6961 (1992).

3. Blancon, J.-C. *et al.* Scaling law for excitons in 2D perovskite quantum wells. *Nat. Commun.* **9,** 2254 (2018).

4. Ha, S.-T., Shen, C., Zhang, J. & Xiong, Q. Laser cooling of organic–inorganic lead halide perovskites. *Nat. Photonics* **10,** 115 (2016).

5. Novoselov, K. S., Geim, A. K., Morozov, S. V., Jiang, D., Zhang, Y., Dubonos, S. V., Grigorieva, I. V. & Firsov, A. A. Electric field effect in atomically thin carbon films. *Science* **306,** 666–669 (2004).

6. Deveaud, B., Clérot, F., Roy, N., Satzke, K., Sermage, B. & Katzer, D. Enhanced radiative recombination of free excitons in GaAs quantum wells. *Phys. Rev. Lett.* **67,** 2355 (1991).

7. Gallart, M., Ziegler, M., Crégut, O., Feltin, E., Carlin, J.-F., Butté, R., Grandjean, N., Hönerlage, B. & Gilliot, P. Determining the nature of excitonic dephasing in high-quality GaN/AlGaN quantum wells through time-resolved and spectrally resolved four-wave mixing spectroscopy. *Phys. Rev. B* **96,** 041303 (2017).

8. Wang, X., Jones, A. M., Seyler, K. L., Tran, V., Jia, Y., Zhao, H., Wang, H., Yang, L., Xu, X. & Xia, F. Highly anisotropic and robust excitons in monolayer black phosphorus. *Nat. Nanotech.* **10,** 517 (2015).

9. Arora, A. *et al.* Highly anisotropic in-plane excitons in atomically thin and bulklike 1 T'-ReSe2. *Nano Lett.* **17,** 3202–3207 (2017).

10. Song, Y., Hu, S., Lin, M.-L., Gan, X., Tan, P.-H. & Zhao, J. Extraordinary second harmonic generation in ReS_2 atomic crystals. *ACS Photonics* **5,** 3485–3491 (2018).

11. Andreani, L. C. & Bassani, F. Exchange interaction and polariton effects in quantum-well excitons. *Phys. Rev. B* **41,** 7536 (1990).

12. Htoon, H., Crooker, S., Furis, M., Jeong, S., Efros, A. L. & Klimov, V. Anomalous circular polarization of photoluminescence spectra of individual CdSe nanocrystals in an applied magnetic field. *Phys. Rev. Lett.* **102,** 017402 (2009).

13. Granados del Aguila, A., Liu, S., Do, T. T. H., Lai, Z., Tran, T. H., Krupp, S. R., Gong, Z.-R., Zhang, H., Yao, W. & Xiong, Q. Linearly Polarized Luminescence of Atomically Thin MoS2 Semiconductor Nanocrystals. *ACS nano* **13,** 13006–13014 (2019).

14. Becker, M. A., Vaxenburg, R., Nedelcu, G., Sercel, P. C., Shabaev, A., Mehl, M. J., Michopoulos, J. G., Lambrakos, S. G., Bernstein, N., Lyons, J. L., *et al.* Bright triplet excitons in caesium lead halide perovskites. *Nature* **553,** 189 (2018).

15. Yin, C. *et al.* Bright-exciton fine-structure splittings in single perovskite nanocrystals. *Phys. Rev. Lett.* **119,** 026401 (2017).

16. Furis, M., Htoon, H., Petruska, M., Klimov, V. I., Barrick, T. & Crooker, S. Bright-exciton fine structure and anisotropic exchange in CdSe nanocrystal quantum dots. *Phys. Rev. B* **73,** 241313 (2006).

17. Kataoka, T., Kondo, T., Ito, R., Sasaki, S., Uchida, K. & Miura, N. Magneto-optical study on excitonic spectra in $(C_6H_{13}NH_3)_2PbI_4$. *Phys. Rev. B* **47,** 2010 (1993).

18. Tanaka, K., Takahashi, T., Kondo, T., Umeda, K., Ema, K., Umebayashi, T., Asai, K., Uchida, K. & Miura, N. Electronic and excitonic structures of inorganic–organic perovskite-type quantum-well crystal $(C_4H_9NH_3)_2PbBr_4$. *Jpn. J. Appl. Phys.* **44,** 5923 (2005).

19. Galkowski, K. *et al.* Determination of the exciton binding energy and effective masses for methylammonium and formamidinium lead tri-halide perovskite semiconductors. *Energy Environ. Sci.* **9,** 962–970 (2016).

20. Takagi, H., Kunugita, H. & Ema, K. Influence of the image charge effect on excitonic energy structure in organic-inorganic multiple quantum well crystals. *Phys. Rev. B* **87,** 125421 (2013).

21. Granados del Águila, A., Groeneveld, E., Maan, J. C., de Mello Donegá, C. & Christianen, P. C. M. Effect of electron-hole overlap and exchange interaction on exciton radiative lifetimes of CdTe/CdSe heteronanocrystals. *ACS Nano* **10,** 4102–4110 (2016).

22. Yu, H., Liu, G.-B., Gong, P., Xu, X. & Yao, W. Dirac cones and Dirac saddle points of bright excitons in monolayer transition metal dichalcogenides. *Nat. Commun.* **5,** 3876 (2014).

23. Dery, H. & Song, Y. Polarization analysis of excitons in monolayer and bilayer transition-metal dichalcogenides. *Phys. Rev. B* **92,** 125431 (12 2015).

24. Niesner, D., Wilhelm, M., Levchuk, I., Osvet, A., Shrestha, S., Batentschuk, M., Brabec, C. & Fauster, T. Giant Rashba splitting in $CH_3NH_3PbBr_3$ organic-inorganic perovskite. *Phys. Rev. Lett.* **117,** 126401 (2016).

25. Price, M. B., Butkus, J., Jellicoe, T. C., Sadhanala, A., Briane, A., Halpert, J. E., Broch, K., Hodgkiss, J. M., Friend, R. H. & Deschler, F. Hot-carrier cooling and photoinduced refractive index changes in organic–inorganic lead halide perovskites. *Nat. Commun.* **6,** 8420 (2015).

26. Yang, Y., Ostrowski, D. P., France, R. M., Zhu, K., Van De Lagemaat, J., Luther, J. M. & Beard, M. C. Observation of a hot-phonon bottleneck in lead-iodide perovskites. *Nat. Photonics* **10,** 53 (2016).

27. Yuan, M., Quan, L. N., Comin, R., Walters, G., Sabatini, R., Voznyy, O., Hoogland, S., Zhao, Y., Beauregard, E. M., Kanjanaboos, P., *et al.* Perovskite energy funnels for efficient light-emitting diodes. *Nat. Nanotech.* **11,** 872 (2016).

28. Abdel-Baki, K., Boitier, F., Diab, H., Lanty, G., Jemli, K., Lédée, F., Garrot, D., Deleporte, E. & Lauret, J. Exciton dynamics and non-linearities in two-dimensional hybrid organic perovskites. *J. Appl. Phys.* **119,** 064301 (2016).

29. Liu, J., Leng, J., Wu, K., Zhang, J. & Jin, S. Observation of internal photoinduced electron and hole separation in hybrid two-dimentional perovskite films. *J. Am. Chem. Soc.* **139,** 1432–1435 (2017).

30. Yang, Y., Wu, K., Shabaev, A., Efros, A. L., Lian, T. & Beard, M. C. Direct observation of photoexcited hole localization in CdSe nanorods. *ACS Energy Lett.* **1,** 76–81 (2016).

31. Morgan, D. P., Maddux, C. J. & Kelley, D. F. Transient absorption spectroscopy of CdSe nanoplatelets. *J. Phys. Chem. C* **122,** 23772–23779 (2018).

32. Burstein, E. Anomalous optical absorption limit in InSb. *Phys. Rev.* **93,** 632 (1954).

33. Moss, T. The interpretation of the properties of indium antimonide. *Proc. Phys. Soc. B* **67,** 775 (1954).

34. Kamat, P. V., Dimitrijevic, N. M. & Nozik, A. Dynamic Burstein-Moss shift in semiconductor colloids. *J. Phys. Chem.* **93,** 2873–2875 (1989).

35. Kawamura, K.-i., Maekawa, K., Yanagi, H., Hirano, M. & Hosono, H. Observation of carrier dynamics in CdO thin films by excitation with femtosecond laser pulse. *Thin Solid Films* **445,** 182–185 (2003).

36. Hickey, S. G., Riley, D. J. & Tull, E. J. Photoelectrochemical studies of CdS nanoparticle modified electrodes: Absorption and photocurrent investigations. *J. Phys. Chem. B* **104,** 7623–7626 (2000).

37. Jones, J. E. On the determination of molecular fields. II. From the equation of state of a gas. *Proc. R. Soc. London. Ser. A, Containing Papers of a Mathematical and Physical Character* **106,** 463–477 (1924).

38. Lennard-Jones, J. E. Cohesion. *Proc. Phys. Soc.* **43,** 461 (1931).

39. Sie, E. J., Steinhoff, A., Gies, C., Lui, C. H., Ma, Q., Rosner, M., Schönhofff, G., Jahnke, F., Wehling, T. O., Lee, Y.-H., *et al.* Observation of exciton redshift–blueshift crossover in monolayer WS_2. *Nano Lett.* **17,** 4210–4216 (2017).

Chapter 6

Phonon-Assisted Exciton Transitions in Lead Halide Perovskite Nanocrystals

In semiconductor nanocrystals, a high-energy photon can create an electron and a hole, which are confined in a nanoscale volume. The photo-generated carriers relax to the band extrema then form an exciton, whose recombination gives rise to the photoluminescence emission (see Fig. 6.1(a)). In contrast, a low-energy excitation can also induce exciton transitions, leading to the light emission at the higher energy than the excitation (see Fig. 6.1(b) and (c)). In this so-called upconversion photoluminescence (UCPL) process, an photon excitation ($\hbar\omega_{\mathrm{Exc}}$) couples to an intermediate (real or virtual) state and eventually produces fluorescence at higher energy ($\hbar\omega_{\mathrm{Det}}$) from the real electronic level $|X\rangle$, after acquiring an additional energy of $-\Delta E = \hbar\omega_{\mathrm{Det}} - \hbar\omega_{\mathrm{Exc}}$. In order to enable upconversion photoluminescence (UCPL), the additional energy $-\Delta E$ needs to be provided from the absorption of either internal (phonon) energy of the medium (see Fig. 6.1(b)) or multiple photons (see Fig. 6.1(c)). Due to several absorption events, the UCPL process occurs with much lower efficiency than the PL emission [1, 2].

Light upconversion has been successfully demonstrated in several systems, such as rare-earth-doped materials [3–6], organic dyes [7–9], carbon nanotubes [10], II-VI nanobelts [11, 12], colloidal semiconductors nanocrystals (NCs) [13–17] and recently lead halide perovskites [18], for variety of applications such as biomedical imaging, frequency upconverted lasing, efficient photovoltaics and optical refrigeration. Besides the apparent conceptual simplicity, to date, the understanding of how and how much thermal energy in a solid can be exploited for upconverting light, remains elusive. This chapter presents a systematic study on the upconversion photoluminescence properties of a set of all-inorganic $CsPbX_3$ (X = I, Br, Cl, I:Br and Br:Cl) perovskite semiconductor colloidal nanocrystals. The maximum energy gain in phonon-assisted UCPL is evaluated

and discussed based on dynamical models.

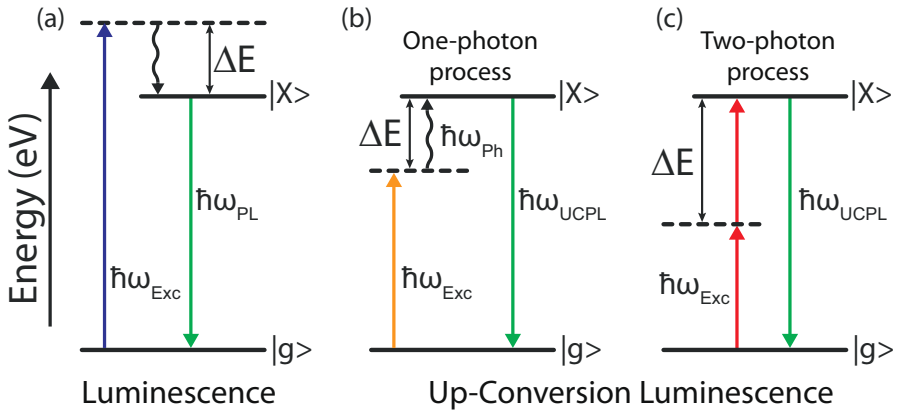

Figure 6.1: Several mechanisms behind luminescence in semiconductor colloidal perovskite nanocrystals: (a) Photoluminescence: A photon energy of $\hbar\omega_{\mathrm{Exc}}$ (blue solid arrow) is absorbed by the NC to create an electron-hole pair. After relaxation to the lowest-energy level $|X\rangle$, the exciton radiatively recombine yielding a photon with energy of $\hbar\omega_{\mathrm{PL}} \leq \hbar\omega_{\mathrm{Exc}}$ (green solid arrow). ΔE is the energy difference between the absorbed and emitted photon, defined as $\Delta E = \hbar\omega_{\mathrm{Exc}} - \hbar\omega_{\mathrm{PL}}$. Excess of energy is normally released to lattice in the form of heat (wavy arrow). Upconversion photoluminescence occurs when $\hbar\omega_{\mathrm{Exc}} < \hbar\omega_{\mathrm{UCPL}}$ by either (b) absorption of one-photon (orange arrow) and subsequent phonon energy (wavy arrow) of the NC or (c) absorption of two (or multiple) photons (red solid arrows) via an intermediate state.

6.1 Sample Preparation and Characterization

6.1.1 Sample Preparation

$CsPbA_3$ NCs were synthesized by following previous reports [19, 20]. The details are provided below.

Preparation of Cs-oleate: Cs_2CO_3 (0.407 g) was put into octadecene (ODE, 20 mL) and oleic acid (OA, 1.25 mL). This mixture was dried for 1 hour at 110°C under N_2 flowing, then heated to 150°C until Cs_2CO_3 entirely reacted with OA to form transparent solution. Since Cs-oleate precipitates out of ODE at room-temperature, it has to be pre-heated to 100°C before injection.

Synthesis of $CsPbA_3$ NCs: ODE (5 mL), oleylamine (OLA, 0.5 mL), OA (0.5 mL) and PbA_2 (0.188 mmol) were put into 25 mL flask and dried under N_2 flowing for 1 hour at 110°C. After the complete dissolution of PbA_2, the temperature was raised to 160°C and the above Cs-oleate solution (0.4 mL) was quickly injected and, 5s later, the reaction mixture was cooled by a water bath. For $CsPbBr_xCl_{3-x}$, trioctylphosphine (TOP, 0.2

mL) were added to dissolve PbA_2. The synthesized $CsPbA_3$ NCs were precipitated by adding 20 mL methyl acetate (MeAc), then centrifuged at 14000 RPM for 5 min. The depositing product was redispersed in 5 mL hexane and precipitated again with 5 mL MeAc and centrifuged at 14000 RPM for 5 min. Then, the QDs were dispersed in 2 mL of hexane. The solution of $CsPbA_3$ NCs was kept in the refrigerator at 4°C for 48 hours to precipitate excess of Cs-oleate and Pb-oleate. The NC solution was diluted and centrifuged again at 14000 RPM for 2 min before use.

6.1.2 Sample Characterization

$CsPbX_3$ NCs were intensively characterized by transmission electron microscopy (TEM) and optical spectroscopy. Most of the synthesized $CsPbX_3$ nanostructures have cubic-like shape. Typical lateral sizes (L) are approximately $L \approx 10$ nm and surface areas are $S = L \times L \approx 100$ nm^2, as can be seen in Fig. 6.2(b) for $CsPbI_3$ with $L = (8.4 \pm 1.7)$ nm and Fig. 6.2(c) for $CsPbBr_3$ with $L = (9.9 \pm 2.3)$ nm. The diffraction planes are clearly observed in the high-resolution TEM image (see Fig. 6.2(d)) indicative of the high crystallinity. The $CsPbX_3$ NCs ensemble samples were prepared by solution spin-coating on cleaned SiO_2/Si substrates for the optical experiments. Each sample was investigated by steady-state photoluminescence and upconversion photoluminescence excitation experiments by varying photon energy, excitation power and temperature.

6.2 Linear Optical Properties

6.2.1 Optical Characterization

The $CsPbX_3$ NCs were first characterized by linear absorption, steady-state and time-resolved photoluminescence experiments. Figure 6.3 shows normalized PL spectra at room temperature (T = 296 K) for perovskite NCs with different compositions. PL emission of iodide-based NCs (red solid curve) takes place in the red region of the electromagnetic spectrum ($\sim$1.8 eV). The PL spectral position shifts to $\sim$2.4 eV and to $\sim$3.1 eV when using Br (green solid curve) or Cl (violet solid curve) atoms, respectively. The emission energy can be further manipulated, not only by varying the NC size [19], but also by alloying the halide-elements to cover the entire visible region. For instance, the mixture I:Br leads to the orange spectrum centred at $\sim$2.2 eV, while Br:Cl results in the light-blue and dark-blue spectra located at $\sim$2.6 eV and $\sim$2.7 eV, respectively. The

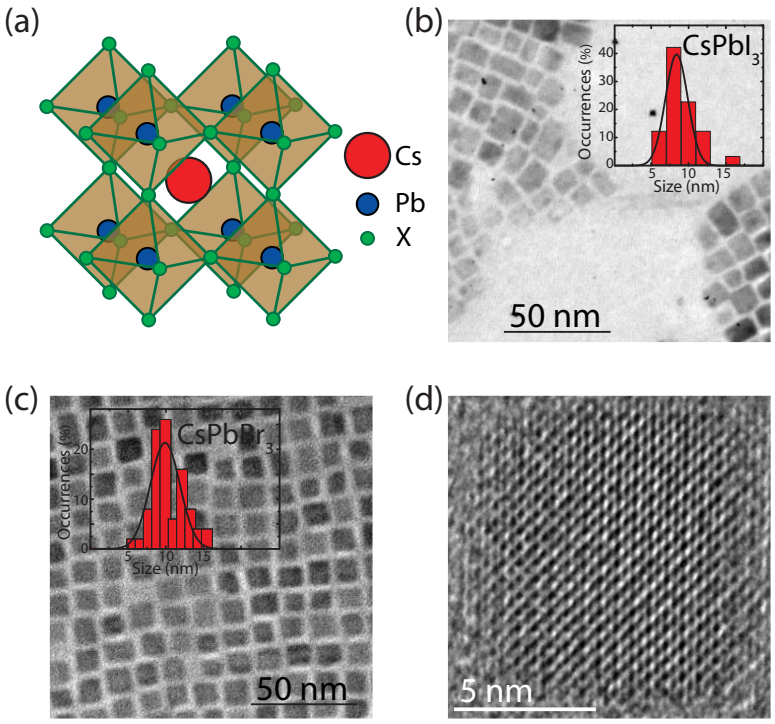

Figure 6.2: (a) Illustration for the perovskite crystal structure. Representative TEM images for (b) $CsPbI_3$ and (c) $CsPbBr_3$ NCs, showing the cubic-like shape with average lateral side of $\langle L \rangle = (8.4 \pm 1.7)$ nm and (9.9 ± 2.3), respectively (inset). Corresponding size histograms are shown in the insets. (d) High-resolution TEM image showing diffraction planes of the $CsPbBr_3$ NCs.

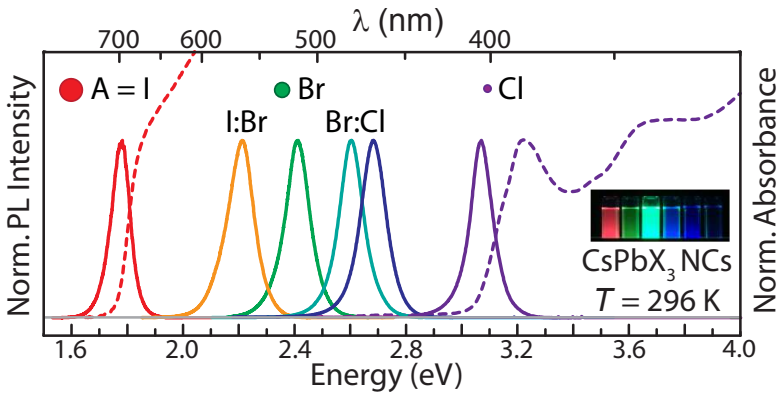

Figure 6.3: Normalized PL spectra taken at room temperature (T = 296 K) of $CsPbI_3$ ($\hbar\omega_{\mathrm{Exc}}$ = 1.96 eV, red solid line), $CsPbI_{1.5}Br_{1.5}$ ($\hbar\omega_{\mathrm{Exc}}$ = 2.71 eV, orange solid line), $CsPbBr_3$ ($\hbar\omega_{\mathrm{Exc}}$ = 2.71 eV, green solid line), $CsPbBr_2Cl$ ($\hbar\omega_{\mathrm{Exc}}$ = 3.81 eV, light-blue solid line), $CsPbBr_{1.5}Cl_{1.5}$ ($\hbar\omega_{\mathrm{Exc}}$ = 3.81 eV, dark-blue solid line) and $CsPbCl_3$ ($\hbar\omega_{\mathrm{Exc}}$ = 3.81 eV, violet solid line). The luminescence spectral position shifts to high energies with decreasing size of the halide atom. Normalized linear absorption spectra taken at T = 296 K are given for $CsPbI_3$ (red dashed line) and $CsPbCl_3$ (violet dashed line). The inset shows an optical image of the perovskite NC solutions under illumination of UV light.

exact energy position for the alloyed NCs depends on the precise stoichiometric ratio of the halogen elements. The relatively narrow PL linewidths of 80-100 meV for $CsPbX_3$ NCs are comparable to those reported for perovskite NCs [19, 21–24] and traditional II-VI quantum dots [25–27].

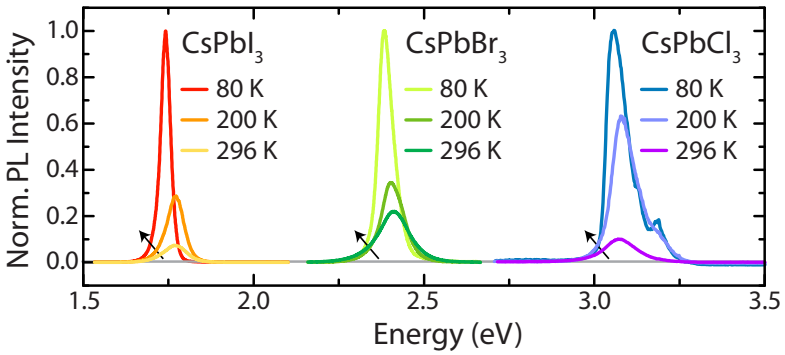

Figure 6.4: Temperature-dependent photoluminescence spectra of $CsPbX_3$ NCs under non-resonant excitation condition. With increasing temperature, the PL spectra shifts to the high-energy side, while the linewidth gets broader and the intensity drops significantly.

Figure 6.4 shows the temperature-dependent PL spectra of the $CsPbX_3$ NCs acquired at selected temperatures and under non-resonant excitation. Overall, as increasing temperature, the PL spectra show a blueshift that is the typical temperature effects on the bandgap of perovskites materials. Furthermore, the PL intensity decreases dramatically at high temperature as a result of the reduced quantum efficiency and the linewidth gets broader due to the enhanced carrier-phonon scattering processes.

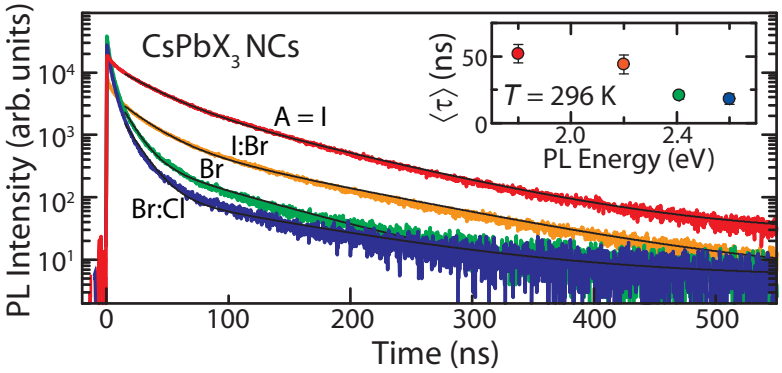

Figure 6.5: Room-temperature PL decay curves under 3.1 eV photo-excitation for $CsPbX_3$ NCs on a semi-logarithmic scale. The time-resolved spectra are labelled by the corresponding constituent halogen atoms. The black solid lines are biexponential fitting curves. Inset: Average PL decay time $\langle\tau\rangle$ is shown for the investigated NCs as a function of the emission energy.

Figure 6.5 shows room-temperature PL decay curves for different all-inorganic $CsPbI_3$

Table 6.1: PL lifetimes τ_1, τ_2 and intensity averaged $\langle\tau\rangle$ for caesium lead halide perovskite NCs. The corresponding decay amplitudes (A_i) and the intensity averaged PL lifetime $\langle\tau\rangle$ are also given.

	$CsPbI_3$	$CsPbI_{1.5}Br_{1.5}$	$CsPbBr_3$	$CsPbBr_2Cl$
τ_1 (ns)	26 ± 4	24 ± 5	11 ± 2	11 ± 2
A_1	5255	2137	1988	1410
τ_2 (ns)	93 ± 10	108 ± 12	75 ± 11	90 ± 20
A_2	4356	723	367	155
$\langle\tau\rangle$ (ns)	52 ± 7	44 ± 7	21 ± 3	18 ± 4

(red curve), $CsPbI_{1.5}Br_{1.5}$ (orange curve), $CsPbBr_3$ (green curve) and $CsPbBr_2Cl$ (blue solid curve) nanocrystals under 3.1 eV excitation. The time-resolved spectra shows multi-exponential behaviours as typically observed in semiconductor NCs [24, 28, 29]. In our case, we ignore the ultrafast decay at early time after the pulse excitation, which is normally contributed by non-radiative process during exciton thermalization, and we model the PL decay curves by biexponential functions (black lines). The obtained PL lifetimes τ_1 and τ_2 are listed in Table 6.1. The faster decay component τ_1 is $\sim$26 ns for $CsPbI_3$ and decreases to $\sim$11 ns for $CsPbBr_2Cl$, which are in good agreement with recent literature [19, 24]. On the other hand, the longer PL lifetime τ_2 $\sim$90 ns is roughly independent of composition, but its contribution to the total PL decay varies. Long decay time is normally attributed to forbidden (dark) transitions, originating from dark exciton recombination. Further experiments by monitoring temperature dependence or magnetic field dependence of the PL decays are required to elucidate the precise nature of these emitting channels.

An intensity-averaged decay time $\langle\tau\rangle = \sum_i A_i\tau_i / \sum_i A_i$ is shown as a function of the emission energy of each NCs (see inset to Fig. 6.5), where A_i (i = 1, 2) is the amplitude of each PL decay component i. The major contribution of the long PL decay channels (A_1, A_2) to the total light emission and the absence of low-energy and poorly emitting defect bands in the PL spectra of the NCs confirms the high quality of our samples.

6.2.2 Quantum-Confinement Effects on $CsPbX_3$ Nanocrystals

Figure 6.6 shows the PL spectra of different perovskite compositions in bulk and nanocrystal forms at T = 80 K and under non-resonant excitation. The PL linewidth measured on the NCs ($\sim$50-100 meV) is broader than that measured on the bulk crystals

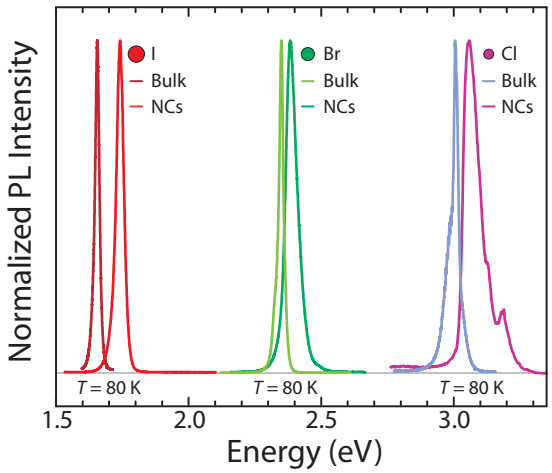

Figure 6.6: Photoluminescence spectra of the perovskites bulk and nanocrystals composed of iodide (dark-red and red lines), bromide (green and dark green lines) and chloride (light-blue and violet lines) at 80 K and under non-resonant excitation. The PL spectrum is blue-shifted when applying spatial confinement on center-of-mass motion of free excitons in the 3D structures.

(∼20 meV). The broadening in the NC PL is mostly due to the inhomogeneous broadening given by the size distribution in the NC ensemble. In addition, going from the three-dimensional bulk to zero-dimensional NCs, the PL spectrum shifts to the high-energy side by ∼91 meV for iodide-based, ∼32 meV for bromide-based and ∼53 meV for chloride-based compounds. The quantum-confinement effects depend on the NC sizes as compared to the exciton Bohr radius in the bulk structure. In our case, all of the NCs have bigger radius than the corresponding exciton Bohr radius that provides a weak quantum-confinement regime for the excitons.

6.3 Nonlinear Optical Properties

6.3.1 Photoluminescence versus Upconversion Photoluminescence

The light upconversion signals were measured on all the NC compounds. At energies well below the lowest-energy resonance, the optical absorption is negligible or tends to be zero. However, strong and stable upconversion photoluminescence signals (coloured dashed lines) are detected for all investigated $CsPbX_3$ NCs as shown in Fig. 6.7(a). The corresponding PL spectra are also shown by coloured solid lines to compare. For all the nanocrystals, both upconversion and photoluminescence spectra share similar linewidths and identical energy positions, in contrast to the observations in II-VI (*e.g.*, CdSe or

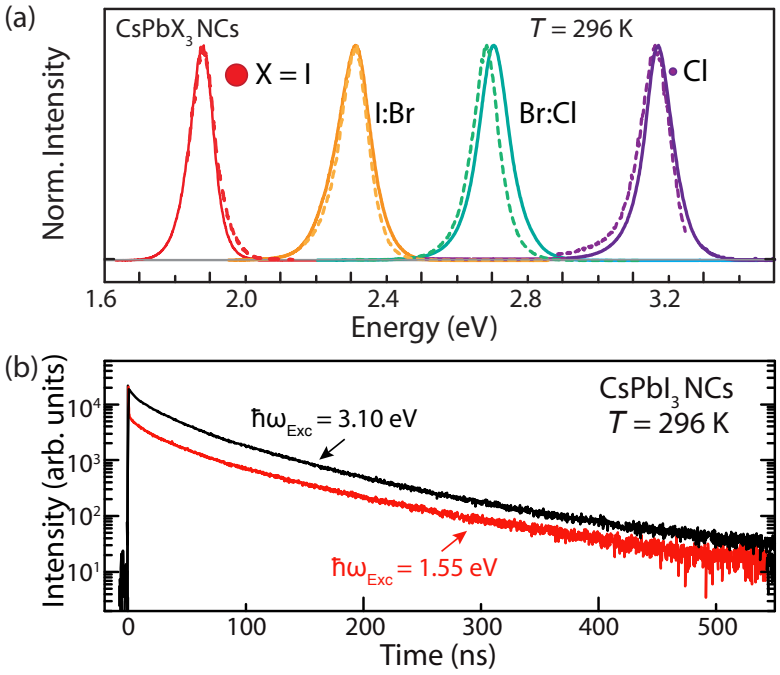

Figure 6.7: Photoluminescence versus upconversion photoluminescence spectra of the all-inorganic $CsPbX_3$ nanocrystals. (a) Comparison between normalized upconversion (dashed lines) and regular photoluminescence (solid lines) spectra taken at room temperature (T = 296 K) for $CsPbI_3$ (red curves), $CsPbI_{1.5}Br_{1.5}$ (orange curves), $CsPbBr_2Cl$ (light-blue curves) and $CsPbCl_3$ (violet curves). The spectra are labelled by the corresponding halogen atom. (b) Room temperature transient spectra for $CsPbI_3$ NCs under excitation with photon energies of 3.1 eV (red curve) and 1.55 eV (black curve), corresponding to PL and phonon-assisted UCPL decays, respectively. Similar emission energies, linewidths, decay traces and time constants are found for PL and UCPL, indicating that the luminescence signals originate from the same exciton levels.

CdTe) NCs [13, 30]. In addition, Fig. 6.7(b) shows similar traces of PL (black curve) and UCPL (red curve) decays for $CsPbI_3$ NCs. The consistence between the regular and upconverted emission properties indicates that the same subset of NCs contribute to the luminescence signal.

Figure 6.8(a) shows room-temperature linear absorption (black curve) and photoluminescence (blue curve) spectra of $CsPbBr_3$ NCs, as a representative system to discuss the photon upconversion in perovskite NCs. The PL spectrum centered at $\hbar\omega_{\mathrm{Det}} \sim 2.41$ eV is monitored while varying the excitation wavelength across the absorption spectrum (color-coded arrows). Figure 6.8(b) compares the room-temperature luminescence spectrum under 2.71 eV excitation (λ_{Exc} = 457 nm, blue curve) with upconversion spectra taken with laser energies of 2.33 eV (λ_{Exc} = 532 nm, green curve), 2.20 eV (λ_{Exc} = 564 nm, orange curve) and 1.96 eV (λ_{Exc} = 633 nm, red curve). Although the absorption

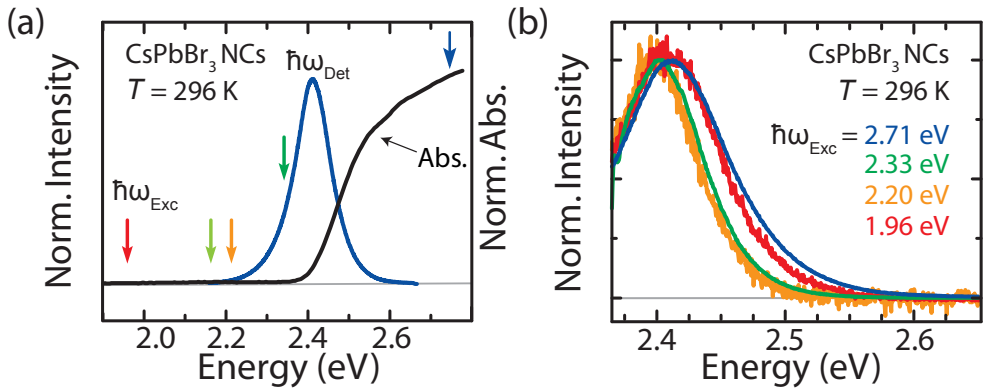

Figure 6.8: UCPL versus excitation energy. (a) Linear absorption profile of $CsPbBr_3$ NCs at T = 296 K (black curve). The color-coded arrows denote the used excitation photon energies ($\hbar\omega_{\mathrm{Exc}}$) in the upconversion experiments. $\hbar\omega_{\mathrm{Det}}$ denotes the center energy of the NC photoluminescence (blue curve). (b) Normalized room-temperature upconversion spectra of $CsPbBr_3$ NCs under illumination with photon energies of 2.71 eV (blue curve), 2.33 eV (green curve), 2.20 eV (orange curve) and 1.96 eV (red curve).

at these energies is negligible, the upconversion signal remains strong. Importantly, all the PL spectra exhibit similar peak positions and linewidths, indicating that the emission signal originates from the same electronic level. Although the upconversion emission occurs for a wide range of photon energies, the mechanism governing the UCPL phenomenon (see Fig. 6.1) depends strongly on how the nanocrystals are excited. In order to differentiate the different mechanisms for each excitation energy, the emission signal was studied as a function of power of the continuous laser excitation and temperature.

6.3.2 Multiple-Photon Absorption

Figure 6.9(a) shows typical room-temperature UCPL spectra obtained with 1.96 eV excitation. The laser power was initially P_o = 95 kWcm^{-2} and varied to a quarter of P_o leading to a nonlinear drop of the emission intensity. This behaviour suggests that more than one photon participate in the upconversion luminescence process. Keeping the same photo-excitation energy and power density while decreasing temperature from 296 K (blue curve, Fig. 6.9(b)) to 80 K (red curve), the spectrum shifts to lower energy as normally observed in these perovskite materials as discussed in Chapter 3 and in literature [31–35]. Furthermore, the UCPL intensity drops at higher temperature as a result of the lower quantum yield. The nonlinear power dependence and the increasing intensity at lower temperature indicate that multiple photons are absorbed to upconvert light.

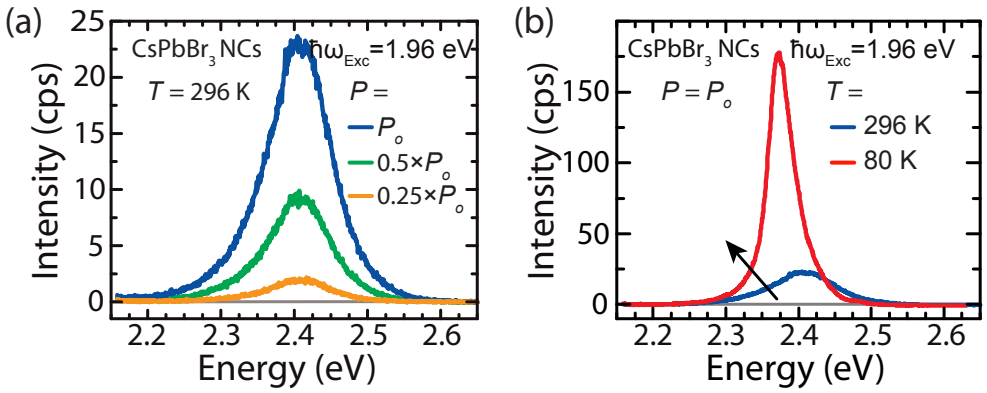

Figure 6.9: UCPL versus power and temperature of multiple-photon absorption mechanism. (a) Power-dependent upconversion spectra of $CsPbBr_3$ NCs taken at room temperature under 1.96 eV excitation photon energies. The maximum power density is P_o = 95 kWcm^{-2}. (b) Upconversion spectra under 1.96 eV photo-excitation taken at T = 80 K (red curve) and T = 296 K (blue curve) using the same power density. The upconversion intensity increases with decreasing temperature.

6.3.3 Phonon-Assisted Photoluminescence

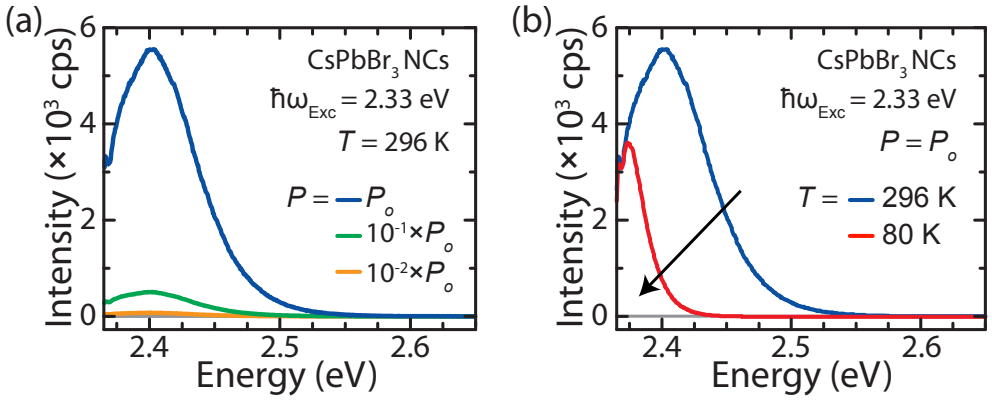

Figure 6.10: UCPL versus power and temperature of phonon-assisted PL mechanism. (a) Power-dependent upconversion spectra of $CsPbBr_3$ NCs taken at room temperature under 2.33 eV excitation photon energies. The maximum power density is P_o = 1.6 kWcm^{-2}. (b) Upconversion spectra under 2.33 eV photo-excitation taken at T = 80 K (red curve) and T = 296 K (blue curve) using the same power density. The upconversion intensity decreases with decreasing temperature.

Figure 6.10(a) shows typical room-temperature UCPL spectra obtained with 2.33 eV excitation. The laser power was initially P_o = 1.6 kWcm^{-2} and varied across two orders of magnitude, leading to a linear drop of emission intensity. This behaviour suggests that only one photon participates in the upconversion process. Keeping the same photo-excitation energy and power density while decreasing temperature from 296 K (blue

curve, Fig. 6.10(b)) to 80 K (red curve), the spectrum shifts to lower energy as normally observed in these perovskite materials [31–35]. Furthermore, the decreasing intensity at lower temperature strongly suggests the critical role of the nanocrystal thermal energy in the photon upconversion process.

6.3.4 Excitation Energy Dependence

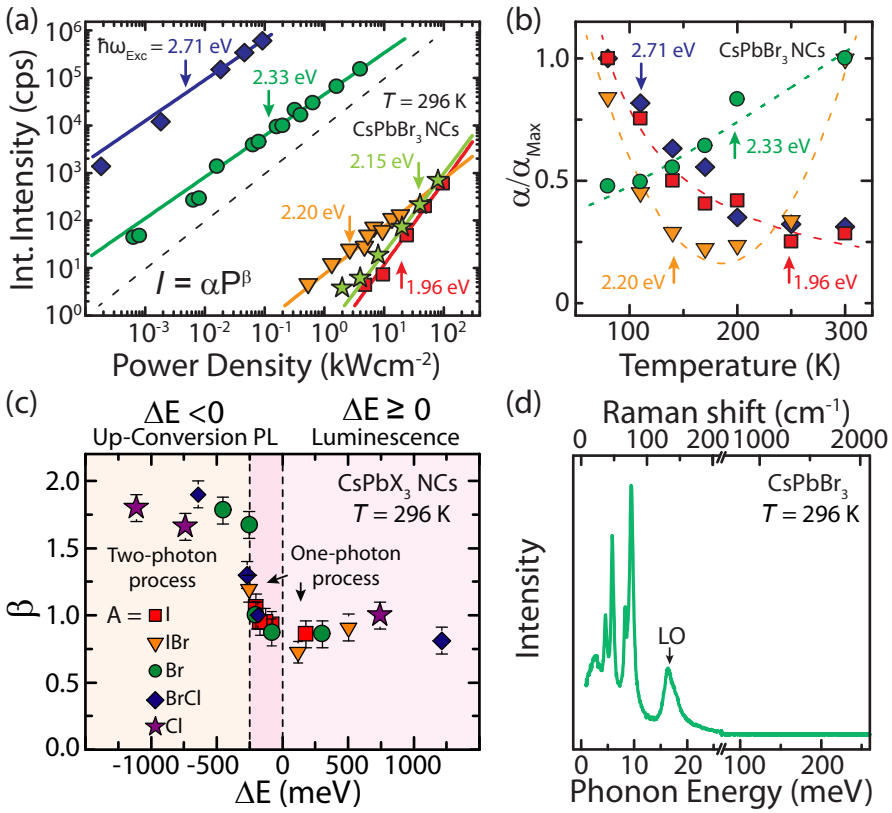

Figure 6.11: Energy gain for phonon-assisted exciton transition in $CsPbX_3$ nanocrystals. (a) Power dependence of the integrated intensity (I) after photo-excitation at 2.71 eV (blue diamonds), 2.33 eV (green circles), 2.20 eV (orange down-triangles), 2.15 eV (light-green stars) and 1.96 eV (red squares). The colored solid lines are fittings to the power law $I = \alpha P^{\beta}$. The black dashed line represents $\beta = 1$. (b) Temperature dependence of pre-factor α for the used excitation energies in (a), with the same symbol and color convention. α has been normalized to the maximum value α_{Max} of each $\hbar\omega_{\mathrm{Exc}}$ for comparison. The colored dashed lines are guidelines. (c) Extracted room-temperature β for all the investigated $CsPbX_3$ NCs as a function of ΔE. The chemical compositions are indicated by the legends. The clear switch between one- and two-photon absorption occurs at $\Delta E \sim$ -200 meV. (d) Room-temperature Raman spectrum of $CsPbBr_3$, showing the optical phonon energy (LO) of 16 meV.

The detailed power dependence of the integrated PL intensity (I) at room temperature for $CsPbBr_3$ NCs, is shown in Fig. 6.11(a) in a log-log scale for all the used laser

wavelengths. The intensity I is fitted to the power law $I = \alpha P^{\beta}$ (colored solid lines), where P is power density in the excitation area (12 μm^2). Excitation above the NC bandgap (i.e., $\hbar\omega_{\mathrm{Exc}} \geq \hbar\omega_{\mathrm{Det}} = 2.41$ eV, blue squares) (*i.e.*, photoluminescence regime), leads to a sublinear ($\beta \leq 1$) power dependence, which is typical for quantum systems [17, 36]. Below-bandgap excitation (i.e., $\hbar\omega_{\mathrm{Exc}} < \hbar\omega_{\mathrm{Det}}$) with weak or negligible linear absorption (i.e., upconversion regime), the intensity decreases drastically with decreasing excitation energy and remains sublinear till $\hbar\omega_{\mathrm{Exc}}$ = 2.20 eV. At around $\hbar\omega_{\mathrm{Exc}}$ = 2.15 eV, the intensity saturates and the slope becomes steeper, with $\beta \sim 2$. Sublinear power dependence suggests that the upconversion is governed by absorption of one-photon followed by absorbing NC thermal energy, whereas, the superlinear power dependence ($\beta \sim 2$) implies two-photon absorption process. This is further confirmed by the temperature-dependent PL at various laser energies.

Figure 6.11(b) shows the normalized pre-factor α as a function of temperature. Two distinct trends are clearly observed. For the process merely involving the absorption of photons ($\hbar\omega_{\mathrm{Exc}} = 2.71$ eV and 1.96 eV) by either one- (blue diamonds) or two-photon (red squares), monotonically increases with decreasing temperature. This increment is due to the higher quantum yield at lower temperatures, as normally observed in NCs [28]. On the other hand, for the processes requiring absorption of NC thermal energy, the UCPL weakens with decreasing bath temperature (green circles). Exciting at 2.20 eV, α exhibits a dual behaviour (orange triangles) alike a temperature-induced switch of the fluorescence mechanism, which defines the room-temperature energy threshold between phonon-assisted upconversion and two-photon absorption in $CsPbBr_3$ NCs. The experimental results at room temperature are summarized in Fig. 6.11(c) for different compounds. The parameter β is depicted as a function of the energy difference ΔE. The step-like behaviour of β clearly delimits different mechanisms at room temperature, where phonon-assisted regime occurs in an energy window from 0 to 250 meV and the multiple-photon process takes place beyond 250 meV. The surprisingly large threshold of $\sim$200 meV is independent of NC compositions and surpasses that of other semiconductor NCs [13, 30, 37].

In order to understand the efficient phonon-assisted UCPL in semiconducting perovskite NCs, knowledge of the phonon spectrum is crucial. Figure 6.11(d) shows a non-resonant Raman spectrum of $CsPbBr_3$ taken at room temperature using 1.96 eV excitation. The spectrum exhibit a number of sharp features at energies below $\sim$20 meV: two set of doublets centered at $\sim$5 meV and $\sim$10 meV, and a broader structure at $\sim$16

meV. The spectral position of the Raman signals are in good agreement with experiments [38, 39] and calculations [40], from which we identified an optical phonon mode at ∼16 meV. At high-energy region of ∼200 meV, no phonon modes were detected. The lack of lattice vibrations matching with the large energy gain of $\sim 8k_BT$ reveals that multiple phonon-assisted upconversion events have to take place with high efficiency.

6.4 Electron-Phonon Interaction

We employed transient absorption (TA) spectroscopy to study the carrier relaxation in $CsPbX_3$ NCs, which provides the timescale for electron-phonon interactions. Figure 6.12(a) shows a typical TA map obtained for $CsPbBr_3$ NCs at room temperature. The used pump fluence was 35.7 μJ/cm^2, producing an average number of excited carriers per NC of $\langle N \rangle \sim 0.1$. A pronounced bleaching feature (positive $\Delta T/T$) appears at the optical bandgap (∼2.5 eV). At early delay time, the bleaching exhibits a considerable broadening in the high-energy side and gets narrower afterwards that indicates the existence of hot carrier. A pump-induced absorption (PIA) feature (negative $\Delta T/T$) at the high-energy side is assigned to the excited-state absorption, while the PIA at low-energy side arises from the exciton-exciton (biexciton) interaction.

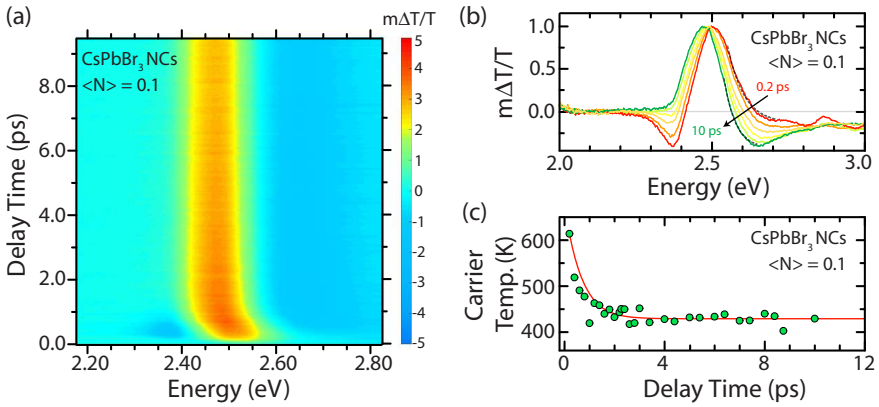

Figure 6.12: Electron-phonon coupling in $CsPbX_3$ NCs. (a) Pseudo-color ($\Delta T/T$) representation transient absorption spectra for $CsPbBr_3$ NCs using excitation energy of 3.82 eV with low pumping fluence. The average number of excited carriers per NC is $\langle N \rangle \ll 1$. The broadening at early time indicates the existence of hot carriers. (b) Normalized transient transmission spectra at selected pump-probe time delays from 0.2 ps to 10 ps (colored solid lines). The high-energy tails are fitted by Boltzmann distribution (black dashed lines). (c) Carrier temperature (blue circles) extracted from (b) as a function of delay time. The carrier cooling is modelled by Eq. (6.1), resulting an effective cooling time of $\langle \tau_{\text{cooling}} \rangle \sim 1.5$ ps.

The extracted transient transmission spectra at selected time delay from 0.2 to 10 ps are shown in Fig. 6.12(b). The high-energy tail of the bleaching feature can be well fitted by the Maxwell-Boltzmann distribution $\Delta T/T \propto \exp(-E/k_B T_c)$ (black dashed line) to obtain the effective electronic temperature T_c. The same fitting criteria are used for all the spectra resulting in the decay of carrier temperature as shown in Fig. 6.12(c). The carrier gets cooled in the first 3 ps, then T_c saturates at longer delay time. This behavior is similar for different excitation powers as long as $\langle N \rangle < 1$, while beyond that, the cooling traces become longer as a result of the phonon bottleneck effects.

In polar semiconductors as lead halide perovskites, the carrier relaxation is governed by the Fröhlich interactions between carriers and longitudinal optical (LO) phonons by elastic scattering. The stronger the interaction is, the faster the relaxation occurs. The coupling strength between carriers and LO phonon population can be quantified by [40–42]:

$$-\frac{3k_B}{2}\frac{dT_c}{dt} \approx \frac{\hbar\omega_{\mathrm{LO}}}{\langle\tau_{\mathrm{cooling}}\rangle}\left[\exp\left(-\frac{\hbar\omega_{\mathrm{LO}}}{k_B T_c}\right) - \exp\left(-\frac{\hbar\omega_{\mathrm{LO}}}{k_B T_l}\right)\right], \tag{6.1}$$

where T_l is the lattice temperature and $\hbar\omega_{\mathrm{LO}}$ is the LO phonon energy. By using parameters obtained from our experiments, T_l = 296 K and $\hbar\omega_{\mathrm{LO}}$ = 16 meV (see Fig. 6.11(d)), Eq. (6.1) can be well fitted to the cooling dynamic curve in Fig. 6.12(c), with $\langle\tau_{\mathrm{cooling}}\rangle \approx$ 1.5 ps. The cooling rate in $CsPbBr_3$ NCs is comparable to that in II-VI semiconductor NCs [43–46], which are typical systems demonstrating strong Fröhlich interaction [11, 47, 48], suggesting a strong electron-phonon coupling of perovskites.

6.5 Discussion

6.5.1 Phonon-Assisted Upconversion Dynamics

A kinetic model has been previously introduced to phenomenologically describe the upconversion luminescence dynamics [10, 30]. The model considers an energetic diagram including a ground state $|g\rangle$, an intermediate state $|I\rangle$ defined by the excitation energy and an electronic level $|X\rangle$ (see Fig. 6.13) defined by the optical bandgap of the NC. The carrier is initially pumped to level $|I\rangle$ with a generation rate G, then either elastically scatters back to $|g\rangle$ (rate Γ_V) or absorbs phonon energies to level $|X\rangle$ (rate γ_{NR}). Excitons at $|X\rangle$ can non-radiatively relax to $|I\rangle$ (rate γ_{NR}) or radiatively recombine (rate Γ_X).

In thermal equilibrium conditions, the carrier populations at $|I\rangle$ and $|X\rangle$ follow Boltzmann distribution. Hence, the transient population at each level can be described

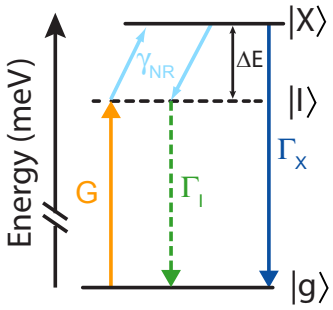

Figure 6.13: Energy diagram for UCPL dynamics. A low-energy excitation (orange arrow) excites a carrier from ground state $|g\rangle$ to an intermediate state $|I\rangle$ (rate G), which can either annihilate with a rate Γ_I or transfer to the electronic level $|X\rangle$ with a rate of γ_{NR} by absorbing phonons. Excitons at $|X\rangle$ can relax to $|I\rangle$ with a rate of γ_{NR} or radiatively recombine with a rate of Γ_X. ΔE denotes the energy difference between emission and excitation energies.

by:

$$\frac{dn_I}{dt} = G - \left[\Gamma_I + \gamma_{\mathrm{NR}} \exp\left(-\frac{\Delta E}{k_B T}\right)\right] n_I + \gamma_{\mathrm{NR}} n_X, \tag{6.2}$$

$$\frac{dn_X}{dt} = \gamma_{\mathrm{NR}} \exp\left(-\frac{\Delta E}{k_B T}\right) n_I - \gamma_{\mathrm{NR}} n_X - \Gamma_X n_X. \tag{6.3}$$

Solving Eq. (6.2) and (6.3) results in an expression for the upconversion intensity:

$$I_{\mathrm{UCPL}} = G \frac{c_1}{c_2 \exp(\Delta E / k_B T) + 1}, \tag{6.4}$$

where $c_1 = \Gamma_X/(\Gamma_X + \gamma_{\mathrm{NR}})$ and $c_2 = \Gamma_I/\gamma_{\mathrm{NR}}$.

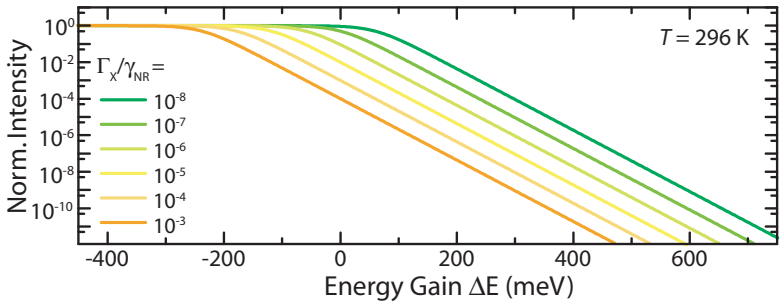

Figure 6.14: Dependence on non-radiative relaxation rate. The UCPL intensity is plotted for different relaxation rates γ_{NR}. The faster the relaxation, the stronger the upconversion and the larger the energy gain.

Figure 6.14 plots the dependence of UCPL intensity on the energy difference between the detection and excitation energies, ΔE. Different relaxation cases, represented by $\Gamma_X/\gamma_{\mathrm{NR}}$, across five orders of magnitude are considered. The kinetic model predicts

that upconversion photoluminescence occurs more efficiently with smaller $\Gamma_X/\gamma_{\rm NR}$, or equivalently, with faster electron-phonon scattering rate.

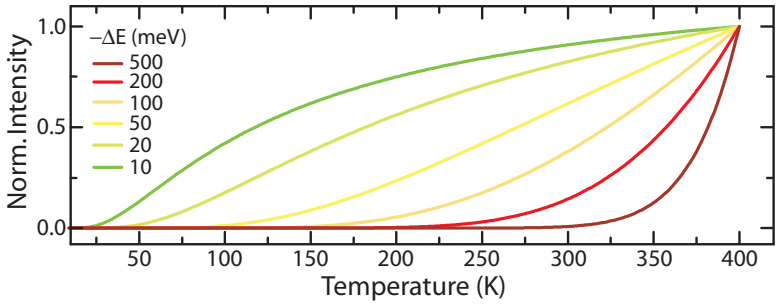

Figure 6.15: Dependence on energy gain. The UCPL intensity is plotted as a function of energy gain T while using different excitation energy, or in other words, different ΔE. The higher the temperature, the stronger the upconversion. Especially, for $-\Delta E$ = 200 meV, the temperature-dependent curve qualitatively reproduces the shape of experimental curves (see Fig. 6.11(b)).

In addition, Eq. (6.4) also predicts the temperature dependence of the UCPL intensity, as shown in Fig. 6.15 for different excitation condition. Specifically, the phonon-assisted exciton transition occurs more efficiently at higher temperature, at which the phonon population is large. Furthermore, the smaller $|\Delta E|$ is, the higher the UCPL intensity. However, a limitation of this three-level model is that it cannot evaluate the maximum thermal energy that can be converted into electromagnetic energy ($|\Delta E|_{\rm Max}$). Our statistical model is therefore proposed to solve this issue and explain for the striking energy gain for light upconversion in perovskite NCs.

6.5.2 Phonon-Assisted Energy Gain

We propose an alternative approach aiming to quantify ($|\Delta E|_{\rm Max}$). Our statistical model takes into account n consecutive absorption of phonons via n-intermediate levels separated by phonon energy $\varepsilon_{\rm ph}$ (see Fig. 6.16(a)). The intermediate levels can be either real or virtual that carry negligible oscillator strength and no light absorption.

As reflected by the PL experiments (see Fig. 6.3), we consider the material with defect-free and high quantum-efficiency. Geometrically, the modelled solid has cubic shape with lateral size L and volume $V = L^3$. A low-energy photon $\hbar\omega_{\rm Exc}$ creates a cold exciton at the level $|0\rangle$, which can either elastically scatter to the ground-state $|g\rangle$ or absorb phonons to the upper levels. At the intermediate state $|i\rangle$, there are three possible pathways: (i) non-radiatively decay to $|g\rangle$ with probability $P_i^{\rm NR}$, (ii) emit a phonon to state $|i-1\rangle$ with probability $P_i^{\rm Em}$ and (iii) absorb a phonon to $|i+1\rangle$ with probability

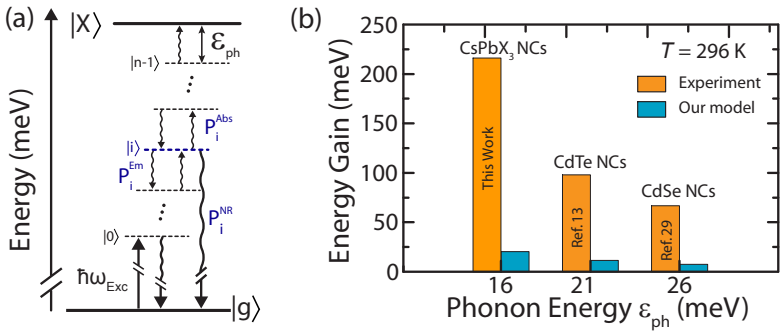

Figure 6.16: (a) Schematic of the statistical probability model, considering sequential absorption of n phonons with energy of $\varepsilon_{\rm ph}$. $P_i^{\rm Abs}$, $P_i^{\rm Em}$ and $P_i^{\rm NR}$ denote the probabilities for absorbing, emitting a phonon and non-radiative relaxation from the intermediate state i, respectively. (b) Computed maximum energy acquired from optical phonons for light upconversion in different semiconductor nanocrystals (light-blue bars) and the maximum values obtained in experiments (orange bars). The experimental values are one order of magnitude larger than the theoretical ones, suggesting the important role of acoustic phonons to the overall UCPL process.

$P_i^{\rm Abs}$. To reach the real electronic state $|X\rangle$ and then emit a high-energy photon, the probability of phonon absorption ($Q_\uparrow$) needs to outcompete with the total probability of decay to lower states ($Q_\downarrow$) that are expressed as follows:

$$Q_\uparrow = \prod_{i=0}^{n-1} P_i^{\rm Abs} = \prod_{i=0}^{n-1}(N-i)p(\varepsilon_{\rm ph};T)\gamma_{\rm e-ph}, \tag{6.5}$$

$$Q_\downarrow = \prod_{i=0}^{n-1} P_i^{\rm Em} + \prod_{i=0}^{n-1} P_i^{\rm NR} = \prod_{i=0}^{n-1}(N+1-i)(p(\varepsilon_{\rm ph};T)+1)\gamma_{\rm e-ph} + \prod_{i=0}^{n-1}\gamma_{\rm NR,i}, \tag{6.6}$$

where N is the number of available phonons estimated as $N = (a/a_o)^3$, with typical lattice constant values of $a_o \sim 0.5$ nm [49]. The term $p(\varepsilon_{\rm ph};T) = (\exp(\varepsilon_{\rm ph}/k_BT)+1)^{-1}$ is the Bose-Einstein distribution, $\gamma_{\rm e-ph}$ is the electron-phonon scattering rate, and $\gamma_{\rm NR,i} = \hbar/2(\hbar\omega_{\rm Det} - i\varepsilon_j)$, defined by Heisenberg uncertainty, is the annihilation rate of cold carriers at the state i. After normalization, the probability for multiple phonon absorption events is given as:

$$P_\uparrow^{\rm Abs} = \frac{Q_\uparrow}{Q_\uparrow + Q_\downarrow}, \tag{6.7}$$

Our model estimates the expected energy gain as $\langle \Delta E \rangle = \sum_n n\varepsilon_{\rm ph} P_\uparrow^{\rm Abs}$. Since electrons preferentially couple to longitudinal optical (LO) phonon modes, whose energy spectrum is discrete, we consider a spacing of $\varepsilon_{\rm ph} = \hbar\omega_{\rm LO}$ between intermediate levels. In the calculation, we used experimental parameters of $\hbar\omega_{\rm Det}$ = 2.41 eV (see Fig. 6.8(b)), $\hbar\omega_{\rm LO}$ = 16 meV (see Fig. 6.11(d)) and $\gamma_{\rm e-ph} \approx \gamma_{\rm cooling} \sim$1.5 ps^{-1} (see Fig. 6.12(c)) for

$CsPbBr_3$ NCs and $\hbar\omega_{\mathrm{Det}}$ = 2.07 eV [50] and 2.14 eV [14, 15], $\hbar\omega_{\mathrm{LO}}$ = 21 meV [51, 52] and 26 meV [53, 54], $\gamma_{\mathrm{e-ph}}$ ~0.3 ps^{-1} [55] and 0.6 ps^{-1} [44, 46] for CdTe and CdSe NCs, respectively.

The calculated energy gain for several semiconductor NCs is shown in Fig. 6.16(b) (blue bars). With increasing LO phonon frequency, the absorbed thermal energy decreases rapidly following Bose-Einstein distribution that agrees well with experimental trend (orange bars). Quantitatively, the energy gain $\langle \Delta E \rangle$ is smaller than the measured value by an order of magnitude revealing that phonon-assisted UCPL requires contribution from not only optical phonons but also other species in the thermal bath. It is also evidenced by the pronounced UCPL signal even at 80 K (see Fig. 6.10(d)), at which the LO-phonon population is negligible. In contrast, low-energy phonons (~1-3 meV) are still abundant at any temperature. The converted lattice energy via direct scattering with acoustic modes is typically few meV [56]; hence, we expect the direct electron-acoustic and electron-optical-phonon coupling are not sufficient to explain for the ~200 meV gain in $CsPbX_3$ NCs at room temperature. We propose the crucial role of acoustic phonon excitations via phonon-phonon interactions.

6.5.3 Phonon-Assisted Exciton Transitions

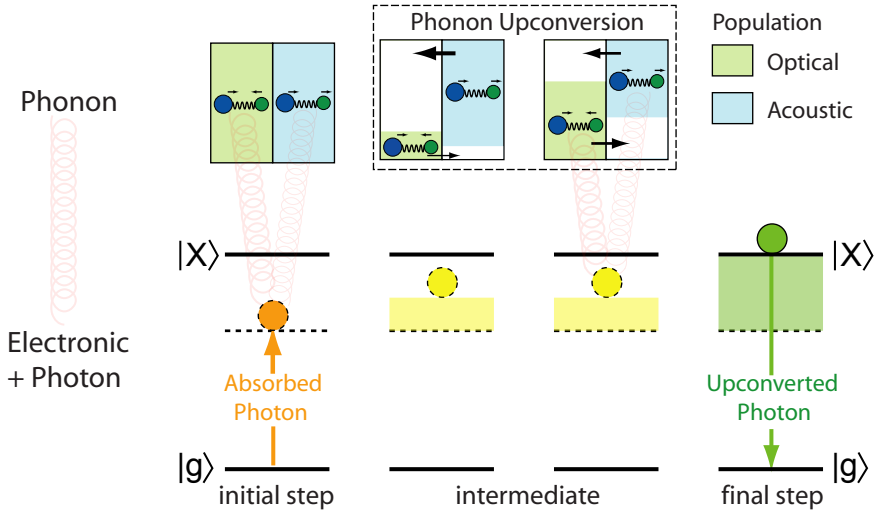

Figure 6.17: Possible pathways to exploit internal thermal energy (phonon) for upconverting low-energy into high-energy photons. In addition to the direct carrier-optical-phonon coupling, acoustic phonons also contribute to the overall process via phonon-phonon interactions.

Figure 6.17 illustrates the interaction among electron, photon and phonon subsystems as the possible mechanisms of photon-assisted optical transition in semiconductor

nanocrystals. The created carriers at the intermediate state can directly couple to optical phonon modes via Fröhlich interaction or to the acoustic phonon bath. At room temperature, both optical and acoustic phonon population are equivalently sizeable, leading to high probability of phonon-absorption, while the electron-optical coupling dominates. After the first few absorption events, such inequivalent interaction with the optical phonons leads to the deficiency of optical phonon population for further absorption, while the acoustic phonon bath remains almost full. The resultant non-equilibrium populations activate the phonon upconversion process, in which, multiple low-energy phonons are annihilated, creating a high-energy vibration [57, 58]. Strong acoustic-acoustic phonon annihilation results in the efficient recycling of optical phonons that can be used to heat the cold carriers. In this scenario, phonon upconversion directly promotes the probability of absorbing n optical phonons (see Eq. (6.5)-(6.6)) that in turn, amplifies the energy gain. Semiconducting lead halide perovskites exhibit low thermal conductivities [59–63], which implies that the recycling of lattice vibrational energy can be very efficient because of the large population of localized acoustic phonons that enhances probability of acoustic-to-optical phonon conversion. Strong phonon upconversion has been recently realized in these materials, which is stronger than conventional semiconductors due to their special phonon energy spectrum [40]. The considerable overlap between acoustic with optical branches facilitates even more the lattice energy conversion. We expect that future calculation simultaneously incorporating electron-phonon and phonon-phonon interactions might contribute to a nonlinear increase of the energy gain of the phonon-assisted upconversion process that in specific, explains for the striking energy gain of $8k_BT$ in $CsPbX_3$ NCs.

6.6 Conclusion

In conclusion, we highlight the efficient upconversion luminescence with strong two-photon absorption and striking phonon-assisted energy gain of $8k_BT$ in high-quality all-inorganic $CsPbX_3$ perovskite NCs. In addition to the strong direct electron-phonon interaction, we suggest the essential contribution from acoustic phonons to the optical transition via phonon-phonon interactions. In the non-equilibrium conditions, the acoustic phonon upconversion recycles the population of optical modes and boosts the efficiency of the phonon-assisted exciton transition. Overall, the phonon-assisted upconversion luminescence is a complex process, where not only light-matter but also

matter-matter interactions are important. Tailor making high-quality nanomaterials with strong electron-phonon interaction and low thermal conductivity may strongly promote the technologies based on light upconversion phenomenon.

References

1. Baluschev, S., Miteva, T., Yakutkin, V., Nelles, G., Yasuda, A. & Wegner, G. Upconversion fluorescence: Noncoherent excitation by sunlight. *Phys. Rev. Lett.* **97,** 143903 (14 2006).

2. Zhou, B., Shi, B., Jin, D. & Liu, X. Controlling upconversion nanocrystals for emerging applications. *Nat. Nanotech.* **10,** 924 (2015).

3. Kaiser, W. & Garrett, C. Two-photon excitation in CaF_2:Eu^{2+}. *Phys. Rev. Lett.* **7,** 229 (1961).

4. Shalav, A., Richards, B., Trupke, T., Krämer, K. & Güdel, H. U. Application of $NaYF_4$:Er^{3+} upconverting phosphors for enhanced near-infrared silicon solar cell response. *Appl. Phys. Lett.* **86,** 013505 (2005).

5. Mauser, N., Piatkowski, D., Mancabelli, T., Nyk, M., Mackowski, S. & Hartschuh, A. Tip enhancement of upconversion photoluminescence from rare earth ion doped nanocrystals. *ACS Nano* **9,** 3617–3626 (2015).

6. Yamamoto, K., Fujii, M., Sowa, S., Imakita, K. & Aoki, K. Upconversion luminescence of rare-earth-doped Y_2O_3 nanoparticle with metal nano-cap. *J. Phys. Chem. C* **119,** 1175–1179 (2015).

7. Prasad, P. N., Bhawalkar, J. D., He, G. S., Zhao, C. F., Gvishi, R., Ruland, G. E., Zieba, J., Cheng, P. C. & Pan, S. J. *Two-photon upconverting dyes and applications* US Patent 5,912,257. 1999.

8. Chen, G. *et al.* Energy-cascaded upconversion in an organic dye-sensitized core shell fluoride nanocrystal. *Nano Lett.* **15,** 7400–7407 (2015).

9. Yang, H., Han, C., Zhu, X., Liu, Y., Zhang, K. Y., Liu, S., Zhao, Q., Li, F. & Huang, W. Upconversion luminescent chemodosimeter based on NIR organic dye for monitoring methylmercury in vivo. *Adv. Funct. Mater.* **26,** 1945–1953 (2016).

10. Akizuki, N., Aota, S., Mouri, S., Matsuda, K. & Miyauchi, Y. Efficient near-infrared upconversion photoluminescence in carbon nanotubes. *Nat. Commun.* **6,** 8920–8920 (2015).

11. Zhang, J., Li, D., Chen, R. & Xiong, Q. Laser cooling of a semiconductor by 40 kelvin. *Nature* **493,** 504 (2013).

12. Zhang, Q., Liu, X., Utama, M. I. B., Xing, G., Sum, T. C. & Xiong, Q. Phonon-assisted anti-Stokes lasing in ZnTe nanoribbons. *Adv. Mater.* **28,** 276–283 (2016).

13. Wang, X., Yu, W. W., Zhang, J., Aldana, J., Peng, X. & Xiao, M. Photoluminescence upconversion in colloidal CdTe quantum dots. *Phys. Rev. B* **68,** 125318 (12 2003).

14. Chen, W., Joly, A. G. & McCready, D. E. Upconversion luminescence from CdSe nanoparticles. *J. Chem. Phys.* **122,** 224708 (2005).

15. Jakubek, Z. J., deVries, J., Lin, S., Ripmeester, J. & Yu, K. Exciton recombination and upconverted photoluminescence in colloidal CdSe quantum dots. *J. Phys. Chem. C* **112,** 8153–8158 (2008).

16. Deutsch, Z., Neeman, L. & Oron, D. Luminescence upconversion in colloidal double quantum dots. *Nat. Nanotech.* **8,** 649–653 (2013).

17. Teitelboim, A. & Oron, D. Broadband near-infrared to visible upconversion in quantum dot-quantum well heterostructures. *ACS Nano* **10,** 446–452 (2015).

18. Ha, S. T., Shen, C., Zhang, J. & Xiong, Q. Laser cooling of organic–inorganic lead halide perovskites. *Nat. Photonics* **10,** 115 (2016).

19. Protesescu, L., Yakunin, S., Bodnarchuk, M. I., Krieg, F., Caputo, R., Hendon, C. H., Yang, R. X., Walsh, A. & Kovalenko, M. V. Nanocrystals of cesium lead halide perovskites ($CsPbX_3$, X=Cl, Br, and I): Novel optoelectronic materials showing bright emission with wide color gamut. *Nano Lett.* **15,** 3692–3696 (2015).

20. Swarnkar, A., Marshall, A. R., Sanehira, E. M., Chernomordik, B. D., Moore, D. T., Christians, J. A., Chakrabarti, T. & Luther, J. M. Quantum dot-induced phase stabilization of α-$CsPbI_3$ perovskite for high-efficiency photovoltaics. *Science* **354,** 92–95 (2016).

21. Akkerman, Q. A., D'Innocenzo, V., Accornero, S., Scarpellini, A., Petrozza, A., Prato, M. & Manna, L. Tuning the optical properties of cesium lead halide perovskite nanocrystals by anion exchange reactions. *J. Am. Chem. Soc.* **137,** 10276–10281 (2015).

22. Nedelcu, G., Protesescu, L., Yakunin, S., Bodnarchuk, M. I., Grotevent, M. J. & Kovalenko, M. V. Fast anion-exchange in highly luminescent nanocrystals of cesium lead halide perovskites ($CsPbX_3$, X = Cl, Br, I). *Nano Lett.* **15,** 5635–5640 (2015).

23. Yakunin, S., Protesescu, L., Krieg, F., Bodnarchuk, M. I., Nedelcu, G., Humer, M., De Luca, G., Fiebig, M., Heiss, W. & Kovalenko, M. V. Low-threshold amplified spontaneous emission and lasing from colloidal nanocrystals of caesium lead halide perovskites. *Nat. Commun.* **6,** 8056 (2015).

24. Makarov, N. S., Guo, S., Isaienko, O., Liu, W., Robel, I. & Klimov, V. I. Spectral and dynamical properties of single excitons, biexcitons, and trions in cesium lead halide perovskite quantum dots. *Nano Lett.* **16,** 2349–2362 (2016).

25. García-Santamaría, F., Brovelli, S., Viswanatha, R., Hollingsworth, J. A., Htoon, H., Crooker, S. A. & Klimov, V. I. Breakdown of volume scaling in Auger recombination in CdSe/CdS heteronanocrystals: The role of the core-shell interface. *Nano Lett.* **11,** 687–693 (2011).

26. Eilers, J., van Hest, J., Meijerink, A. & Donega, C. d. M. Unravelling the size and temperature dependence of exciton lifetimes in colloidal ZnSe quantum dots. *J. Phys. Chem. C* **118,** 23313–23319 (2014).

27. Granados del Águila, A., Groeneveld, E., Maan, J. C., de Mello Donegá, C. & Christianen, P. C. M. Effect of electron-hole overlap and exchange interaction on exciton radiative lifetimes of CdTe/CdSe heteronanocrystals. *ACS Nano* **10,** 4102–4110 (2016).

28. Crooker, S. A., Barrick, T., Hollingsworth, J. A. & Klimov, V. I. Multiple temperature regimes of radiative decay in CdSe nanocrystal quantum dots: Intrinsic limits to the dark-exciton lifetime. *Appl. Phys. Lett.* **82,** 2793–2795 (2003).

29. De Mello Donegá, C., Bode, M. & Meijerink, A. Size- and temperature-dependence of exciton lifetimes in CdSe quantum dots. *Phys. Rev. B* **74,** 085320 (8 2006).

30. Rakovich, Y. P., Donegan, J. F., Vasilevskiy, M. I. & Rogach, A. L. Anti-Stokes cooling in semiconductor nanocrystal quantum dots: A feasibility study. *Phys. Status Solidi A* **206,** 2497–2509 (2009).

31. Sebastian, M., Peters, J. A., Stoumpos, C. C., Im, J., Kostina, S. S., Liu, Z., Kanatzidis, M. G., Freeman, A. J. & Wessels, B. W. Excitonic emissions and above-band-gap luminescence in the single-crystal perovskite semiconductors $CsPbBr_3$ and $CsPbCl_3$. *Phys. Rev. B* **92,** 235210 (23 2015).

32. Sestu, N. *et al.* Absorption F-sum rule for the exciton binding energy in methylammonium lead halide perovskites. *J. Phys. Chem. Lett.* **6,** 4566–4572 (2015).

33. Li, J., Yuan, X., Jing, P., Li, J., Wei, M., Hua, J., Zhao, J. & Tian, L. Temperature-dependent photoluminescence of inorganic perovskite nanocrystal films. *RSC Adv.* **6,** 78311–78316 (2016).

34. Wei, K., Xu, Z., Chen, R., Zheng, X., Cheng, X. & Jiang, T. Temperature-dependent excitonic photoluminescence excited by two-photon absorption in perovskite $CsPbBr_3$ quantum dots. *Opt. Lett.* **41,** 3821–3824 (2016).

35. Do, T. T. H., Granados del Águila, A., Cui, C., Xing, J., Ning, Z. & Xiong, Q. Optical study on intrinsic exciton states in high-quality $CH_3NH_3PbBr_3$ single crystals. *Phys. Rev. B* **96,** 075308 (2017).

36. Aharonovich, I., Castelletto, S., Simpson, D. A., Stacey, A., McCallum, J., Greentree, A. D. & Prawer, S. Two-level ultrabright single photon emission from diamond nanocrystals. *Nano Lett.* **9,** 3191–3195 (2009).

37. Xiong, Y., Liu, C., Wang, J., Han, J. & Zhao, X. Near-infrared anti-Stokes photoluminescence of PbS QDs embedded in glasses. *Opt. Express* **25,** 6874–6882 (2017).

38. Calistru, D. M., Mihut, L., Lefrant, S. & Baltog, I. Identification of the symmetry of phonon modes in $CsPbCl_3$ in phase IV by Raman and resonance-Raman scattering. *J. Appl. Phys.* **82,** 5391–5395 (1997).

39. Yaffe, O. *et al.* Local polar fluctuations in lead halide perovskite crystals. *Phys. Rev. Lett.* **118,** 136001 (13 2017).

40. Yang, J. *et al.* Acoustic-optical phonon up-conversion and hot-phonon bottleneck in lead-halide perovskites. *Nat. Commun.* **8,** 14120 (2017).

41. Von der Linde, D. & Lambrich, R. Direct measurement of hot-electron relaxation by picosecond spectroscopy. *Phys. Rev. Lett.* **42,** 1090 (1979).

42. Zanato, D., Balkan, N., Ridley, B., Hill, G. & Schaff, W. Hot electron cooling rates via the emission of LO-phonons in InN. *Semicond. Sci. Technol.* **19,** 1024 (2004).

43. Klimov, V. I. & McBranch, D. W. Femtosecond 1P-to-1S electron relaxation in strongly confined semiconductor nanocrystals. *Phys. Rev. Lett.* **80,** 4028 (1998).

44. Achermann, M., Bartko, A. P., Hollingsworth, J. A. & Klimov, V. I. The effect of Auger heating on intraband carrier relaxation in semiconductor quantum rods. *Nat. Phys.* **2,** 557 (2006).

45. Gao, Y., Talgorn, E., Aerts, M., Trinh, M. T., Schins, J. M., Houtepen, A. J. & Siebbeles, L. D. Enhanced hot-carrier cooling and ultrafast spectral diffusion in strongly coupled PbSe quantum-dot solids. *Nano Lett.* **11,** 5471–5476 (2011).

46. Maity, P., Debnath, T. & Ghosh, H. N. Slow electron cooling dynamics mediated by electron-hole decoupling in highly luminescent CdS_xSe_{1-x} alloy quantum dots. *J. Phys. Chem. C* **119,** 10785–10792 (2015).

47. Scamarcio, G., Spagnolo, V., Ventruti, G., Lugara, M. & Righini, G. Size dependence of electron-LO-phonon coupling in semiconductor nanocrystals. *Phys. Rev. B* **53,** R10489 (1996).

48. Zhang, Q., Liu, X., Utama, M. I. B., Zhang, J., de la Mata, M., Arbiol, J., Lu, Y., Sum, T. C. & Xiong, Q. Highly enhanced exciton recombination rate by strong electron-phonon coupling in single ZnTe nanobelt. *Nano Lett.* **12,** 6420–6427 (2012).

49. Chen, J., Morrow, D. J., Fu, Y., Zheng, W., Zhao, Y., Dang, L., Stolt, M. J., Kohler, D. D., Wang, X., Czech, K. J., *et al.* Single-crystal thin films of cesium lead bromide perovskite epitaxially grown on metal oxide perovskite ($SrTiO_3$). *J. Am. Chem. Soc.* **139,** 13525–13532 (2017).

50. Joly, A. G., Chen, W., McCready, D. E., Malm, J.-O. & Bovin, J.-O. Upconversion luminescence of CdTe nanoparticles. *Phys. Rev. B* **71,** 165304 (2005).

51. De Paula, A., Barbosa, L., Cruz, C., Alves, O., Sanjurjo, J. & Cesar, C. Quantum confinement effects on the optical phonons of CdTe quantum dots. *Superlattices Microst.* **23,** 1103–1106 (1998).

52. Bruchhausen, A., Fainstein, A., Jusserand, B. & André, R. Resonant Raman scattering by CdTe quantum-well-confined optical phonons in a semiconductor microcavity. *Phys. Rev. B* **73,** 085305 (2006).

53. Lange, H., Artemyev, M., Woggon, U. & Thomsen, C. Geometry dependence of the phonon modes in CdSe nanorods. *Nanotechnology* **20,** 045705 (2008).

54. Lin, C., Kelley, D. F., Rico, M. & Kelley, A. M. The “surface optical" phonon in CdSe nanocrystals. *ACS Nano* **8,** 3928–3938 (2014).

55. Rawalekar, S., Kaniyankandy, S., Verma, S. & Ghosh, H. N. Ultrafast charge carrier relaxation and charge transfer dynamics of CdTe/CdS core-shell quantum dots as studied by femtosecond transient absorption spectroscopy. *J. Phys. Chem. C* **114,** 1460–1466 (2009).

56. Eshlaghi, S., Worthoff, W., Wieck, A. & Suter, D. Luminescence upconversion in GaAs quantum wells. *Phys. Rev. B* **77,** 245317 (2008).

57. Shin, S. & Kaviany, M. Optical phonon production by upconversion: Heterojunction transmitted versus native phonons. *Phys. Rev. B* **91,** 165310 (2015).

58. Caretta, A., Donker, M. C., Perdok, D. W., Abbaszadeh, D., Polyakov, A. O., Havenith, R. W., Palstra, T. T. & van Loosdrecht, P. H. Measurement of the acoustic-to-optical phonon coupling in multicomponent systems. *Phys. Rev. B* **91,** 054111 (2015).

59. Pisoni, A., Jacimovic, J., Barisic, O. S., Spina, M., Gaál, R., Forró, L. & Horváth, E. Ultra-low thermal conductivity in organic-inorganic hybrid perovskite $CH_3NH_3PbI_3$. *J. Phys. Chem. Lett.* **5,** 2488–2492 (2014).

60. Yue, S., Zhang, X., Qin, G., Yang, J. & Hu, M. Insight into the collective vibrational modes driving ultralow thermal conductivity of perovskite solar cells. *Phys. Rev. B* **94,** 115427 (2016).

61. Qian, X., Gu, X. & Yang, R. Lattice thermal conductivity of organic-inorganic hybrid perovskite $CH_3NH_3PbI_3$. *Appl. Phys. Lett.* **108,** 063902 (2016).

62. Létoublon, A. *et al.* Elastic constants, optical phonons, and molecular relaxations in the high temperature plastic phase of the $CH_3NH_3PbBr_3$ hybrid perovskite. *J. Phys. Chem. Lett.* **7,** 3776–3784 (2016).

63. Elbaz, G. A., Ong, W.-L., Doud, E. A., Kim, P., Paley, D. W., Roy, X. & Malen, J. A. Phonon speed, not scattering, differentiates thermal transport in lead halide perovskites. *Nano Lett.* **17,** 5734–5739 (2017).

Chapter 7

Summary and Outlook

7.1 Summary

The year of 2019 marks ten years of intensive efforts to bring lead halide perovskite surpassing conventional semiconductors in energy-harvesting efficiency. Up to now, the peak power-conversion efficiency of the perovskite-based solar cells has been recorded at 23.7% [1] and the external quantum efficiency of the perovskite-based light-emitting diodes has been boosted to beyond 20% [2, 3]. These results promise a stable development of perovskite research in the future. Along with the application route, understanding the fundamental properties, though still lagging behind, has also gained encouraging achievements. In this thesis:

1. We have unravelled the multiple interband transitions near the bandedges that dominate the optical properties of lead halide perovskite semiconductors. Furthermore, different excitons with distinct binding energies explain for the wide range of reported exciton binding energy of these materials. When the optical transitions are not well resolved in the optical spectra, the analysis would lead to an average value of the binding energies of different excitons existing in the systems. Our results call for the reconsideration of the current theory concerning the electronic band structures. The role of the cations needs to be included.

2. We have resolved multiple optical transitions in the perovskite quantum-wells, through which, the degeneracy of the electronic bands has been revealed. As a result of quantum- and dielectric-confinement effects, the strong electron-hole spin-exchange interaction gives rise to the pronounced exciton fine-structure splitting, which is an order of magnitude larger than conventional III-V quantum-wells. We have observed the simultaneous presence of anisotropic and isotropic excitons that originates from the nontrivial interplay between electron-hole exchange

interactions, Rashba effects and the internal electric field in the quantum-well structures. The observation of multiple exciton bands with distinct properties suggests that layered perovskites provide ideal platforms for studying exciton spin-physics. The interplay of different spin-interacting processes poses new challenges towards establishing a complete and coherent electronic band structures for these atomically thin semiconductors. In contrast to the bulk, the exciton dynamics in 2D perovskite is rather fast. At cryogenic temperature, the relaxation among the exciton bands occur within $\sim$500 fs after the photo-excitation. Furthermore, the major part of the photoluminescence decays completely within $\sim$1 ns that is indicative of optically active transitions. Our results provide a comprehensive picture towards the understanding of the exciton band structures in 2D perovskites.

3. We have explained the efficient phonon-assisted exciton transition process in perovskite nanocrystals. In particular, we have evaluated the maximum thermal energy of up to $\sim 8k_BT$ ($\sim$200 meV), which can be exploited to an enable optical transitions under the low-energy photo-excitation condition. The process requires the consecutive absorption of more than ten optical phonons that is uniquely demonstrated in perovskite nanocrystals. In quantum-confined systems, the inherently strong electron-phonon interaction in perovskite materials is enhanced. Furthermore, the low thermal conductivity and the special phonon spectra of perovskites promote the multiple optical-phonon absorption process via phonon-upconversion. The overall phonon-assisted upconversion photoluminescence is a complicated process, where both light-matter and matter-matter interactions play important role. The fundamental understanding of the phonon-assisted upconversion photoluminescence on these emergent perovskite materials allows for the design of nanomaterials to enhance both electron-phonon and phonon-phonon interactions for energy-conversion devices.

7.2 Outlook

Our work presented in this thesis has revealed new understanding of the emission properties, electronic band structures and the exciton fine-structure details of lead halide perovskite semiconductors. There remains unanswered questions to be solved to establish a complete understanding of the fundamental properties. This section will discuss

few issues to be addressed in the follow-up work.

7.2.1 Microscopic Origins of the Multiple Transitions

We have demonstrated that the optical properties of lead halide perovskites at low temperature consist of multiple transitions, which arise from different electronic bands near the fundamental bandedges. Our results on several perovskite compounds suggest that while the inorganic lead-halide framework contributes importantly to the electronic band structure, the role of the cations cannot be overlooked. So far, theoretical calculations have predicted the former part, while the latter part remains unclear.

Furthermore, by angle-resolved photoemission spectroscopy technique, a giant Rashba effect has been observed on $CH_3NH_3PbBr_3$ single crystals at low-temperature orthorhombic and high-temperature cubic phases [4]. On the other hand, a recent work evaluated a modest Rashba effect on $CH_3NH_3PbI_3$ at room-temperature tetragonal phase [5]. The actual Rashba splitting in the bulk perovskite structure is still controversial. The density functional theory (DFT) calculation for the band structure needs to be critically revised, taking into account the role of the cations and carefully considering the structural distortion caused by different reasons such as the disorder of the organic cations and the structural relaxation.

Experimentally, future optical measurements, conducted in external magnetic and electric fields, are also useful to investigate the significance of Rashba effects on the electronic band structure of perovskite semiconductors. In these experiments, high-quality bulk single crystals are required to minimize the surface disorders and defect levels. The combination of experimental and theoretical work will elucidate the nontrivial band structures of perovskites. The knowledge of the microscopic origins of the multiple transitions will be crucial for understanding the carrier/exciton relaxation between the bands and the prolong photoluminescence decays.

7.2.2 Origin of the Indirect Transition in Two-Dimensional Perovskites

Similarly to the bulk perovskites, the optical spectra of two-dimensional structures also comprise multiple optical transitions, among which, the indirect properties are manifested in the lowest-energy transition. The origin of the indirect nature is still questionable. Future theoretical calculation needs to include the surface disorder due to the organic

barrier, which causes the broken inversion symmetry and Rashba effects.

In order to unravel the microsopic origin of this indirect-like transition, the optical measurements in external electric and magnetic fields will be important. The electric field can tilt the band alignment of the multiple quantum-well structures. Consequently, if X_1 is an interlayer exciton, the energy and oscillator strength will strongly depend on the electric field strength. On the other hand, the exciton originating from the Rashba-split bands, will response to the applied magnetic field. Due to the rather broad linewidth, high magnetic field will be required to induce a noticeable change. The understanding of the precise origin of this transition is critically important to interpret the spin-dynamics of this material.

7.2.3 Control of spin-interaction in perovskite nanostructures

As a result of the strong quantum- and dielectric-confinement, the spin-interacting processes in perovskite quantum-wells are significantly enhanced. While the confinement effects can be precisely controlled by the thickness of the perovskite quantum-wells, the dielectric confinement can be tuned by changing the barrier environment. A comprehensive study on different quantum-well thickness and different organic barriers will reveal the relation between the confinement effects on different spin-interacting processes, particularly electron-hole exchange interaction and Rashba effects.

Due to the nontrivial interplay between different spin-interacting processes, the spin dynamics is not trivial. Future work to determine the spin lifetime and spin-flip processes in these 2D perovskites systems, taking multiple optical transitions into consideration, will be useful, from which, the functional spintronic and spin-orbitronic devices can be designed and fabricated.

In addition, dimensionality is another tunability freedom. Apart from 2D, the spin-interaction can be tuned by utilizing other perovskite nanostructures such as nanowires and nanocrystals. The reduced dimensionality allows for the enhancement of spin-exchange interaction between electrons and holes. Exciton fine-structure has been revealed in perovskite nanocrystals [6–8]. Although the studied NC sizes in literature lie in the weak confinement regime, the reported energy splitting still differed by an order of magnitude. Future study on the size-dependent splitting as well as measurements in magnetic field would be needed to confirm the exciton fine-structure, energy splitting and optical selection rules on each transition.

References

1. https://www.nrel.gov/pv/assets/pdfs/pv-efficiency-chart.20181221.pdf.

2. Lin, K., Xing, J., Quan, L. N., de Arquer, F. P. G., Gong, X., Lu, J., Xie, L., Zhao, W., Zhang, D., Yan, C., *et al.* Perovskite light-emitting diodes with external quantum efficiency exceeding 20 percent. *Nature* **562,** 245 (2018).

3. Cao, Y., Wang, N., Tian, H., Guo, J., Wei, Y., Chen, H., Miao, Y., Zou, W., Pan, K., He, Y., *et al.* Perovskite light-emitting diodes based on spontaneously formed submicrometre-scale structures. *Nature* **562,** 249 (2018).

4. Niesner, D., Wilhelm, M., Levchuk, I., Osvet, A., Shrestha, S., Batentschuk, M., Brabec, C. & Fauster, T. Giant Rashba splitting in $CH_3NH_3PbBr_3$ organic-inorganic perovskite. *Phys. Rev. Lett.* **117,** 126401 (2016).

5. Frohna, K., Deshpande, T., Harter, J., Peng, W., Barker, B. A., Neaton, J. B., Louie, S. G., Bakr, O. M., Hsieh, D. & Bernardi, M. Inversion symmetry and bulk Rashba effect in methylammonium lead iodide perovskite single crystals. *Nat. Commun.* **9,** 1829 (2018).

6. Yin, C. *et al.* Bright-exciton fine-structure splittings in single perovskite nanocrystals. *Phys. Rev. Lett.* **119,** 026401 (2017).

7. Becker, M. A., Vaxenburg, R., Nedelcu, G., Sercel, P. C., Shabaev, A., Mehl, M. J., Michopoulos, J. G., Lambrakos, S. G., Bernstein, N., Lyons, J. L., *et al.* Bright triplet excitons in caesium lead halide perovskites. *Nature* **553,** 189 (2018).

8. Utzat, H., Sun, W., Kaplan, A. E., Krieg, F., Ginterseder, M., Spokoyny, B., Klein, N. D., Shulenberger, K. E., Perkinson, C. F., Kovalenko, M. V., *et al.* Coherent single-photon emission from colloidal lead halide perovskite quantum dots. *Science* **363,** 1068–1072 (2019).

List of Publications

1. **T. Thu Ha Do**, Andrés Granados del Águila, Chao Cui, Jun Xing, Zhijun Ning, Qihua Xiong. Optical study on intrinsic exciton states in high-quality $CH_3NH_3PbBr_3$ single crystals. *Phys. Rev. B* **96**, 075308 (2017).

2. Xinxiong Li*, **T. Thu Ha Do***, Andrés Granados del Águila, Yinjuan Huang, Wangqiao Chen, Qihua Xiong, Qichun Zhang. A 3D haloplumbate framework constructed from unprecedented lindqvist-like highly-coordinated $[Pb_6Br_{25}]^{13-}$ nanoclusters with temperature-dependent emission. *Chem. Asian J.* **13**, 3185 (2018). (***equal contribution**)

3. Xinxiong Li*, **T. Thu Ha Do***, Andrés Granados del Águila, Yinjuan Huang, Wangqiao Chen, Yongxin Li, Rakesh Ganguly, Samuel Morris, Qihua Xiong, Dongsheng Li, Qichun Zhang. Two-Dimensional and Emission-Tunable: An Unusual Perovskite Constructed from Lindqvist-Type $[Pb_6Br_{19}]^{7-}$ Nanoclusters. *Inorg. Chem.* **57**, 14035 (2018). (***equal contribution**)

4. Sheng Liu, Shishuai Sun, Chee Kwan Gan, Andrés Granados del Águila, Yanan Fang, Jun Xing, **T. Thu Ha Do**, Tim White, Hongguo Li, Qihua Xiong. Manipulating Efficient Light Emission in Two-dimensional Perovskite Crystals by Pressure-induced Anisotropic Deformation. *Sci. Adv.* **5**(7), eaav9445 (2019).

5. Andrés Granados del Águila*, Sheng Liu*, **T. Thu Ha Do***, Zhuangchai Lai, Thu Ha Tran, Sean Ryan Krupp, Zhirui Gong, Hua Zhang, Wang Yao, Qihua Xiong. Linearly Polarized Luminescence of Atomically-thin MoS2 Semiconductor Nanocrystals. ACS Nano, 13 (11), 13006-13014 (2019). (***equal contribution**)

6. **T. Thu Ha Do**, Andrés Granados del Águila, Jun Xing, Sheng Liu, Chongyun Jiang, Weibo Gao, Qihua Xiong. Anisotropic bright excitons in two-dimensional layered perovskites. (2019). **under revision**.

7. Di Bao, Andrés Granados del Águila, **T. Thu Ha Do**, Sheng Liu, Qihua Xiong. Probing Dark Exciton by Near-Resonance Photoluminescence Excitation Spectroscopy in WS_2 Monolayer. **submitted**.

8. Andrés Granados del Águila*, **T. Thu Ha Do***, Jun Xing, Wen Jie Jee, Lulu Zhang, Qihua Xiong. Efficient upconversion photoluminescence in all-inorganic lead halide perovskite nanocrystals. **to be submitted**. (***equal contribution**)